Alma Mater Studiorum · Università di Bologna

Scuola di Scienze
Dipartimento di Fisica e Astronomia
Corso di Laurea Magistrale in Fisica

Neutrino physics with the XENONnT experiment

Relatore:
Prof.ssa Gabriella Sartorelli

Presentata da:
Federica Pompa

Correlatori:
Dott. Marco Selvi
Dott. Pietro Di Gangi

Anno Accademico 2018/2019

To my family,
that has always supported me.
To my love,
that has always been with me.
To all people who never believed in me:
as proof that I did it, even without them.

Ancora adesso, nelle terre di Carewall, tutti raccontano quel viaggio. Ognuno a modo suo. Tutti senza averlo mai visto. Ma non importa. Non smetteranno mai di raccontarlo. Perché nessuno possa dimenticare di quanto sarebbe bello se, per ogni mare che ci aspetta, ci fosse un fiume, per noi. E qualcuno - un padre, un amore, qualcuno - capace di prenderci per mano e di trovare quel fiume - immaginarlo, inventarlo - e sulla sua corrente posarci, con la leggerezza di una sola parola, addio.

Alessandro Baricco
Oceano Mare

Abstract

One of the most active fields in physics is the search for Dark Matter, for which the XENON Project is one of the main protagonists. The new XENONnT experiment will be operative starting from 2020 in the underground *Laboratori Nazionali del Gran Sasso*, under 3600 meters water equivalent of mountain rock shield. It is a multi-ton detector for direct search of Dark Matter, consisting of a double phase liquid-gas xenon TPC which contains 5.9 t of liquid xenon target mass, inserted in a Cryostat surrounded by a tank containing 700 t of Gd-loaded water, instrumented with PMTs for muon and neutron tagging. Its aim, as that of its precursor XENON1T, is to detect WIMPs elastic scattering off xenon nucleus through the measure of the light and charge observable signals produced by recoils in LXe. A new neutron Veto system, surrounding the outer Cryostat and instrumented with 120 additional PMTs, will contribute to reduce the neutron background in the TPC. Thanks to the large xenon target used, this experiment is sensitive also to all flavors of Supernova neutrinos. These can be detected through two different interactions channels: through coherent elastic scatters on xenon nuclei in the TPC and through interactions of electron antineutrinos with protons of water via inverse beta decay process.
In the first part of this work, after a theoretical introduction to neutrino physics, I present the results of a Monte Carlo simulation to predict the XENONnT detection efficiencies for neutrino events as IBD interactions in the neutron and muon Vetoes.
In the last part of the thesis, I investigate the XENONnT possibility to detect neutrinoless double beta decay of ^{136}Xe isotope, a Standard Model forbidden decay which can prove the Majorana nature of neutrinos. Starting from evaluation of the ER background rate from Cryostat and PMTs in the energy region where we expect to observe $0\nu\beta\beta$, the sensitivity of XENONnT for this nuclear decay was estimated.

Sommario

Uno dei campi di ricerca più attivi della fisica è quello relativo alla ricerca della Materia Oscura, nel quale il Progetto XENON riveste il ruolo di uno tra i principali protagonisti. L' esperimento XENONnT, costruito nei *Laboratori Nazionali del Gran Sasso*, sotto 3600 metri di roccia che fungono da schermo contro i raggi cosmici, sarà operativo a partire dal 2020. È un rivelatore impiegato per la ricerca diretta della Materia Oscura, costituito da una TPC a doppia fase liquido-gas contenente circa 5.9 t di xenon liquido, inserita in un criostato circondato da un serbatoio contenente circa 700 t di acqua drogata con gadolinio e munita di PMTs per l'identificazione di muoni e neutroni. Il suo scopo, come quello del suo precursore XENON1T, è quello di rivelare lo scattering elastico delle WIMP sui nuclei di xenon attraverso la misura dei segnali di luce e carica generati dai rinculi nucleari. Il nuovo veto di neutroni, posto attorno al criostato e munito di 120 PMTs addizionali, contribuirà a ridurre il background da neutroni nella TPC. Grazie alla grande massa di xenon usata, questo esperimento è sensibile anche ai neutrini da Supernova. Questi possono essere rivelati attraverso due canali di interazione differenti: attraverso lo scattering elastico sui nuclei di xenon nella TPC ed attraverso le interazioni di antineutrini elettronici con i protoni dell'acqua via processi di decadimento beta inverso.
Nella prima parte di questo lavoro, dopo un'introduzione teorica alla fisica dei neutrini, presento i risultati di simulazioni Monte Carlo per la previsione dell'efficienza di rivelazione di XENONnT per eventi di IBD nei veti di neutroni e muoni.
Nell'ultima parte della tesi, analizzo la possibilità di XENONnT di rivelare il doppio decadimento beta senza emissione di neutrini dell'isotopo ^{136}Xe, una transizione proibita dal Modello Standard che, se osservata, potrebbe provare la natura dei neutrini come fermioni di Majorana. A partire dalla valutazione del rate di ER background da criostato e PMTs nella regione energetica in cui ci aspettiamo di osservare questo decadimento, è stata stimata la sensibilità di XENONnT per questa transizione.

Contents

Introduction

There are justified reasons to believe that new phenomena, new particles and new principles that would lead us to a deeper level of understanding of nature, are waiting for us beyond the description given today by the Standard Model of particle physics. Indeed, some considerations show that the Standard Model is incomplete and can be seen as a *low energy limit* of a more fundamental theory, which should reveal itself at higher energies.
First of all the awareness that, with the known physics, we are able to explain only a minimum part of the whole Universe composition. A lot of astrophysical and cosmological observations support the hypothesis that a considerable amount of energy content of the Universe is made of something we do not know and that is called *Dark Matter*. Candidate particles for Dark Matter arise in theories beyond the Standard Model and show some properties like a stable or very long lives, to confirm their expected abundance, no electric and color charge, so they do not interact through electromagnetic and strong interactions, and non relativistic nature, that characterizes massive particles. Due to such features, Dark Matter candidates are identified under the name of Weakly Interacting Massive Particles (WIMPs).
The number of experiments to directly detect WIMPs has grown in the last years. Among these, detectors using liquid xenon have demonstrated the highest sensitivities. Currently, the XENON Project at the *Laboratori Nazionali del Gran Sasso* (LNGS) has a leading role in this field, exploiting the technique of the double-phase Time Projection Chamber (TPC) based on liquid xenon.
Another evidence of something beyond the known physics is the definitive discovery of a non zero neutrino mass. This represented the first experimental hint for physics beyond the Standard Model.
Neutrino, with its unknown mass and uncertain Dirac or Majorana nature, is waiting to be placed into a new model, different from the Stan-

dard Model which can not describe it in the correct way. Determining if massive neutrinos are Dirac or Majorana fermions is crucial to define the mechanism that gives them mass: within the Standard Model, massive neutrinos can be only Dirac fermions, because the Higgs mechanism gives mass only to Dirac particles. The most promising way to investigate the nature of massive neutrinos is to search for the neutrinoless double beta decay, a forbidden Standard Model nuclear transition which explicitly violates the total lepton number. The observation of this transition would directly confirm the Majorana nature of neutrinos and the fact that lepton number is not a global symmetry of the Standard Model. Dark matter detectors that utilize liquid xenon have now achieved tonne-scale targets, giving them sensitivity to all flavors of Supernova neutrinos. During a Supernova explosion, most of the energy is released by neutrinos and antineutrinos of all flavors, with mean energies of tens of MeV. With the XENONnT experiment, neutrinos can be detected through two different interaction channels: via coherent elastic scatters of neutrino with xenon nuclei (CEνNS) in the TPC and through inverse beta decay (IBD) process in water.
This thesis work is focused on the possibility to detect Supernova neutrinos with the XENONnT neutron and muon Vetoes and on its sensitivity to observe the neutrinoless double beta decay of the ^{136}Xe isotope.

In Chapter 1, the theory of electroweak interactions is presented. Starting from the Fermi theory of weak interactions described in Sections 1.1 and 1.2, and discussing about parity violation in Section 1.3, the Intermediate Vector Boson (IVB) model is introduced to describe in the correct way the weak interactions (Section 1.4): these are mediated by the charged $W^{\pm}$ and neutral Z vector bosons. The Glashow-Weinberg-Salam model is described in Section 1.5. The gauge vector bosons, the quarks and the leptons which are massless, acquire mass following the appearance of another scalar bosonic field called the Higgs field, which is involved in the Spontaneous Symmetry Breaking process (Section 1.6). The gauge vector bosons acquire mass through the Higgs mechanism (Section 1.7) and also fermions and leptons acquire mass after the Spontaneous Symmetry Breaking process by interacting with the Higgs vacuum expectation value (Section 1.8).

In Chapter 2 the neutrino physics, with the problem related to its nature, is introduced. Both the Dirac (Section 2.1) and the Majorana (Section 2.2)

cases are presented, with their respective mass terms (Sections 2.1.1 and 2.2.1) and oscillation scenarios (Sections 2.1.2 and 2.2.2). The lepton number conservation is discussed in Section 2.1.3 for the Dirac case and in Section 2.2.3 for the Majorana one: from its non conservation in Majorana case, is possible to suspect that lepton number is not a global symmetry of the Standard Model but is just approximate, related to the range of energies that we can explore directly.

Chapter 3 is dedicated to a description of the XENON Dark Matter Project. In Section 3.1 the properties of liquid xenon as a detection medium are described. Among the liquid xenon based detectors, the double-phase TPC technology, whose detection principle is described in Section 3.2, has been widely used for the direct search of WIMPs because of its simple scalability and the ability to discriminate between electronic recoils (ER) and nuclear recoils (NR) (Section 3.2.1). Passing through the description of past XENON experiments (Section 3.3), Section 3.4 describes the new phase of the Project: the XENONnT experiment, that will be operative starting from 2020.

In Chapter 4, after a description of the explosion mechanism of a Supernova (Section 4.1), the neutrino and antineutrino signals of luminosity and mean energy emitted following the first 10 s of the explosion are reported (Section 4.2). This study was done considering two different Supernova progenitors of masses equal to $27M_{\odot}$ and $11.2M_{\odot}$ using two different Equations of State: the LS220 Equation of State and the Shen one. Considering only the SN progenitor of $27M_{\odot}$ in LS220 EoS, Section 4.3 shows the integrated fluxes for each neutrino and antineutrino flavor and, taking into account the neutrino oscillations and both scenarios of normal and inverted mass ordering, changes to these fluxes have been derived.

Chapter 5 is dedicated to the study of detection efficiency of XENONnT about interactions of Supernova electron antineutrinos in Gd-doped water via IBD process (Section 5.1). Using the XENONnT GEANT4 framework, Monte Carlo simulations of positrons and neutrons coming from the electron antineutrino interaction in water were performed, and the detection efficiency of the XENONnT detector is reported. A separated analysis on muon Veto (mVeto) and neutron Veto (nVeto) shows their different detection efficiencies about this kind of events. This analysis was

done considering electron antineutrinos coming from two different SN progenitors: from $27M_{\odot}$ SN in LS220 EoS and from $11.2M_{\odot}$ SN in Shen EoS. Results of this analysis are reported in Sections 5.2 and 5.3.

In Chapter 6 is presented the study on the possibility to detect the neutrinoless double beta decay of the ^{136}Xe isotope with XENONnT. After a theoretical introduction on this Standard Model forbidden nuclear transition (Section 6.1), the estimation of the electronic recoil background in XENONnT was performed (Section 6.2). Simulations of the radiogenic nuclides decays, that have the most relevant contribution for the ER background in the region of interest where we expect the neutrinoless double beta decay to occur, was performed. Following the selection criteria of single scatter interactions in the assumed fiducial volume, the background rate of all nuclides is obtained (Section 6.2.1) and the energy resolution of the detector is applyed (Section 6.2.2). The sensitivity for neutrinoless double beta decay of XENONnT is studied (Section 6.3). Adding also the monoenergetic peak of the signal, taking into account the energy resolution, the smeared spectra of background and signal rate are obtained (Section 6.4).

Chapter 1

The Standard Model of electroweak interactions

> I guerrieri della luce non sempre sono sicuri di ciò che stanno facendo. Molte volte trascorrono la notte in bianco, pensando che la loro vita non ha alcun significato. Per questo sono guerrieri della luce. Perché sbagliano. Perché si interrogano. Perché cercano una ragione: e certamente la troveranno.
>
> Paulo Coelho
> *Manuale del guerriero della luce*

The Standard Model of particle physics is the result of an immense experimental and inspired theoretical effort, spanning more than fifty years. It provides a remarkably accurate description of results from many experiments, depicting quarks and leptons as the building blocks of matter and describing their interactions through the exchange of force carriers: the photon for electromagnetic interactions, the W and Z bosons for weak interactions, and the gluons for strong interactions. The electromagnetic and weak interactions are unified in the electroweak theory. Nearly fifty years ago it was proposed [1–4] that spontaneous symmetry breaking in gauge theories could be achieved through the introduction of a scalar field. The application of this mechanism to the electroweak theory [5–7] leads to the generation of the W and Z masses, and to the prediction of the existence of the Higgs boson H [8, 9].

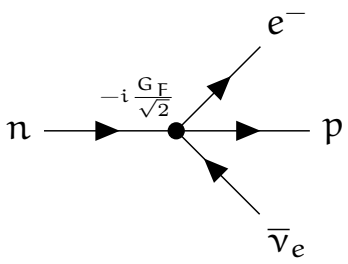

Figure 1.1: Feynman diagram of the neutron decay described in the Fermi theory.

1.1 Fermi theory of beta decay

The beginning of the weak interaction theory starts in 1934 with Fermi description of the β-decay

$$n \longrightarrow p + e^- + \overline{\nu}_e \tag{1.1}$$

in terms of quantum field theory. Fermi assumed that the emission of a $(e^-, \overline{\nu}_e)$ pair was analogous to the electromagnetic emission of a photon. He tried to copy the main features of electromagnetism, just by substituting to the photon the $(e^-, \overline{\nu}_e)$ pair. He described this interaction as a point interaction shown in Figure (1.1), mediated by the Fermi coupling constant G_F at the vertex.
Since the electromagnetic interaction of a charged particle is described by the following lagrangian:

$$\mathcal{L}_{em}^{int} = e\,\overline{\psi}\gamma^\mu\psi A_\mu \tag{1.2}$$

where ψ is the field describing the charge particle and A_μ the electromagnetic field, the Fermi ansatz for the process described in Equation (1.1) was

$$\mathcal{L}_F = -G_F(\overline{\psi}_e\,\Gamma^i\,\psi_\nu)(\overline{\psi}_p\,\Gamma_i\,\psi_n)\,. \tag{1.3}$$

where Γ^i is the operator that defines the type of interaction, constructed as a combination of Dirac γ^μ matrices. The index i can assume the values $i = S, V, T, A, P$, according to the behavior of the different bilinear form in Equation (1.3) under Lorentz transformations. All possibilities are shown in Table (1.1). In 1957 the weak coupling were definitely determined to be $V - A$.
Another important process to take into account is the muon decay into electron and antineutrinos:

$$\mu^- \longrightarrow e^- + \overline{\nu}_e + \nu_\mu\,. \tag{1.4}$$

Table 1.1: Bilinear forms and their behavior under Lorentz transformations

Γ^i	Bilinear form: $(\overline{\psi}_e \Gamma^i \psi_\nu)$	Nature under Lorentz transformations
$\mathbb{I}$	$\overline{\psi}_e \psi_\nu$	Scalar (S)
γ^μ	$\overline{\psi}_e \gamma^\mu \psi_\nu$	Vector (V)
$\sigma^{\mu\nu}$	$\overline{\psi}_e \sigma^{\mu\nu} \psi_\nu$	Tensor (T)
$\gamma^\mu\gamma_5$	$\overline{\psi}_e \gamma^\mu\gamma_5 \psi_\nu$	Axial-Vector (A)
γ_5	$\overline{\psi}_e \gamma_5 \psi_\nu$	Pseudo-Scalar (P)

This decay is very similar to the neutron decay of Equation (1.1) with the (n, p) pair replaced by the (μ^-, ν_μ) one. In fact, it can be described by a very similar interaction with the same coupling constant at the vertex.
It turns out that the global effective coupling constant G_F has practically the same value that was found for the nuclear beta decay. Its measured value is $G_F = 1.166 \times 10^{-5}\ GeV^{-2}$.

1.2 Problems of the Fermi theory

Consider the lagrangian of Equation (1.3). The main problem of the theory described by this is its non-renormalizability, due to the fact that the coupling constant G_F is not dimensionless.
This means that, evaluating Feynman diagrams beyond the tree level, one encounters divergences due to the bad ultraviolet behavior of the theory. To absorb all these divergences, it is necessary to add an infinite number of terms in the lagrangian. Doing this, the theory loses its predictivity.
Even if the Fermi theory is non-renormalizable, it can be used as an effective theory, valid up to some characteristic energy which, for instance, can be determined by looking at the unitary property of the theory. The unitarity requires that the scattering amplitudes are limited. However the bad high energy behavior of the non-renormalizable theory leads to increasing amplitudes, and therefore to a violation of unitarity.
The Fermi theory is an effective theory that works very well up to the threshold energy $E_0 \approx 367\ GeV$.

1.3 Parity violation in weak interactions

The idea that parity was not conserved in weak interactions came up in 1956. In this year, T.D. Lee and C.N. Yang made a review of the results obtained from the study of weak processes and concluded that there was no evidence of parity conservation in weak interactions [10]. New experiments were proposed in order to check the parity conservation law. These were based on the fact that only the measure of pseudoscalar quantities could give information about the conservation of parity, because these change sign under a parity transformation. Studying the beta decay of a polarized nucleus, one could look for the pseudoscalar quantity of the helicity h, defined as

$$h = \frac{\boldsymbol{\sigma} \cdot \mathbf{p}}{|\mathbf{p}|},$$

where $\boldsymbol{\sigma}$ is the spin of the nucleus and $\mathbf{p}$ the momentum of the outgoing electron.
The experiment was performed by Madame Wu and collaborators [11] who analyzed the decay of polarized cobalt nuclei:

$$^{60}\mathrm{Co} \longrightarrow {}^{60}\mathrm{Ni} + e^- + \overline{\nu}_e + 2\gamma\,. \tag{1.5}$$

The experiment showed a big asymmetry in the momentum distribution of the outgoing electrons: the number of emitted electrons in the parallel direction to the nuclear magnetization is different to that along the anti-parallel one. This was a very clear evidence of parity violation: the electrons where emitted preferentially in the opposite direction to the nuclear spin. So these have a negative value of the helicity $h = -1$, showing a left-handed chirality. As consequence, the antineutrino must be right-handed, with helicity $h = 1$.
To take into account parity violation, it is necessary to modify the weak lagrangian, introducing the chiral components of the fields.

1.4 IVB model for weak interactions

The V-A theory of weak interactions was developed in 1957 by Feynman and Gell-Mann [12] as an extension of the Fermi theory. The lagrangian assumes the form

$$\mathcal{L}_W = -\frac{G_F}{\sqrt{2}} J_\rho J^{\rho\dagger} \tag{1.6}$$

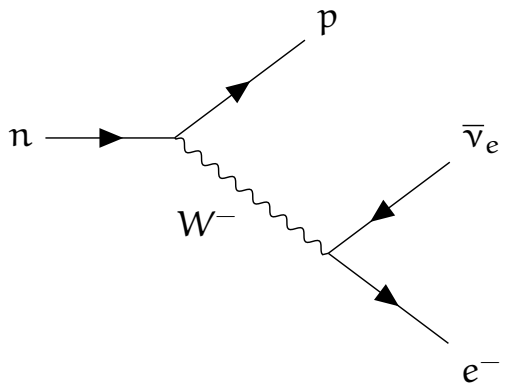

Figure 1.2: Feynman diagram of the neutron decay mediated by the W^- vector boson.

where the charged weak current J_ρ is the sum of two pieces, one coming from leptons and the other coming from the hadrons:

$$J_\rho = J^l_\rho + J^h_\rho\,; \tag{1.7a}$$

$$J^l_\rho = \sum_{l=e,\mu,\tau} \bar{l}\gamma_\rho\left(\frac{1-\gamma_5}{2}\right)\nu_l\,; \tag{1.7b}$$

$$J^h_\rho = \overline{p}\gamma_\rho(c_V + c_A\,\gamma_5)n\,, \tag{1.7c}$$

where c_V and c_A are coefficients related to the V-A coupling. In this discussion the hadronic sector is neglected and only the leptonic one is considered.
The analogy between QED and the V-A theory can be pushed further if one assumes that weak interactions are mediated by an Intermediate Vector Boson $W^\pm_\mu$. The main difference between the mediators of QED and those of weak theory is that in QED, since the photon is massless, the force is long range, instead weak interactions are short range, so we need to exchange a massive particle. Assuming that the charged weak current $J^\pm_\mu$ couples to such a field, the lagrangian can be written as:

$$\mathcal{L}_{IVB} = -\frac{g}{2\sqrt{2}}\left[J^\pm_\mu W^\mu_\pm + \left(J^\pm_\mu W^\mu_\pm\right)^\dagger\right], \tag{1.8}$$

where g is the dimensionless coupling constant of the weak interaction. So a process like the neutron decay in Equation (1.1) is mediated by a massive and charged vector boson $W^\pm$ as shown in Figure (1.2). It can be shown that, in the limit of low energies, the scattering amplitude of the

IVB theory reproduces that of the Fermi one with the following relation between the two coupling constants:

$$\frac{g^2}{8M_W^2} = \frac{G_F}{\sqrt{2}}, \tag{1.9}$$

where M_W is the mass of the W vector boson. In 1973, the discovery of the elastic scattering $\nu_\mu + e^- \longrightarrow \nu_\mu + e^-$ at CERN, led the discovery of another neutral vector boson: the Z boson [13, 14].

1.5 The Glashow-Weinberg-Salam model

We will consider only the leptonic sector restricted to the electron and its neutrino. Since we know that in weak interactions only the left-handed electron plays a role, we can introduce the projection operators P_L and P_R defined in Equations (A.11a) and (A.11b). Under their action, we can make the fields chirality explicit, as shown in Equations (A.13). The charged V-A currents $J_\mu^\pm$ of Equation (1.8) become:

$$J_\mu^+ = \overline{\psi}_{eL}\gamma_\mu\left(\frac{1-\gamma_5}{2}\right)\psi_{\nu_e} = \overline{\psi}_e\left(\frac{1+\gamma_5}{2}\right)\gamma_\mu\left(\frac{1-\gamma_5}{2}\right)\psi_{\nu_e}; \tag{1.10a}$$

$$J_\mu^- = \left(J_\mu^+\right)^\dagger = \overline{\psi}_{\nu_{eL}}\gamma_\mu\left(\frac{1-\gamma_5}{2}\right)\psi_e. \tag{1.10b}$$

Now, considering the left-handed electron and its neutrino in a single $SU(2)$ doublet:

$$L = \begin{pmatrix}\psi_{\nu_e}\\ \psi_e\end{pmatrix}_L = \left(\frac{1-\gamma_5}{2}\right)\begin{pmatrix}\psi_{\nu_e}\\ \psi_e\end{pmatrix}; \tag{1.11a}$$

$$\overline{L} = \begin{pmatrix}\overline{\psi}_{\nu_e} & \overline{\psi}_e\end{pmatrix}_L = \begin{pmatrix}\overline{\psi}_{\nu_e} & \overline{\psi}_e\end{pmatrix}\left(\frac{1+\gamma_5}{2}\right), \tag{1.11b}$$

we can rewrite the Equation (1.10a) as:

$$J_\mu^+ = \begin{pmatrix}\overline{\psi}_{\nu_e} & \overline{\psi}_e\end{pmatrix}_L\gamma_\mu\begin{pmatrix}0 & 0\\ 1 & 0\end{pmatrix}\begin{pmatrix}\psi_{\nu_e}\\ \psi_e\end{pmatrix}_L = \overline{L}\gamma_\mu\tau_- L. \tag{1.12}$$

In the same way Equation (1.10b) becomes:

$$J_\mu^- = \overline{L}\gamma_\mu\tau_+ L. \tag{1.13}$$

We have defined

$$\tau_{\pm} = \frac{\tau_1 \pm i\tau_2}{2}\,; \tag{1.14}$$

where τ_i are the Pauli matrices defined in Equation (A.2). So the interaction between these charged currents and the charged vector bosons $W^{\pm}$ is given by the following lagrangian:

$$\mathcal{L}_{cc} = -\frac{g}{2\sqrt{2}}\left(J^{+}_{\mu}W^{\mu}_{-} + J^{-}_{\mu}W^{\mu}_{+}\right) = -\frac{g}{2\sqrt{2}}\overline{L}\gamma_{\mu}(\tau_{-}W^{\mu}_{-} + \tau_{+}W^{\mu}_{+})L\,. \tag{1.15}$$

We can now try to write the electromagnetic interaction term (1.2) within the same formalism. Because the electromagnetism preserves the parity, we have to take into account both left and right components of the interacting fields:

$$\mathcal{L}^{int}_{em} = e\left(\overline{\psi}_L\gamma_{\mu}\psi_L + \overline{\psi}_R\gamma_{\mu}\psi_R\right)A^{\mu}\,. \tag{1.16}$$

Using the definition in Equations (1.11), the left-handed part of the lagrangian (1.16) can be written as:

$$\overline{\psi}_L\gamma_{\mu}\psi_L = \left(\overline{\psi}_{\nu_e} \quad \overline{\psi}_e\right)_L\gamma_{\mu}\begin{pmatrix}0 & 0\\ 0 & 1\end{pmatrix}\begin{pmatrix}\psi_{\nu_e}\\ \psi_e\end{pmatrix}_L = \overline{L}\gamma_{\mu}\begin{pmatrix}0 & 0\\ 0 & 1\end{pmatrix}L\,, \tag{1.17}$$

and noticing that $\begin{pmatrix}0 & 0\\ 0 & 1\end{pmatrix} = \frac{1-\tau_3}{2}$,

$$\overline{\psi}_L\gamma_{\mu}\psi_L = \overline{L}\gamma_{\mu}\frac{1-\tau_3}{2}L\,. \tag{1.18}$$

Writing the right-handed component of the field as a $SU(2)$ singlet:

$$R = (\psi_e)_R\,; \tag{1.19}$$

the right-handed part of the lagrangian (1.16) becomes:

$$\overline{\psi}_R\gamma_{\mu}\psi_R = \overline{R}\gamma_{\mu}R\,. \tag{1.20}$$

In this way, the electromagnetic interaction lagrangian (1.16) becomes:

$$\begin{aligned}\mathcal{L}^{int}_{em} &= e\left(\overline{L}\gamma_{\mu}\frac{1-\tau_3}{2}L + \overline{R}\gamma_{\mu}R\right)A^{\mu} =\\ &= e\left(\frac{1}{2}\overline{L}\gamma_{\mu}L + \overline{R}\gamma_{\mu}R - \frac{1}{2}\overline{L}\gamma_{\mu}\tau_3 L\right)A^{\mu} =\\ &= -ej^{em}_{\mu}A^{\mu}\,.\end{aligned} \tag{1.21}$$

The electromagnetic current j^{em}_μ can be written in terms of two different currents:

$$j^{em}_\mu = j^3_\mu + \frac{j^Y_\mu}{2}\,; \tag{1.22a}$$

$$j^3_\mu = \bar{L}\gamma_\mu \frac{\tau_3}{2} L\,; \tag{1.22b}$$

$$j^Y_\mu = -\bar{L}\gamma_\mu L - 2\bar{R}\gamma_\mu R\,. \tag{1.22c}$$

These equations show that the electromagnetic current j^{em}_μ is a mixture of j^3_μ, partner of the charged currents, and of j^Y_μ, which is another neutral current.
With the following notation, I can unify the charged currents and j^3_μ:

$$j^i_\mu = \bar{L}\gamma_\mu \frac{\tau_i}{2} L\,. \tag{1.23}$$

Their associated charges Q^i span the Lie algebra of the symmetry group $SU(2)_L$, called *weak isospin*:

$$\left[Q^j, Q^k\right] = i\epsilon_{jkl} Q^l\,; \tag{1.24}$$

while the charge Q^Y associated to the current j^Y_μ commutes with Q^i

$$\left[Q^Y, Q^i\right] = 0\,, \tag{1.25}$$

and generates the group $U(1)$, called *hypercharge*. The connection between the electric charge Q_e, the Q^3 and the hypercharge Q^Y is given by the Gell-Mann–Nishijima relation:

$$Q_e = Q^3 + \frac{Q^Y}{2}\,. \tag{1.26}$$

Together, the Equations (1.24) and (1.25) form the Lie algebra of the symmetry group $SU(2)_L \otimes U(1)_Y$.
The results obtained tell us that if we want describe the electroweak interactions in the context of group theory, we have to introduce, near the charged currents, two other currents: a neutral current j^3_μ and a new one: the weak hypercharge j^Y_μ.
To build up a gauge theory from these elements, we have to start with a lagrangian possessing an $SU(2)_L \otimes U(1)_Y$ global symmetry. We start from the kinetic term

$$\mathcal{L} = \bar{L}\, i\gamma^\mu \mathcal{D}^L_\mu L + \bar{R}\, i\gamma^\mu \mathcal{D}^R_\mu R\,, \tag{1.27}$$

where $\mathcal{D}^L_\mu$ and $\mathcal{D}^R_\mu$ are the covariant derivatives for the left and right components:

$$\mathcal{D}^L_\mu = \partial_\mu - ig\frac{\tau_i}{2} W^i_\mu - i\frac{g'}{2} Y_\mu\,; \tag{1.28a}$$

$$\mathcal{D}^R_\mu = \partial_\mu - ig' Y_\mu\,. \tag{1.28b}$$

Notice that these are different: the right covariant derivative does not contains the generator of $SU(2)_L$ and its hypercharge is double that the left one. This is due to the fact that, under the action of $SU(2)_L \otimes U(1)_Y$ gauge group, the two chiral components, L and R, transform differently:

$$\begin{aligned} L &\longrightarrow L' = e^{\frac{i}{2}\boldsymbol{\tau}\cdot\boldsymbol{\alpha}(x)} e^{-i\beta(x)} L \\ R &\longrightarrow R' = e^{-2i\beta(x)} R \end{aligned} \tag{1.29}$$

Mass term, mixing left and right components of the fields, would destroy the global symmetry so does not appear in Equation (1.27). In fact, making clear the chiral components of the spinor field $\psi = \psi_L + \psi_R$ and using the properties of the projection operators (A.12):

$$m\overline{\psi}\psi = m\left(\overline{\psi}_L + \overline{\psi}_R\right)\left(\psi_L + \psi_R\right) = m\left(\overline{\psi}_L\psi_R + \overline{\psi}_R\psi_L\right), \tag{1.30}$$

it is possible to show that this mass term is not invariant under transformations of $SU(2)_L \otimes U(1)_Y$.
Expliciting the covariant derivatives in the kinetic lagrangian (1.27):

$$\begin{aligned} \mathcal{L} &= \overline{L}\, i\gamma^\mu \left(\partial_\mu - ig\frac{\tau_i}{2}W^i_\mu - i\frac{g'}{2}Y_\mu\right)L + \overline{R}\, i\gamma^\mu\left(\partial_\mu - ig'Y_\mu\right)R = \\ &= \overline{L}\, i\gamma^\mu\partial_\mu L + \overline{R}\, i\gamma^\mu\partial_\mu R + g\overline{L}\gamma^\mu\frac{\tau_i}{2}W^i_\mu L + \frac{g'}{2}\overline{L}\gamma^\mu Y_\mu L + g'\overline{R}\gamma^\mu Y_\mu R, \end{aligned} \tag{1.31}$$

and taking into account only the interaction term

$$\mathcal{L}_{int} = g\overline{L}\gamma^\mu\left(\frac{\boldsymbol{\tau}}{2}\cdot\boldsymbol{W}_\mu\right)L + \frac{g'}{2}\overline{L}\gamma^\mu Y_\mu L + g'\overline{R}\gamma^\mu Y_\mu R, \tag{1.32}$$

we have, as expected, the charged interaction with the $W^\pm$ bosons and the two neutral bosons W^3 and Y.
As we saw previously, the photon must be coupled with the electromagnetic current j^{em}_μ which is a linear combination of j^3_μ and j^Y_μ (1.22a). So we expect the photon field A_μ to be a linear combination of W^3 and Y. It is convenient to introduce a rotation of these two fields:

$$\begin{pmatrix} W^3 \\ Y \end{pmatrix} = \begin{pmatrix} \cos\theta & \sin\theta \\ -\sin\theta & \cos\theta \end{pmatrix}\begin{pmatrix} Z \\ A \end{pmatrix}, \tag{1.33}$$

where the mixing angle θ, called the Weinberg angle, can be identified through the requirement that the current coupled with A_μ is exactly the electromagnetic one with coupling constant $-e$.
Considering the part of $\mathcal{L}_{int}$ in Equation (1.32) involving the neutral couplings, remembering Equations (1.22b) and (1.22c) we obtain

$$\mathcal{L}_{nc} = gj^\mu_3 W^3_\mu - \frac{g'}{2}j^\mu_Y Y_\mu, \tag{1.34}$$

and using the Equation (1.33) we get

$$\mathcal{L}_{nc} = -\left(g \sin\theta\, j_3^\mu + \frac{g'}{2}\cos\theta\, j_Y^\mu\right) A_\mu + \left(g\cos\theta\, j_3^\mu - \frac{g'}{2}\sin\theta\, j_Y^\mu\right) Z_\mu\,. \tag{1.35}$$

The electromagnetic coupling is reproduced by requiring the conditions

$$g\sin\theta = g'\cos\theta = e\,, \tag{1.36}$$

and the relation between the two coupling constants g and g' is given by

$$\tan\theta = \frac{g'}{g}\,. \tag{1.37}$$

Using the Equation (1.22a) and the relation (1.37) we can rewrite the neutral current lagrangian of Equation (1.35) as:

$$\begin{aligned}\mathcal{L}_{nc} &= -e\left(j_3^\mu + \frac{j_Y^\mu}{2}\right) A_\mu + \left[g\cos\theta\, j_3^\mu - g'\sin\theta\,\left(j_{em}^\mu - j_3^\mu\right)\right] Z_\mu = \\ &= -e\, j_{em}^\mu A_\mu + \frac{g}{\cos\theta}\left(j_3^\mu - \sin^2\theta\, j_{em}^\mu\right) Z_\mu\,.\end{aligned} \tag{1.38}$$

We can identify

$$j_Z^\mu = j_3^\mu - \sin^2\theta\, j_{em}^\mu \tag{1.39}$$

as the neutral current coupled to the Z.
The approximate value for $\sin^2\theta$ evaluated from processes induced by neutral currents at low energy is $\sin^2\theta \approx 0.23$.

1.6 Spontaneous Symmetry Breaking

Putting together the results obtained from charged and neutral lagrangian, we have

$$\mathcal{L} = -\frac{g}{\sqrt{2}}\left(J_\mu^- W_+^\mu + J_\mu^+ W_-^\mu\right) - e\, j_{em}^\mu\, A_\mu + \frac{g}{\cos\theta} j_Z^\mu\, Z_\mu\,, \tag{1.40}$$

that does not contain the mass terms for the gauge fields $W_\mu^\pm$, A_μ and Z_μ. We have to find a way to give mass to the charged bosons $W_\mu^\pm$ and to the neutral one Z_μ, leaving A_μ massless. We have to request that the gauge symmetry associated with the photon field A_μ, the $U(1)_{em}$ gauge symmetry, does not get broken. It is not sufficient to completely break the $SU(2)_L$ symmetry and leave the $U(1)_Y$ untouched, because the field Y_μ does not coincide with the A_μ.
The most interesting consequence of spontaneous symmetry breaking is the Goldstone theorem. This theorem says that for any continuous symmetry spontaneously broken, there exist a massless particle called Goldstone boson. The number of these massless bosons is given by the following relation:

$$N_{Gb} = \dim(G) - \dim(H)\,,$$

where G is the global symmetry group of the theory and H is the subgroup of G leaving invariant the vacuum. The number of the Goldstone bosons correspond to the so called broken generators that do not leave the vacua of the theory invariant under the action of the gauge group: $\mathbf{T}_{BG}\,|0\rangle \neq |0\rangle$. One can understand the origin of the massless particles noticing that the broken generators allow transitions from a possible vacuum to another one. Since these states are degenerate, these transitions does not cost any energy. This implies that we must have massless particles: Goldstone bosons correspond to flat directions in the potential. In the electroweak case, there are three Goldstone bosons.

1.7 The Higgs mechanism: give mass to the gauge bosons

At first sight the spontaneous symmetry breaking mechanism does not seem to solve the mass problem. On the contrary we get more massless particles, the Goldstone bosons. However, once one couples spontaneous symmetry breaking to a gauge symmetry, things change: the Goldstone bosons disappear and, at the same time, the gauge bosons corresponding to the broken symmetries acquire mass. This is the so called Higgs mechanism.
In the electroweak case we need three broken symmetries in order to give mass to the W^+, W^- and Z. Since $SU(2)_L \otimes U(1)_Y$ has four generators, we will be left with one unbroken symmetry, that we should identify with the group of electromagnetism $U(1)_{em}$ in such a way to have the corresponding gauge particle, which is the photon, massless.
To realize this aim we have to introduce a set of scalar fields transforming in a convenient way under $SU(2)_L \otimes U(1)_Y$. The simplest choice turns out to be a complex representation of $SU(2)$: an Higgs doublet of dimension 2. The vacuum should be electrically neutral, so one of the components of the doublet must be neutral. Assuming this as the lower one, we can define the Higgs doublet as:

$$\Phi = \begin{pmatrix} \phi^+ \\ \phi^0 \end{pmatrix} . \tag{1.41}$$

Under the action of $SU(2)_L \otimes U(1)_Y$ group, Φ transforms as:

$$\Phi \longrightarrow \Phi' = e^{\frac{i}{2}\boldsymbol{\tau}\cdot\boldsymbol{\alpha}(x)} e^{i\beta(x)} \Phi \, . \tag{1.42}$$

The most general renormalizable lagrangian for Φ with the global $SU(2)_L \otimes U(1)_Y$ symmetry is:

$$\mathcal{L}_{\text{Higgs}} = \partial_\mu \Phi^\dagger \partial^\mu \Phi - \mu^2 \Phi^\dagger \Phi - \lambda \Big(\Phi^\dagger \Phi \Big)^2 , \tag{1.43}$$

with $\lambda > 0$ and $\mu^2 < 0$. The potential $V_{\text{Higgs}}(\Phi^\dagger\Phi) = \mu^2\Phi^\dagger\Phi + \lambda\left(\Phi^\dagger\Phi\right)^2$ has infinitely minima on the surface

$$|\Phi|^2_{\text{min}} = -\frac{\mu^2}{2\lambda} = \frac{v^2}{2}\,, \tag{1.44}$$

where $v^2 = -\frac{\mu^2}{\lambda}$. Now, we have to choose the vacuum. Charged scalar fields must have zero value in the vacuum, which must be electrically neutral. On the other hand, neutral scalar fields, which do not have electric charge, can have a non zero value in the vacuum, which is called vacuum expectation value. We can see that the Higgs doublet of Equation (1.41) have a non zero vacuum expectation value. In order to have an electrically neutral vacuum, the VEV of the Higgs doublet must be due to ϕ^0. Choosing the vacuum as the state

$$\langle\Phi\rangle = \frac{1}{\sqrt{2}}\begin{pmatrix}0\\ v\end{pmatrix}\,, \tag{1.45}$$

the symmetry $SU(2)_L \otimes U(1)_Y$ is spontaneously broken by this:

$$Q_1\langle\Phi\rangle = \frac{\tau_1}{2}\langle\Phi\rangle = \frac{1}{2\sqrt{2}}\begin{pmatrix}v\\ 0\end{pmatrix} \neq 0\,; \tag{1.46}$$

$$Q_2\langle\Phi\rangle = \frac{\tau_2}{2}\langle\Phi\rangle = -\frac{i}{2\sqrt{2}}\begin{pmatrix}v\\ 0\end{pmatrix} \neq 0\,; \tag{1.47}$$

$$Q_3\langle\Phi\rangle = \frac{\tau_3}{2}\langle\Phi\rangle = -\frac{1}{2\sqrt{2}}\begin{pmatrix}0\\ v\end{pmatrix} \neq 0\,; \tag{1.48}$$

$$Q_Y\langle\Phi\rangle = \langle\Phi\rangle \neq 0\,; \tag{1.49}$$

but

$$Q_e\langle\Phi\rangle = \left(Q_3 + \frac{Q_Y}{2}\right)\langle\Phi\rangle = \frac{1}{\sqrt{2}}\begin{pmatrix}1 & 0\\ 0 & 0\end{pmatrix}\begin{pmatrix}0\\ v\end{pmatrix} = 0\,. \tag{1.50}$$

Therefore the vacuum is invariant under gauge transformations of the type

$$e^{i\alpha Q_e}\,\langle\Phi\rangle = \langle\Phi\rangle\,,$$

that belong to the group $U(1)_{\text{em}}$. This invariance guarantees the existence of a massless gauge boson associated with the symmetry group $U(1)_{\text{em}}$, which is identified with the photon.
In order to derive the physical properties of the particles resulting from the spontaneous breaking of the $SU(2)_L \otimes U(1)_Y$ symmetry, it is convenient to write the Higgs doublet as:

$$\Phi = \frac{1}{\sqrt{2}}\exp\left\{\frac{i}{2}\frac{\xi\cdot\boldsymbol{\tau}}{v}\right\}\begin{pmatrix}0\\ v+H\end{pmatrix} \tag{1.51}$$

where H describes the physical Higgs boson, $\boldsymbol{\tau} = \begin{pmatrix}\tau_1 & \tau_2 & \tau_3\end{pmatrix}$ are the Pauli matrices and $\boldsymbol{\xi} = \begin{pmatrix}\xi_1 & \xi_2 & \xi_3\end{pmatrix}$ are the Goldstone bosons. It can be rotated away by a gauge transformation like (1.42) with

$$\boldsymbol{\alpha}(x) = -\frac{\boldsymbol{\xi}}{v}\,; \tag{1.52a}$$

$$\beta(x) = 0\,. \tag{1.52b}$$

The transformations in Equations (1.52) define the so called *unitary gauge*, in which the physical states of the theory appear explicitly. In the unitary gauge, the Higgs doublets reads:

$$\Phi = \frac{1}{\sqrt{2}}\begin{pmatrix}0\\ v + H\end{pmatrix}\,. \tag{1.53}$$

Now we promote the global $SU(2)_L \otimes U(1)_Y$ symmetry to a local one by introducing the covariant derivative. Remembering that $\Phi \in SU(2)_L \otimes U(1)_Y$, we have

$$\mathcal{D}^H_\mu = \partial_\mu - i\frac{g}{2}\boldsymbol{\tau}\cdot\boldsymbol{W}_\mu - i\frac{g'}{2}Y_\mu\,. \tag{1.54}$$

In terms of the physical fields, Equation (1.54) becomes

$$\mathcal{D}^H_\mu = \partial_\mu - i\frac{g}{\sqrt{2}}(\tau_+ W^-_\mu + \tau_- W^+_\mu) - ig\frac{\tau_3}{2}W^3_\mu - i\frac{g'}{2}Y_\mu\,. \tag{1.55}$$

So, the kinetic term of Equation (1.43) becomes

$$(\mathcal{D}^H_\mu\Phi)^\dagger(\mathcal{D}^{H\mu}\Phi) = \left|\frac{1}{\sqrt{2}}\begin{pmatrix}0\\ \partial_\mu H\end{pmatrix} - i\frac{g}{2}\begin{pmatrix}(H+v)W^-_\mu\\ -\frac{H+v}{\sqrt{2}}\left(W^3_\mu - \frac{g'}{g}Y_\mu\right)\end{pmatrix}\right|^2\,. \tag{1.56}$$

Inverting now the relation (1.33):

$$Z_\mu = \cos\theta\, W^3_\mu - \sin\theta\, Y_\mu\,; \tag{1.57a}$$

$$A_\mu = \sin\theta\, W^3_\mu + \cos\theta\, Y_\mu\,, \tag{1.57b}$$

and using the relation (1.37) in the kinetic term of Equation (1.56), we obtain the following expression for the Higgs lagrangian (1.43):

$$\begin{aligned}\mathcal{L}_H &= \frac{1}{2}(\partial_\mu H)(\partial^\mu H) - \lambda v^2 H^2 - \lambda v H^3 - \frac{\lambda}{4}H^4 + \\ &+ \frac{1}{8}\left(1 + \frac{H}{v}\right)^2\left(2g^2v^2W^-_\mu W^{+\mu} + \frac{g^2v^2}{\cos^2\theta}Z_\mu Z^\mu\right) = \\ &= \frac{1}{2}(\partial_\mu H)(\partial^\mu H) - \lambda v^2 H^2 - \lambda v H^3 - \frac{\lambda}{4}H^4 + \\ &+ \frac{g^2}{4}(v+H)^2W^-_\mu W^{+\mu} + \frac{g^2}{8\cos^2\theta}(v+H)^2 Z_\mu Z^\mu\,.\end{aligned} \tag{1.58}$$

Finally the mass of vector bosons appears [15]:

$$m_W = \sqrt{\frac{g^2 v^2}{4}} = 80.379 \pm 0.012 \text{ GeV}; \tag{1.59a}$$

$$m_Z = \sqrt{\frac{g^2 v^2}{4\cos^2\theta}} = \frac{m_W}{\cos\theta} = 91.1876 \pm 0.0021 \text{ GeV}, \tag{1.59b}$$

together with the mass of the Higgs boson [8, 9],

$$m_H = \sqrt{2\lambda v^2} = \sqrt{-2\mu^2} = 125.18 \pm 0.16 \text{ GeV}. \tag{1.60}$$

Remembering the relation (1.9) between the Fermi constant G_F and the weak coupling g, knowing the value of m_W^2, we obtain the value of the Higgs vacuum expectation value:

$$v \approx 246 \text{ GeV}. \tag{1.61}$$

1.8 Yukawa sector: give mass to the leptons

We have seen that does not exist an explicit mass term for fermions in the weak lagrangian (1.27), because it will break the gauge symmetry. To give mass to the fermions, we use again the Higgs mechanism through an Yukawian coupling. With the $SU(2)$ doublet L, Φ and the $SU(2)$ singlet R, we can construct the general lagrangian:

$$\mathcal{L}_y = -y_e\left(\overline{L}\Phi R + \overline{R}\Phi^\dagger L\right), \tag{1.62}$$

which, by the transformation laws (1.29) of the chiral components and (1.42) of the field Φ, is shown to be invariant under the action of $SU(2)_L \otimes U(1)_Y$ group. The mass term for the fermions can be read by writing Φ in the unitary gauge (1.53). Making this, the lagrangian in Equation (1.62) becomes:

$$\begin{aligned}
\mathcal{L}_y &= -y_e\left[\overline{L}\begin{pmatrix} 0 \\ \frac{v+H}{\sqrt{2}} \end{pmatrix} R + \overline{R}\begin{pmatrix} 0 & \frac{v+H}{\sqrt{2}} \end{pmatrix} L\right] = \\
&= -y_e\left[\begin{pmatrix} \overline{\psi}_\nu & \overline{\psi}_e \end{pmatrix}_L \begin{pmatrix} 0 \\ \frac{v+H}{\sqrt{2}} \end{pmatrix} \psi_{eR} + \overline{\psi}_{eR}\begin{pmatrix} 0 & \frac{v+H}{\sqrt{2}} \end{pmatrix} \begin{pmatrix} \psi_\nu \\ \psi_e \end{pmatrix}_L\right] = \\
&= -y_e\left[\overline{\psi}_{eL}\frac{v}{\sqrt{2}}\psi_{eR} + \overline{\psi}_{eL}\frac{H}{\sqrt{2}}\psi_{eR} + \overline{\psi}_{eR}\frac{v}{\sqrt{2}}\psi_{eL} + \overline{\psi}_{eR}\frac{H}{\sqrt{2}}\psi_{eL}\right].
\end{aligned} \tag{1.63}$$

The neutrino remains massless while the electron acquires mass:

$$m_e = \frac{y_e v}{\sqrt{2}}. \tag{1.64}$$

y_e is a coupling parameter related to the electron. Each fermion to which we want to give mass has its own parameter.

Chapter 2

Neutrinos nature

> In due modi si raggiunge Despina: per nave o per cammello. La città si presenta differente a chi viene da terra e a chi dal mare.
>
> Italo Calvino
> *Le città invisibili*

In the Standard Model of electroweak interactions described in Chapter 1, we saw that, following the Higgs mechanism, only leptons acquire mass, while neutrinos stay massless. In fact, the Standard Model describes neutrinos as neutral and massless fermions. Today we know that neutrinos have very small masses, different from zero. There are at least three flavors of very light neutrinos, ν_e , ν_μ and ν_τ which are left-handed, and their antiparticles $\overline{\nu}_e$, $\overline{\nu}_\mu$ and $\overline{\nu}_\tau$ which are right-handed. Neutrinos of each flavor participate in reactions in which the charged leptons of the corresponding flavor are involved: these reactions are mediated by charged bosons $W^{\pm}$. Neutrinos can also participate in neutral current reactions mediated by Z boson.
We are so much interested in neutrinos because these play a very important role in various branches of physics as well as in astrophysics and cosmology. The smallness of neutrino mass is very likely related to existence of new, yet unexplored, mass scales in particle physics, perhaps related to the unification of forces.

2.1 Dirac neutrino

2.1.1 Dirac mass term

As we have seen, a mass term like that of Equation (1.30), cannot be included in the electroweak lagrangian because, mixing left and right components of the fields, would destroy the global symmetry $SU(2)_L \otimes U(1)_Y$. The presence of a non zero Dirac mass requires a particle that has both left and right-handed chiral states: the Dirac mass can be viewed, in fact, as the coupling constant between the two chiral components. To integrate this into the Standard Model of electroweak interactions, we need the Higgs particle, which can couple with both chirality. Since we know that neutrino is chirally left-handed, there is a good reason to suppose that neutrino must be massless: does not seem to exist right-handed state to couple to it for the mass term construction. However, we know that neutrino has a small mass, so there must be a right-handed one which only shows up in the Standard Model to give the neutrino mass, but otherwise cannot be observed, because the weak interaction does not couple to it.
So, Dirac neutrino mass term can be generated with the same Higgs mechanism that gives masses to charged leptons. To do this, is needed to extend the Standard Model, introducing the right-handed neutrino fields $\nu_{\alpha R}$ with α = e, μ, τ. Such a model is called the *minimally extended Standard Model* [16]. The right-handed neutrino fields are *sterile*, because these do not take part in weak interactions. On the other hand, the left-handed neutrino fields that partecipate in weak interactions are usually called *active*. The number of sterile right-handed neutrino fields is not constrained by the theory, and the introduction of three right-handed neutrino fields, one for each lepton flavor, is not the only minimal extension of the Standard Model: the presence of more or less right-handed neutrino fields cannot be excluded.
In the minimally extended Standard Model, restricted only to one flavor:

$$L = \begin{pmatrix} \nu_L \\ l_L \end{pmatrix}, \qquad l_R, \qquad \nu_R$$

the lagrangian of Equation (1.62) can be written as:

$$\mathcal{L}_y = -y_l\left(\overline{L}\Phi\, l_R + \overline{l}_R\, \Phi^\dagger L\right) - y_\nu\left(\overline{L}\widetilde{\Phi}\, \nu_R + \overline{\nu}_R\, \widetilde{\Phi}^\dagger L\right), \tag{2.1}$$

where Φ is given by the Equation (1.53) and $\widetilde{\Phi}$ is defined as

$$\widetilde{\Phi} = \frac{1}{\sqrt{2}}\begin{pmatrix} v + H \\ 0 \end{pmatrix}. \tag{2.2}$$

Writing explicitly, the lagrangian (2.1) assumes the following form:

$$\begin{aligned}\mathcal{L}_L = &-\frac{y_l}{\sqrt{2}}\left[(\overline{\nu}_L \quad \overline{l}_L)\begin{pmatrix}0\\ \nu+H\end{pmatrix}l_R + \overline{l}_R(0 \quad \nu+H)\begin{pmatrix}\nu_L\\ l_L\end{pmatrix}\right]- \\ &-\frac{y_\nu}{\sqrt{2}}\left[(\overline{\nu}_L \quad \overline{l}_L)\begin{pmatrix}\nu+H\\ 0\end{pmatrix}\nu_R + \overline{\nu}_R(\nu+H \quad 0)\begin{pmatrix}\nu_L\\ l_L\end{pmatrix}\right] = \\ &= -\left(\frac{\nu+H}{\sqrt{2}}\right)\left[y_l(\overline{l}_R l_L + \overline{l}_L l_R) + y_\nu(\overline{\nu}_R\nu_L + \overline{\nu}_L\nu_R)\right].\end{aligned} \tag{2.3}$$

Together with the mass of the lepton l, already seen in Equation (1.64) for the electron case, the mass of the neutrino appears:

$$m_\nu = \frac{y_\nu \nu}{\sqrt{2}}. \tag{2.4}$$

Generalizing to the three flavors case:

$$L'_e = \begin{pmatrix}\nu'_{eL}\\ e'_L\end{pmatrix}, \qquad e'_R, \qquad \nu'_{eR}; \tag{2.5a}$$

$$L'_\mu = \begin{pmatrix}\nu'_{\mu L}\\ \mu'_L\end{pmatrix}, \qquad \mu'_R, \qquad \nu'_{\mu R}; \tag{2.5b}$$

$$L'_\tau = \begin{pmatrix}\nu'_{\tau L}\\ \tau'_L\end{pmatrix}, \qquad \tau'_R, \qquad \nu'_{\tau R}, \tag{2.5c}$$

the lagrangian (2.1) becomes

$$\mathcal{L}_y = -\sum_{\alpha,\beta=e,\mu,\tau}\left(Y'^l_{\alpha\beta}\,\overline{L}'_{\alpha L}\Phi\, l'_{\beta R} + Y'^\nu_{\alpha\beta}\,\overline{L}'_{\alpha L}\widetilde{\Phi}\,\nu'_{\beta R}\right) + h.c., \tag{2.6}$$

where Y'^l and Y'^ν are the matrices of Yukawa couplings for charged leptons and neutrinos, respectively. In the unitary gauge, this lagrangian can be written in matrix form as:

$$\mathcal{L}_y = -\frac{\nu+H}{\sqrt{2}}\left(\overline{l}'_L Y'^l l'_R + \overline{\nu}'_L Y'^\nu \nu'_R\right) + h.c., \tag{2.7}$$

where we have introduced the follow notation:

$$l'_L = \begin{pmatrix}e'_L\\ \mu'_L\\ \tau'_L\end{pmatrix}; \qquad l'_R = \begin{pmatrix}e'_R\\ \mu'_R\\ \tau'_R\end{pmatrix}; \tag{2.8a}$$

$$\nu'_L = \begin{pmatrix}\nu'_{eL}\\ \nu'_{\mu L}\\ \nu'_{\tau L}\end{pmatrix}; \qquad \nu'_R = \begin{pmatrix}\nu'_{eR}\\ \nu'_{\mu R}\\ \nu'_{\tau R}\end{pmatrix}. \tag{2.8b}$$

The Dirac mass matrices for leptons and neutrinos become, respectively,

$$M^{l} = \frac{v}{\sqrt{2}} Y'^{l}\,; \tag{2.9a}$$

$$M^{\nu} = \frac{v}{\sqrt{2}} Y'^{\nu}\,. \tag{2.9b}$$

Both mass matrices M^{l} and M^{ν} can be diagonalized by diagonalizing the Yukawa couplings matrices Y'^{l} and Y'^{ν} through biunitary transformations. Defining the 3×3 unitary matrices V_j^{l} and V_j^{ν} as follow:

$$(V_j^{l})^{-1} = V_j^{l\dagger}\,; \qquad j = L, R \tag{2.10a}$$

$$(V_j^{\nu})^{-1} = V_j^{\nu\dagger}\,; \qquad j = L, R \tag{2.10b}$$

we can perform the biunitary transformations of the Yukawa coupling matrices

$$V_L^{l\dagger}\, Y'^{l}\, V_R^{l} = Y^{l}\,, \qquad \text{with} \qquad Y^{l}_{\alpha\beta} = y^{l}_{\alpha}\, \delta_{\alpha\beta}\,, \qquad \alpha, \beta = e, \mu, \tau\,; \tag{2.11}$$

$$V_L^{\nu\dagger}\, Y'^{\nu}\, V_R^{\nu} = Y^{\nu}\,, \qquad \text{with} \qquad Y^{\nu}_{ij} = y^{\nu}_{i}\, \delta_{ij}\,, \qquad i, j = 1, 2, 3\,, \tag{2.12}$$

with y^{l}_{α} and y^{ν}_{i} real and positive. Defining the massive chiral leptons and neutrinos fields as follow:

$$l_L = V_L^{l\dagger}\, l'_L = \begin{pmatrix} e_L \\ \mu_L \\ \tau_L \end{pmatrix}\,; \qquad l_R = V_R^{l\dagger}\, l'_R = \begin{pmatrix} e_R \\ \mu_R \\ \tau_R \end{pmatrix}\,; \tag{2.13a}$$

$$n_L = V_L^{\nu\dagger} \nu'_L = \begin{pmatrix} \nu_{1L} \\ \nu_{2L} \\ \nu_{3L} \end{pmatrix}\,; \qquad n_R = V_R^{\nu\dagger} \nu'_R = \begin{pmatrix} \nu_{1R} \\ \nu_{2R} \\ \nu_{3R} \end{pmatrix}\,, \tag{2.13b}$$

the diagonalized lagrangian (2.7) becomes

$$\begin{aligned} \mathcal{L}_y &= -\frac{v + H}{\sqrt{2}} \left(\bar{l}_L Y^{l} l_R + \bar{n}_L Y^{\nu} n_R \right) + h.c. = \\ &= -\frac{v + H}{\sqrt{2}} \left(\sum_{\alpha = e,\mu,\tau} y^{l}_{\alpha}\, \bar{l}_{\alpha L}\, l_{\alpha R} + \sum_{k=1}^{3} y^{\nu}_{k}\, \bar{\nu}_{kL}\, \nu_{kR} \right) + h.c. \end{aligned} \tag{2.14}$$

Using the Dirac charged lepton and neutrino fields:

$$l_\alpha = l_{\alpha L} + l_{\alpha R} \qquad \alpha = e, \mu, \tau \tag{2.15a}$$

$$\nu_k = \nu_{kL} + \nu_{kR} \qquad k = 1, 2, 3 \tag{2.15b}$$

we finally obtain

$$\begin{aligned}\mathcal{L}_y = &- \sum_{\alpha=e,\mu,\tau} \frac{y^l_\alpha v}{\sqrt{2}} \bar{l}_\alpha l_\alpha - \sum_{k=1}^{3} \frac{y^\nu_k v}{\sqrt{2}} \bar{\nu}_k \nu_k - \\ &- \sum_{\alpha=e,\mu,\tau} \frac{y^l_\alpha}{\sqrt{2}} \bar{l}_\alpha l_\alpha H - \sum_{k=1}^{3} \frac{y^\nu_k}{\sqrt{2}} \bar{\nu}_k \nu_k H \,.\end{aligned} \tag{2.16}$$

This result generalizes that of Equation (2.3). The neutrino masses are given by:

$$m_k = \frac{y^\nu_k v}{\sqrt{2}} \,. \tag{2.17}$$

Note that the neutrino masses that we have obtained with this mechanism are proportional to the Higgs vacuum expectation value v (1.61), as the masses of charged leptons. There is no explanation of the very small values of the eigenvalues y^ν_k of the Higgs-neutrino Yukawa coupling matrix that are needed. In fact, the Higgs mechanism leaves completely open the question of the value of the Yukawa couplings with the Higgs of all particles. This mystery leads us to believe that the Standard Model must be considered as an effective theory, obtained from the low energy limit of a more complete theory, maybe the GUT one.

2.1.2 Three Dirac neutrinos mixing

In the Standard Model, the flavor neutrino fields are also mass eigenstates because any linear combination of massless fields is a massless field. In theory beyond the Standard Model, in which neutrinos are massive, flavor neutrino fields are, in general, not mass eigenstates but their linear combinations. This is the phenomenon of neutrino mixing.
The data imply the presence of neutrino mixing in the vector charged weak current of Equations (1.10) [17]:

$$J^+_\rho = \sum_{\alpha=e,\mu,\tau} \bar{l}'_{\alpha L} \gamma_\rho \nu'_{\alpha L} \,; \tag{2.18a}$$

$$J^-_\rho = \sum_{\alpha=e,\mu,\tau} \bar{\nu}'_{\alpha L} \gamma_\rho l'_{\alpha L} \,. \tag{2.18b}$$

Using the mass chiral leptons and neutrinos fields defined in Equations (2.13) to express primate ones

$$l'_L = V^l_L \, l_L \,; \qquad \bar{l}'_L = \bar{l}_L \, V^{l\dagger}_L \,; \tag{2.19a}$$

$$\nu'_L = V^\nu_L \, n_L \,; \qquad \bar{\nu}'_L = \bar{n}_L V^{\nu\dagger}_L \,, \tag{2.19b}$$

we can rewrite the weak currents of Equations (2.18) as follow

$$J_\rho^+ = \bar{l}_L V_L^{l\dagger} \gamma_\rho V_L^\nu \, n_L \, ; \tag{2.20a}$$

$$J_\rho^- = \bar{n}_L V_L^{\nu\dagger} \gamma_\rho V_L^l \, l_L \, . \tag{2.20b}$$

Defining the mixing matrix in the lepton sector

$$U = V_L^{l\dagger} V_L^\nu \, , \tag{2.21}$$

the leptonic weak charged currents of Equations (2.20) reads:

$$J_\rho^+ = \bar{l}_L \gamma_\rho U \, n_L \, ; \tag{2.22a}$$

$$J_\rho^- = \bar{n}_L \gamma_\rho U^\dagger l_L \, . \tag{2.22b}$$

It is customary to define left-handed flavor neutrino fields as

$$\nu_L = U n_L = V_L^{l\dagger} \nu'_L = \begin{pmatrix} \nu_{eL} \\ \nu_{\mu L} \\ \nu_{\tau L} \end{pmatrix} ; \tag{2.23a}$$

$$\bar{\nu}_L = \overline{(U n_L)} = \bar{\nu}'_L V_L^l = \begin{pmatrix} \bar{\nu}_{eL} & \bar{\nu}_{\mu L} & \bar{\nu}_{\tau L} \end{pmatrix} , \tag{2.23b}$$

which allow us to write the leptonic weak charged currents as

$$J_\rho^+ = \bar{l}_L \gamma_\rho (U n_L) = \bar{l}_L \gamma_\rho \nu_L \, ; \tag{2.24a}$$

$$J_\rho^- = \left(\bar{n}_L U^\dagger \right) \gamma_\rho l_L = \bar{\nu}_L \gamma_\rho l_L \, . \tag{2.24b}$$

Making explicit the sum over the leptons, the weak charged lagrangian is written as:

$$\mathcal{L}_{cc} = -\frac{g}{2\sqrt{2}} \sum_{l=e,\mu,\tau} \left(\bar{l}_L \gamma^\rho \, \nu_{lL} W_\rho^- + \bar{\nu}_{lL} \gamma^\rho l_L W_\rho^+ \right) , \tag{2.25}$$

where the flavor neutrino fields ν_{lL}, according to the Equation (2.23a), are given by

$$\nu_{lL} = \sum_{k=1}^{3} U_{lk} \, n_{kL} \, , \tag{2.26}$$

where n_{kL} is the left-handed component of the massive neutrino field (2.13b) having a mass m_k, and U is the unitary mixing matrix called the Pontecorvo-Maki-Nakagawa-Sakata neutrino mixing matrix.
As we can see from Equation (2.25), the right-handed components ν_{lR} of the massive Dirac neutrino fields do not enter in the weak charged lagrangian. Hence, they represent sterile degrees of freedom, that do not take part in weak interactions. It is possible to define superpositions of right-handed neutrino fields, in analogy to the definition of left-handed flavor neutrino fields of Equations

(2.23). However, such a definition would be useless, because of the sterilty of right-handed neutrino fields. Since the mixing of the left-handed neutrino fields (2.23) is independent of the right-handed ones, the active and sterile degrees of freedom remain decoupled in the presence of Dirac mixing and oscillations between active and sterile states is not possible.
In general, a unitary $N \times N$ matrix depends on N^2 independent real parameters. These can be divided into

- $\frac{N(N-1)}{2}$ mixing angles,
- $\frac{N(N+1)}{2}$ phases.

Hence, the neutrino mixing matrix with $N = 3$ can be written in terms of three mixing angles and six phases. However, not all of these are physical observables. As in the quarks case, five of six phases in the unitary mixing matrix are unphysical because they can be eliminated by rephasing the neutrino charged lepton fields. In general, the number of physical phases is given by

$$\frac{N(N+1)}{2} - (2N-1) = \frac{(N-1)(N-2)}{2}\,.$$

So, in case of $N = 3$, there is only one physical phase. The total number of physical parameters in the neutrino mixing matrix with $N = 3$ is

$$\frac{N(N-1)}{2} + \frac{(N-1)(N-2)}{2} = 4\,.$$

A convenient parametrization of the Dirac neutrino mixing matrix is given by the following one:

$$U = \begin{pmatrix} c_{12}c_{13} & s_{12}c_{13} & s_{13}e^{-i\delta_{13}} \\ -s_{12}c_{23} - c_{12}s_{23}s_{13}e^{i\delta_{13}} & c_{12}c_{23} - s_{12}s_{23}s_{13}e^{i\delta_{13}} & s_{23}c_{13} \\ s_{12}s_{23} - c_{12}c_{23}s_{13}e^{i\delta_{13}} & -c_{12}s_{23} - s_{12}c_{23}s_{13}e^{i\delta_{13}} & c_{23}c_{13} \end{pmatrix} \tag{2.27}$$

where $c_{ij} = \cos\theta_{ij}$ and $s_{ij} = \sin\theta_{ij}$. The three mixing angles θ_{12}, θ_{13}, θ_{23} take values in the range $0 \leqslant \theta_{ij} \leqslant \frac{\pi}{2}$ and δ_{13} is the CP-violating phase with a value in the range $0 \leqslant \delta_{13} \leqslant 2\pi$.
An interesting question is why the mixing is always applied to the neutrinos whereas the charged leptons are treated as particles with definite mass. The reason is that the only characteristic that distinguishes the three charged leptons is their mass, and the flavor of a charged lepton is identified by measuring its mass. The mass determines its kinematical properties and its decay modes. Hence, charged leptons with a definite flavor are, by definition, particles with definite mass. On the other hand, neutrinos can be detected only indirectly by

identifying the charged particles produced in weak interactions and the flavor of a neutrino created or destroyed in a charged current weak interaction process is, by definition, the flavor of the associated charged lepton. Therefore, flavor neutrinos are not required to have a definite mass and the mixing implies that they are superpositions of neutrinos with definite masses.

2.1.3 Lepton number in Dirac case

For massive Dirac neutrinos, even if the flavor lepton numbers L_e, L_μ, L_τ are not conserved, the total one $L = L_e + L_\mu + L_\tau$, associated through Noether's theorem with the global $U(1)$ gauge transformations, is conserved. The total lagrangian is, in fact, invariant under the global $U(1)$ gauge transformations:

$$\nu_{kL} \longrightarrow e^{i\varphi}\nu_{kL} \qquad \nu_{kR} \longrightarrow e^{i\varphi}\nu_{kR} \qquad k = 1,2,3\,; \tag{2.28a}$$

$$l_{\alpha L} \longrightarrow e^{i\varphi}l_{\alpha L} \qquad l_{\alpha R} \longrightarrow e^{i\varphi}l_{\alpha R} \qquad \alpha = e,\mu,\tau\,, \tag{2.28b}$$

with the same phase φ for the independent chiral neutrino and charged lepton fields. Neutrinos and negatively charged leptons have $L = +1$, whereas antineutrinos and positively charged leptons have $L = -1$. The lepton quantum number is different for neutrinos and antineutrinos. Hence, we see that the Dirac character of massive neutrinos, which implies that neutrinos and antineutrinos are different particles, is closely related to the invariance of the total lagrangian under the global $U(1)$ gauge transformations of Equations (2.28).

2.2 Majorana neutrino

2.2.1 Majorana mass term

A Majorana mass is generated by a Lagrangian mass term with only one chiral fermion field. We can start to consider a single neutrino flavor ν. Since it is left-handed, we use the left-handed chiral field ν_L. We can start from a mass term such that of Equation (1.30). In order to construct a mass term using only ν_L, we must find a right-handed function of ν_L which can be substituted in place of ν_R in Equation (1.30). From the Majorana condition (B.14) we have

$$\nu_L^c = \mathcal{C}\overline{\nu}_L^T\,, \tag{2.29}$$

and, since it is right-handed, the couplings $\overline{\nu}_L^c\nu_L$ and $\overline{\nu}_L\nu_L^c$ do not vanish. So, replacing ν_R and $\overline{\nu}_R$ in Equation (1.30) we obtain the Majorana mass term:

$$\mathcal{L}_M^{\text{mass}} = -\frac{m}{2}(\overline{\nu}_L^c\nu_L + \overline{\nu}_L\nu_L^c)\,. \tag{2.30}$$

The factor $\frac{1}{2}$ was introduced to avoid double counting due to the fact that ν_L^c and $\overline{\nu}_L$ are not independent. The full Majorana lagrangian, consisting of the kinetic terms for ν_L^c and ν_L and of the Majorana mass term (2.30), is

$$\mathcal{L}_M = \frac{1}{2}\left[\overline{\nu}_L i\gamma^\mu \overleftrightarrow{\partial_\mu} \nu_L + \overline{\nu}_L^c i\gamma^\mu \overleftrightarrow{\partial_\mu} \nu_L^c - m(\overline{\nu}_L^c \nu_L + \overline{\nu}_L \nu_L^c)\right]. \tag{2.31}$$

To derive the Euler-Lagrange field equation (B.2) it useful to express ν_L^c using the relation (2.29), and, taking its Hermitian conjugated

$$\overline{\nu}_L^c = \left(\mathcal{C}\overline{\nu}_L^T\right)^\dagger \gamma^0 = \nu_L^T \gamma^{0T} \mathcal{C}^\dagger \gamma^0, \tag{2.32}$$

and making use of the charge conjugation matrix property (B.8c), express $\overline{\nu}_L^c$ as:

$$\overline{\nu}_L^c = -\nu_L^c \mathcal{C}^\dagger. \tag{2.33}$$

Then, the lagrangian (2.31) can be written as

$$\begin{aligned}\mathcal{L}_M &= \frac{1}{2}\left[\overline{\nu}_L i\gamma^\mu \overleftrightarrow{\partial_\mu} \nu_L - \nu_L^T \mathcal{C}^\dagger i\gamma^\mu \overleftrightarrow{\partial_\mu} \mathcal{C}\overline{\nu}_L^T - m\left(-\nu_L^T \mathcal{C}^\dagger \nu_L + \overline{\nu}_L \mathcal{C}\overline{\nu}_L^T\right)\right] = \\ &= \frac{1}{2}\left[\overline{\nu}_L i\gamma^\mu \overleftrightarrow{\partial_\mu} \nu_L + \nu_L^T i\gamma^\mu \overleftrightarrow{\partial_\mu} \overline{\nu}_L^T - m\left(-\nu_L^T \mathcal{C}^\dagger \nu_L + \overline{\nu}_L \mathcal{C}\overline{\nu}_L^T\right)\right].\end{aligned} \tag{2.34}$$

From Equation (B.2) we obtain the Majorana field equation for ν_L:

$$i\gamma^\mu \partial_\mu \nu_L = m\mathcal{C}\overline{\nu}_L^T. \tag{2.35}$$

Defining the Majorana field ν as done in Equation (B.13), the lagrangian (2.31) can be written as

$$\mathcal{L}_M = \frac{1}{2}\overline{\nu}\left(i\gamma^\mu \overleftrightarrow{\partial_\mu} - m\right)\nu, \tag{2.36}$$

and has the same form of the Dirac lagrangian (B.1), apart from the factor $\frac{1}{2}$. The Majorana mass term represents a physical effect beyond the Standard Model. In fact, neutrinos in the Standard Model cannot have Majorana masses because it is not possible to have a renormalizable lagrangian term which can generate a Majorana neutrino mass.

2.2.2 Three Majorana neutrinos mixing

Let us consider now three generations of massive Majorana neutrinos. From the definition of the left-handed flavor neutrino fields $\boldsymbol{\nu}'_L$ of Equation (2.8b), we can construct the Majorana mass term:

$$\mathcal{L}_M^{\text{mass}} = \frac{1}{2}\left(\boldsymbol{\nu}_L'^T \mathcal{C}^\dagger M^L \boldsymbol{\nu}'_L + \text{h.c.}\right) = \frac{1}{2}\sum_{\alpha,\beta=e,\mu,\tau}\left(\nu_{\alpha L}'^T \mathcal{C}^\dagger M^L_{\alpha\beta} \nu'_{\beta L} + \text{h.c.}\right). \tag{2.37}$$

In general, the matrix M^L is a complex symmetric matrix. As in the case of Dirac neutrinos, the fields of massive neutrinos are obtained diagonalizing the Majorana mass term (2.37). The matrix M^L can be diagonalized through a unitary matrix V_L^ν like that of Equation (2.10b):

$$(V_L^\nu)^T M^L V_L^\nu = M\,, \qquad \text{with} \qquad M_{jk} = m_j\,\delta_{jk}\,, \qquad j,k = 1,2,3\,, \tag{2.38}$$

with m_j real and positive masses. Defining the massive left-handed neutrino field $\mathbf{n}_L$ as done in Equation (2.13b) and using the Equation (2.38), the lagrangian in Equation (2.37) can be written in diagonal form:

$$\begin{aligned}\mathcal{L}_M^{\text{mass}} &= \frac{1}{2}\Big(\mathbf{n}_L^T \mathcal{C}^\dagger M \mathbf{n}_L + \text{h.c.}\Big) = \frac{1}{2}\sum_{k=1}^{3}\Big(m_k \nu_{kL}^T \mathcal{C}^\dagger \nu_{kL} + \text{h.c.}\Big) = \\ &= -\frac{1}{2}(\overline{\mathbf{n}}_L^c M \mathbf{n}_L + \text{h.c.}) = -\frac{1}{2}\sum_{k=1}^{3}(m_k \overline{\nu}_{kL}^c \nu_{kL} + \text{h.c.})\,.\end{aligned} \tag{2.39}$$

The Majorana fields of massive neutrinos

$$\nu_k = \nu_{kL} + \nu_{kL}^c\,, \tag{2.40}$$

satisfy the Majorana condition

$$\nu_k^c = \nu_k\,, \tag{2.41}$$

and allow to write the three generation Majorana lagrangian:

$$\mathcal{L}_M = \frac{1}{2}\sum_{k=1}^{3}\overline{\nu}_k\Big(i\gamma^\mu \overleftrightarrow{\partial_\mu} - m_k\Big)\nu_k = \frac{1}{2}\overline{\mathbf{n}}\Big(i\gamma^\mu \overleftrightarrow{\partial_\mu} - M\Big)\mathbf{n}\,, \tag{2.42}$$

with the vector of massive Majorana neutrino fields

$$\mathbf{n} = \begin{pmatrix}\nu_1\\ \nu_2\\ \nu_3\end{pmatrix}. \tag{2.43}$$

As in the case of Dirac neutrinos, the effects of the mixing are contained in the leptonic weak charge currents of Equations (2.22). We can define the mixing matrix U in the same way of Equation (2.21) and the left-handed flavor neutrino fields $\overline{\nu}_L$ as in Equation (2.23a), in order to write the leptonic weak charged currents as in Equations (2.24).
However, there is an important difference with respect to the mixing of Dirac neutrinos: the physical CP-violating phases in the Majorana mixing matrix are three instead of one. This is due to the fact that the Majorana mass term in (2.39) is not invariant under the global $U(1)$ gauge transformations

$$\nu_{kL} \longrightarrow e^{i\varphi}\,\nu_{kL} \qquad k = 1,2,3\,.$$

Since that, the left-handed massive neutrino fields cannot be rephased. Therefore, the unitary 3×3 mixing matrix of Majorana neutrinos depends on three mixing angles and three physical phases. This mixing matrix can be written as a product of a unitary matrix, similar to the mixing matrix in the Dirac case (2.27), with three mixing angles and one physical phase; and a diagonal unitary matrix D_M, containing the Majorana phases λ_2 and λ_3, that can be written as

$$D_M = \mathrm{diag}\begin{pmatrix} 1 & e^{i\lambda_2} & e^{i\lambda_3} \end{pmatrix}. \tag{2.44}$$

Explicitly, the Majorana mixing matrix can be written as:

$$U = \begin{pmatrix} c_{12}c_{13} & s_{12}c_{13} & s_{13}e^{-i\delta_{13}} \\ -s_{12}c_{23} - c_{12}s_{23}s_{13}e^{i\delta_{13}} & c_{12}c_{23} - s_{12}s_{23}s_{13}e^{i\delta_{13}} & s_{23}c_{13} \\ s_{12}s_{23} - c_{12}c_{23}s_{13}e^{i\delta_{13}} & -c_{12}s_{23} - s_{12}c_{23}s_{13}e^{i\delta_{13}} & c_{23}c_{13} \end{pmatrix} \begin{pmatrix} 1 & 0 & 0 \\ 0 & e^{i\lambda_2} & 0 \\ 0 & 0 & e^{i\lambda_3} \end{pmatrix}. \tag{2.45}$$

The Dirac and Majorana descriptions of neutrino have different phenomenological consequences only if the neutrino is massive. In the massless Dirac theory, the independent left-handed and right-handed chiral components of the neutrino field obey the decoupled Weyl equations (B.5). In the massless Majorana theory, the same Weyl equations (B.5) hold, with the different that left-handed and right-handed chiral fields are related by Equations (B.11). However, only the left-handed chiral component of the neutrino field interacts. If the neutrino is massless, since the left-handed chiral component of the neutrino field obeys the Weyl Equation (B.5a) in both the Dirac and Majorana descriptions, the two theories are physically equivalent.
It is clear that, in practice, it is possible to distinguish a Dirac from a Majorana neutrino only by measuring some effect due to the neutrino mass. The most promising way to find if neutrinos are Majorana particles is the search for neutrinoless double beta decay, described in detail in Chapter 6.

2.2.3 Lepton number in Majorana case

If massive neutrinos are Majorana particles, the total lepton number L is not conserved. In fact, the Majorana mass term in Equation (2.30) is not invariant under the global $U(1)$ gauge transformation of Equation (2.28a), involving the left chiral field. This transformation is incompatible with the definition of the Majorana field (B.14) because, if

$$\nu \longrightarrow e^{i\varphi}\nu\,;$$

then

$$\nu^c \longrightarrow e^{-i\varphi}\nu^c\,.$$

Since in the Majorana case neutrinos and antineutrinos are the same object, it is clear that there cannot be a conserved lepton number. Interactions involving Majorana neutrinos violate lepton number conservation by $\Delta L = \pm 2$.

Chapter 3

The XENON Dark Matter Project

> The strongest of all warriors are these two: Time and Patience
>
> Lev Tolstoj

Among the various experimental strategies for the direct detection of Dark Matter particles, detectors using liquid xenon (LXe) have demonstrated the highest sensitivity. Among these, the XENON Dark Matter Project, hosted at LNGS under 3600 meters-water-equivalent mountain rock, has a leading role since it has developed the LXe-based dual-phase Time Projection Chamber (TPC) technology. The advantages coming from this kind of detector are a good energy resolution due to the detection of a double signal of charge and light and its simple scalability. This technique is the same used by the most sensitive experiments for the direct search of Dark Matter like XENON1T [18] and its smaller predecessors XENON10 [19] and XENON100 [20], LUX [21], PandaX [22] and the new XENONnT [23], fast upgrade of XENON1T.
The first phase of XENON Dark Matter Project was XENON10, installed in 2005 and operational until 2007, consisting of a total LXe mass of 15 kg with 5.4 kg used as fiducial mass. Its aim was to test the possibility to realize a dual-phase TPC (LXe/GXe) on the kg scale to detect directly Dark Matter interactions. The good results obtained in 2007 [24] pushed towards the realization of a new larger detector based on its same detection principle: XENON100. The LXe amount was increased to 161 kg, with 62 kg used as active volume in the TPC and the remaining as an outer active veto. The fiducial volume was chosen as 34 kg or 48 kg, depending on the background conditions. In 2012 XENON100 experiment set the best upper limits both on the spin-independent [25] and spin-dependent [26] coupling of WIMPs to nucleons.
To significantly improve upon the XENON100 experimental sensitivities, the

XENON Dark Matte Project laid the foundations for the next generation of multi-ton scale double-phase TPC with XENON1T, a 3.2 t LXe detector with 2 t of active mass in the TPC.
After setting the current most stringent constraint on the WIMP-nucleon spin-independent cross section, with a minimum of $4.1 \times 10^{-47}\,cm^2$ for WIMP of mass $m_\chi = 30\,GeV\,c^{-2}$ at 90% CL [27], XENON1T was replaced by its upgrade XENONnT, consisting of about 8 t of total LXe mass with 5.9 t of active mass, with the aim of improving the sensitivity of XENON1T of about an order of magnitude [28].

3.1 Liquid xenon as Dark Matter target

In experiments searching for rare events expected from physics beyond the Standard Model, liquid xenon remains the preferred medium for many reasons. An important feature of LXe is the production of both free electrons and scintillation photons when energy is deposited by an incident particle. Another property of LXe, is represented by its self-shielding power against external background sources thanks to its high atomic number $Z = 54$ and density $\rho = 2.96\,g cm^{-3}$. Its relatively large triple point $T = 161\,K$ it is not extremely demanding from the cryogenic point of view and, moreover, its large atomic number $A = 131$ increases the expected WIMP interaction rate, since the WIMP-nucleus cross section scales with A^2. xenon has nine stable isotopes, while the unstable ones are very short-lived. Hence, it is a rather pure material, which is a mandatory requirement for a search of very rare events like WIMP scatterings. There are two isotopes with non zero spin: ^{129}Xe with spin $\frac{1}{2}$ and ^{131}Xe with spin $\frac{3}{2}$, with isotopic abundance of 26.4% and 21.2% respectively. This allows to study also the dependence of the WIMP-nucleus cross section on the spin, thus providing more informations about the Dark Matter nature.

3.1.1 Ionization yield

The energy deposited by radiation in noble liquids is shared among the electron-ion pairs production, atoms excitation and the production of sub-excitation electrons with kinetic energy lower than the xenon excitation energy degrading into heat. The deposited energy E_0 into ionization, excitation, and sub-excitation electrons can be expressed by an energy balance equation proposed by Platzman:

$$E_0 = N_i E_i + N_{ex} E_{ex} + N_i \varepsilon, \tag{3.1}$$

where N_i and N_{ex} are, respectively, the number of electron-ion pairs and excited atoms produced, E_i and E_{ex} are the average expenditures of energy to ionize or

excite a Xe atom while ε is the mean kinetic energy of sub-excitation electrons. For LXe the average energy lost in excitation process is comparatively small ($\sim 5\%$) [29], while the energy transferred to sub-excitation electrons is larger than 30% of the ionization potential. It is possible to define the W value as the average energy required to produce one electron-ion pair:

$$W = \frac{E_0}{N_i} = E_i + E_{ex}\left(\frac{N_{ex}}{N_i}\right) + \varepsilon. \tag{3.2}$$

The ionization yield, also known as charge yield, is defined as the number of electron-ion pairs produced per unit absorbed energy and it is inversely proportional to the W value. Among the liquid noble gases, LXe has the smallest W value, about $15.6\,eV$ [30], therefore the largest ionization yield of about 6×10^7 electron-ion pairs per keV. As we consider the fraction of collected charges, the electron-ion recombination process plays a crucial role. In fact, a fraction r of the total initial electron-ion pairs recombines forming additional excitons, hence the number of detected electrons is given by

$$N_e = (1 - r)N_{ex}, \tag{3.3}$$

while the number of photons due to the de-excitation of the initial and recombined excitons is

$$N_\gamma = \left(\frac{N_{ex}}{N_i} + r\right)N_i. \tag{3.4}$$

Since different particles ionizes the medium in different ways, the recombination process intensity depends on the particle type: highly ionizing particles have tracks with a high density of free charge, leading to a higher recombination rate compared to minimum ionizing particles.

3.1.2 Scintillation yield

In addition to the ionization of the medium, xenon emits scintillation light of $177.6\,nm$ in the region of vacuum ultraviolet (VUV) light. The xenon scintillation is attributed to the decay of excited dimers (excimers) to the ground state. They can be produced by two different processes involving excited atoms (Xe^*):

$$\begin{aligned} Xe^* + Xe + Xe &\rightarrow Xe_2^* + Xe, \\ Xe_2^* &\rightarrow 2Xe + h\nu, \end{aligned} \tag{3.5}$$

or ionized ions (Xe^+) [31]:

$$\begin{aligned} Xe^+ + Xe &\rightarrow Xe_2^+, \\ Xe_2^+ + e^- &\rightarrow Xe + Xe^{**}, \\ Xe^{**} &\rightarrow Xe^* + \text{heat}, \\ Xe^* + Xe + Xe &\rightarrow Xe_2^* + Xe, \\ Xe_2^* &\rightarrow 2Xe + h\nu. \end{aligned} \tag{3.6}$$

Due to the different configuration of the energy levels of dimers and atoms, the photons emitted by dimers are not re-absorbed by the atoms making LXe transparent to its own scintillation light. The scintillation light in LXe has two decay components with two different decay times: the singlet and the triplet states of the excited dimers Xe_2^*. The fast scintillation component is due to the direct de-excitation of the singlet states while the slow one to the triplet ones. Their decay times can vary under intense electric fields. In absence of an external electric fields, the scintillation signal for α particles and fission fragments is characterized by a fast component $\tau_f \simeq 4\,ns$ and a slow one $\tau_s \simeq 20\,ns$ [32]. For relativistic electrons, the low deposited energy density leads to a slow electron-ion recombination, therefore the signal is dominated by a single component with a decay time of $45\,ns$. As an electric field is applied to the LXe, the double component structure is observed also for electrons, with $\tau_f \simeq 2\,ns$ and $\tau_s \simeq 27\,ns$ [32]. The difference between the scintillation signal decay for different types of incident particles can be used to discriminate these particles: this technique is called pulse-shape discrimination (PSD) and it is widely used with organic scintillator [33]. The small time separation of the decay components makes difficult to use this technique with LXe-based detector, but for LAr this is an effective technique as the singlet and triplet components have very different lifetime, about $5\,ns$ and $1590\,ns$. For this reason LAr based TPCs have the advantage to be able to operate in a single phase mode, indeed they can discriminate electronic recoils (ERs) and nuclear recoils (NRs) events using PSD techniques. The scintillation yield, known as light yield, is defined as the mean number of emitted photons per unit deposited energy. LXe has the highest light yield compared to all noble liquids since emits about 5×10^7 photons per keV deposited. Assuming the absence of quenching processes, the maximum light yield is reached when all the electron-ion pairs recombine to produce excimers, when $r = 1$ in Equation (3.4), possible only for a null external electric field. In this best-scenario case, the average energy required to produce a single photon is

$$W_{ph} = \frac{W}{1 + N_{ex}/N_i}, \tag{3.7}$$

as obtained by Equations (3.1) and (3.2). Since most of the scintillation light comes from the recombination process described in Equation (3.6), the scintil-

lation yield depends on the linear energy transfer (LET), that is the density of electron-ion pairs produced along the track of a particle, because the recombination probability between electrons and ions increases with the density of electron-ion pairs. In liquid and gaseous xenon (GXe), for high electric field below the avalanche threshold, a scintillation process called proportional scintillation, or electro-luminescence, occurs as observed for the first time by the Saclay group [34]. Electrons produced by ionization acquire enough energy to excite atoms in collisions emitting light through a process similar to the normal scintillation [35]

$$\begin{aligned} e^- + Xe &\rightarrow e^- + Xe^*, \\ Xe^* + 2Xe &\rightarrow Xe_2^* + Xe, \\ Xe_2^* &\rightarrow 2Xe + h\nu. \end{aligned} \tag{3.8}$$

The proportional scintillation spectrum is similar to that of scintillation, therefore this signal can be efficiently detected by the PMTs used for scintillation light.

3.1.3 Anti-correlation of light and charge signals

In double-phase TPCs, both signals coming from scintillation and ionization can be observed simultaneously. Ionizing radiations deposit their energy in the medium following the Platzman balance equation (3.1), therefore the number of excited atoms and electron-ion pairs is proportional to the deposited energy and to its LET. Excluding impurities effects, the sum of the scintillation and ionization signal divided by $N_{ex} + N_i$ gives a completely flat LET dependence: this holds if excited atoms and electron-ion pairs are exclusively converted into light or free charge signals. This leads to a perfect anti-correlation between the charge yield and light yield. For relativistic electrons this correlation does not perfectly hold: for low LET the light yield decreases because of escape electrons, i.e. those electrons not recombining for an extent period of time in the absence of electric field. These electrons can be collected as charge signal for high electric fields. Since ionization and scintillation signals are anti-correlated, also their fluctuations are: this means that for a under-fluctuation of one signal, the other over-fluctuates. Indeed, by normalizing the detected signals to the numbers of photons or electrons emitted by LXe, their sum is constant and independent on the electric field applied, as Figure (3.1) shows. As a result, the fluctuation of the sum signal is smaller than that of the individual signals. Therefore, a measurement of both the charge and light signals improves the energy resolution of the LXe-based detector.

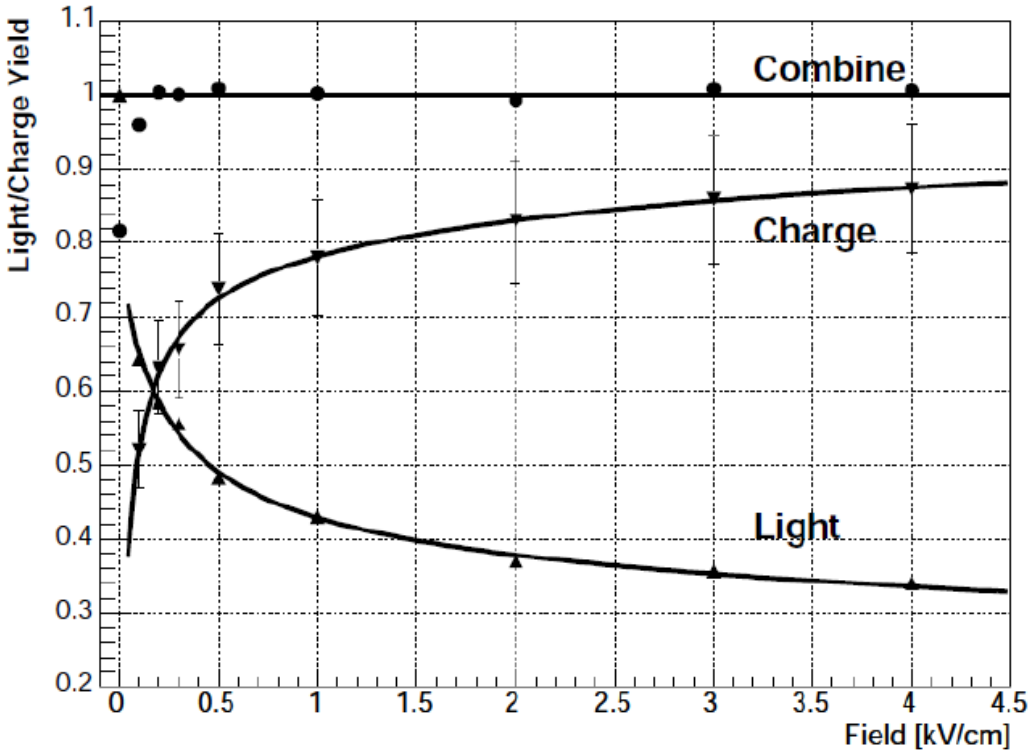

Figure 3.1: Measurements of light and charge yield in LXe as a function of the applied electric field for mono-energetic $662\,keV$ γ-rays from ^{137}Cs [36]. The charge yield increases with higher fields, as the recombination of freed electrons becomes less probable and more electrons take part to the S2 signal. This also implies that the S1 signal loses the contribution from the recombination process.

3.2 Detection principle of a double-phase TPC

The core of the XENON Project is the double-phase xenon TPC detector, exploiting both the light and the charge signals produced by the interaction of particles with the target LXe. The top and the bottom of the TPC are defined, respectively, by the cathode electrode (negatively charged) and the gate mesh (grounded). This region encloses the LXe sensitive volume. Above the gate electrode there is the anode, with the LXe/GXe interface between them: a high electric field $E_{extraction}$, of $\mathcal{O}(10\,kV\,cm^{-1})$, is kept between the two in order to extract the electrons from the LXe. A top array of photomultiplier tubes (PMTs) in the GXe and a bottom one below the cathode in the LXe are used to detect the light signals, whose collection is maximized by coating the TPC internal walls using PTFE (polytetrafluoroethylene) panels. The PMTs have to be sensitive to the xenon scintillation VUV light at $\lambda \simeq 178\,nm$.

The energy deposited by an incident particle in the instrumented volume produces two measurable signals from which the energy deposition can be reconstructed. The working principle of a double-phase LXeTPC is shown in Figure (3.2): when a particle interacts with the LXe target, the deposited energy is converted both in prompt scintillation light, named S1, and in electron-ion pairs produced by ionization. The primary signal S1 is immediately detected by the

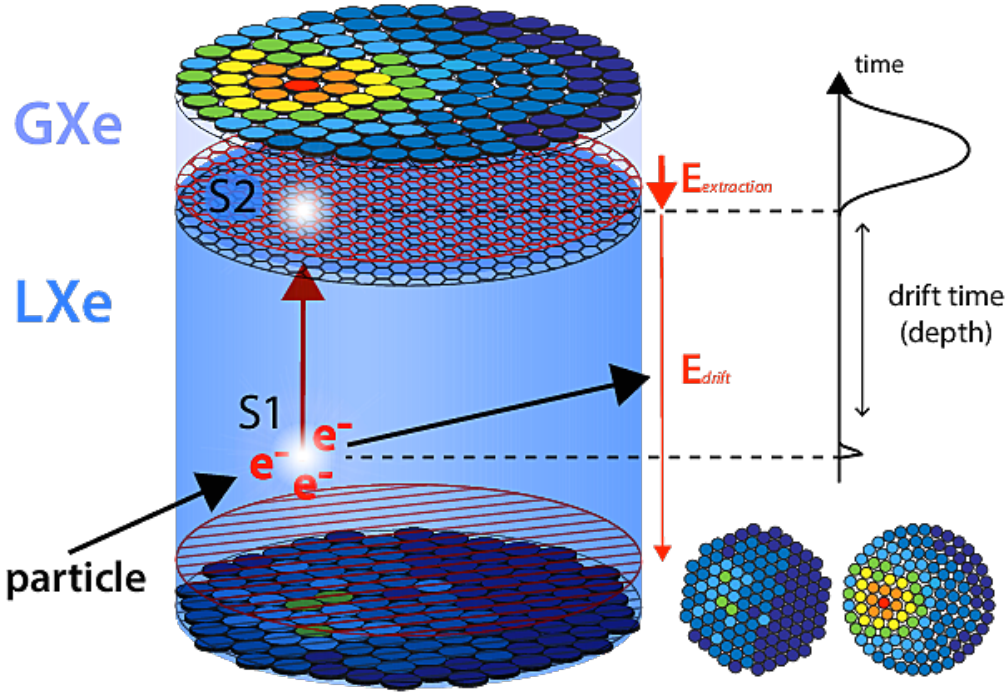

Figure 3.2: Schematic view of the working principle of a double-phase TPC used in the XENON Project. The prompt scintillation signal S1 is measured by both PMT arrays. Ionization electrons are drifted from the interaction vertex towards the LXe/GXe interface under the action of an uniform electric field E_{drift}. The S2 signal is formed via proportional scintillation triggered by electrons extracted in the gaseous region by means of another intense electric field $E_{extraction}$ established between the gate (electrode just below the liquid-gas interface, in black) and the anode (electrode just above the liquid-gas interface, in red). The localized pattern of the S2 signal in the top PMT array is used to reconstruct the (x, y) interaction position, while the delay time between S1 and S2 informs about the z position of the interaction vertex. The energy of the event is reconstructed from the combination of both S1 and S2 signals.

PMT arrays. The electrons which do not undergo recombination, are drifted by an electric field E_{drift} towards the anode in the GXe gap. As they reach the in-

terface above the grounded mesh, they are extracted from the LXe into the GXe by the high electric field $E_{extraction}$ and they produce a proportional scintillation light signal, named S2. A measurement of both S1 and S2 signals allowed a full 3D reconstruction of the position of the energy deposition in the TPC. From the hit pattern of the S2 signal on the top PMTs, the (x, y) position is determined. The z coordinate is inferred from the time difference between S1 and S2 signals. The knowledge of the interaction point allows the selection of those events located in the inner part of the LXe, usually called fiducial volume. Since the major part of background events are expected to be found at the edge of the TPC, the outermost volume is used as shield to remarkably reduce the background from external sources.
The position reconstruction is important to correct the detected signals for inefficiency and position-dependent effects. A light collection efficiency (LCE) map is applied to S1 signal to take into account detector geometrical efficiencies and PMTs quantum efficiencies. This correction map is obtained from ^{83m}Kr calibration data, correcting for each position in order to have an homogeneous light yield in the entire volume. Similarly, the charge signal S2 needs to be corrected both for its LCE map and for the electron lifetime. Indeed, drifting electrons may be captured by impurities or recombine with ions along their path, following an exponential decrease of the signal with the z position of the event. The electron lifetime τ_e is measured by fitting the exponential decay of an intrinsic ER calibration source S2 signal intensity as a function of the z position. The XENON1T experiment uses both α particles from ^{222}Rn and monoenergetic gammas from ^{83m}Kr to measure the electron lifetime. Applying these corrections to both S1 and S2 signals, the corrected cS1 and cS2 are obtained. Combining the cS1 and cS2, the energy resolution improves since the anti-correlation between the signals reduces the statistical fluctuations. The reconstructed combined energy is a function of both the signals and it is given by

$$E = W\left(\frac{cS1}{g_1} + \frac{cS2_b}{g_2}\right), \tag{3.9}$$

where $W = (13.7 \pm 0.2)\ eV$ is the mean energy needed to produce a quantum (photon or electron) in LXe, while g_1 and g_2 are the S1 and S2 gains, i.e. the number of observed photoelectrons per photon or electron. Instead of using the proportional signal cS2, the fraction of it collected in the bottom array $cS2_b$ is preferred since it is homogeneously distributed over the entire bottom array area, whereas the proportional photons collected on the top are mainly detected by few PMTs.

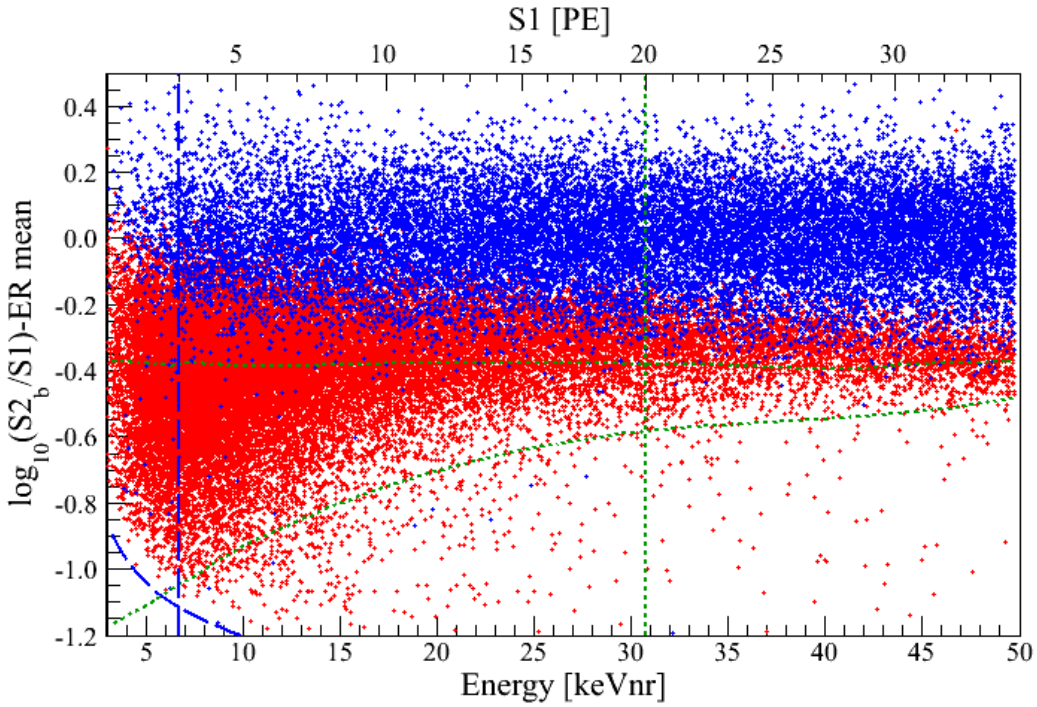

Figure 3.3: Distribution of the flattened discrimination parameter $\log_{10}\left(\frac{S2}{S1}\right)$ as function of the nuclear recoil energy (or S1 signal, in upper x axis) achieved with the XENON100 experiment [20]. The ER band, obtained from calibration data of ^{60}C and ^{232}Th (γ emitters), is shown in blue, while in red is shown the NR band, obtained from calibration of ^{241}AmBe (neutron source). The y axis is the flattened version of the $\frac{S2}{S1}$ distribution, considering $\log_{10}\left(\frac{S2}{S1}\right) - \mathrm{ER}_{\mathrm{mean}}$, where $\mathrm{ER}_{\mathrm{mean}}$ is the mean of the ER band. In this way, one gets a flat ER band centered in zero and removes the energy dependence of this discrimination parameter.

3.2.1 Discriminating electronic and nuclear recoils

The ability to discriminate the interacting particle is fundamental for direct Dark Matter search experiments. Indeed, WIMPs are expected to interact with the medium through elastic scatter off a nucleus, producing NR events, while most of the background consists of ER events, like γ rays and electrons coming from radioactive isotopes, both in the detector materials and intrinsic. Therefore, being able to discriminate between ERs and NRs means reducing the main background. Particles with different LET have different $\frac{S2}{S1}$ ratio and this is exploited for discrimination. Due to its high LET, NR has higher recombination rate with respect to the ER, therefore the ratio between the charge and light signals for

recoiling nuclei is much lower

$$\left(\frac{S2}{S1}\right)_{NR} \ll \left(\frac{S2}{S1}\right)_{ER}. \tag{3.10}$$

The detector response to ER and NR events is characterized through calibration runs, where γ-rays and neutrons sources are used to produce a high statistics respectively for ERs and NRs. An example of the ER and NR bands obtained with calibration runs is shown in Figure (3.3) for XENON100 experiment [20]. The ER events are from ^{60}C and ^{232}Th calibration, while the NR events are from ^{241}AmBe calibration [37]. Given the overlap between the ER and NR bands, in XENON100 a 99.5% ER discrimination corresponded to a 50% acceptance of NR events, while a 99.75% ER discrimination gave an acceptance of 40%. A good discrimination power allows to reduce the ER background impact in the WIMP search. The data analysis for XENON1T does not apply a hard cut to reject ER events, but exploits the full information of the ER and NR distributions in the $(S1, S2)$ space through a profile likelihood treatment [38].

3.3 Past XENON experiments

The XENON Project aims at the detection of WIMPs interaction with nuclei by using the technology of the double-phase xenon TPC. The advantages of this detector are the ability to detect both light and charge signals, improving the energy resolution and discriminating ER and NR events, and its simple scalability. The scalable technology has allowed the evolution of the XENON Project from a kg scale TPCs for XENON10 and XENON100 experiments up to the tonne-scale experiments, XENON1T and the current XENONnT, all of them hosted at LNGS. In the following, the past experiments of the Project and their main results are briefly discussed.

3.3.1 XENON10

The XENON10 detector was the first prototype of the XENON Dark Matter search program, containing a total of 25 kg of pure LXe and aiming at demonstrating the achievable energy threshold and background rejection power [39]. It has taken data from October 2006 to February 2007. The TPC active volume is defined by a PTFE cylinder with an inner diameter of 20 cm and a height of 15 cm, for a total amount of about 14 kg of LXe, and an electric drift field is applied to it. The detector is protected from external background by a cubic steel-framed structure, consisting of 20 cm high-density polyethylene (HDPE) inside 20 cm of low-radioactivity lead. The HDPE is used to reduce the neutron background by

a factor 90, which is mainly due to radiogenic and cosmogenic neutron production in the surrounding rock or lead. It was installed at the LNGS and started the commissioning in April 2006, then from October 2006 to February 2007 a total of 58.4 live days of data were acquired using a fiducial volume of 5.4 kg. The analysis of these data improved upper limits on both spin-independent and spin-dependent cross sections for WIMP scattering off nuclei. An exclusion limit at 90% CL to spin-independent cross section of $4.5 \times 10^{-44}\,cm^2$ was reached for $m_\chi = 30\,GeV\,c^{-2}$ [24]. Concerning the spin-dependent cross section, an upper limit of $5 \times 10^{-39}\,cm^2$ was set for $m_\chi = 30\,GeV\,c^{-2}$ [40].

3.3.2 XENON100

The XENON100 experiment started in 2008 and ended its data acquisition in the middle of 2016. The TPC is an almost cylindrical structure with a height of 30.5 cm and a diameter of 20.6 cm and the drift field is about $530\,V\,cm^{-1}$ [20]. It contains an active LXe mass of 62 kg enclosed by 24 panels made of PTFE, chosen for its properties both as insulator and good reflector for the VUV scintillation light. The active volume is read by a top and bottom PMTs arrays, respectively made of 98 and 80 rectangular PMTs selected for their low radioactivity and high quantum efficiency for the LXe scintillation light wavelength. The target is surrounded by an optically separated LXe veto, acting as an active shield of about 99 kg and it is instrumented with 64 PMTs, of the same type used for the TPC readout. An additional passive shield is used to reduce the background coming from the radioactivity of the environment. After setting the best limits on spin-independent WIMP-nucleon interaction cross section in 2012 using a total exposure time of 225 days with a fiducial mass of 34 kg [25], in 2016 XENON100 improved them combining three different science runs for a total exposure time of 477 live days and a fiducial mass of 48 kg [41]. A profile likelihood analysis was performed to set the upper limit on spin-independent elastic scattering WIMP-nucleon cross section for WIMP masses above $8\,GeV\,c^{-2}$. It set a 90% CL minimum at $1.1 \times 10^{-45}\,cm^2$ for $m_\chi = 50\,GeV\,c^{-2}$. Using the same approach, an upper limit on the spin-dependent WIMP-neutron and WIMP-proton elastic scattering cross sections were set with a minimum of $2.0 \times 10^{-40}\,cm^2$ and $52 \times 10^{-40}\,cm^2$ respectively for $m_\chi = 50\,GeV\,c^{-2}$, at 90% CL.

3.3.3 XENON1T

The XENON1T experiment, hosted underground in the Hall B of the LNGS, was commissioned in 2016 and its first results were published in May 2017. With an active mass of 2 t of LXe, it is the first tonne-scale double-phase TPC dedicated to the direct search of Dark Matter, with a sensitivity reached of $1.6 \times 10^{-47}\,cm^2$

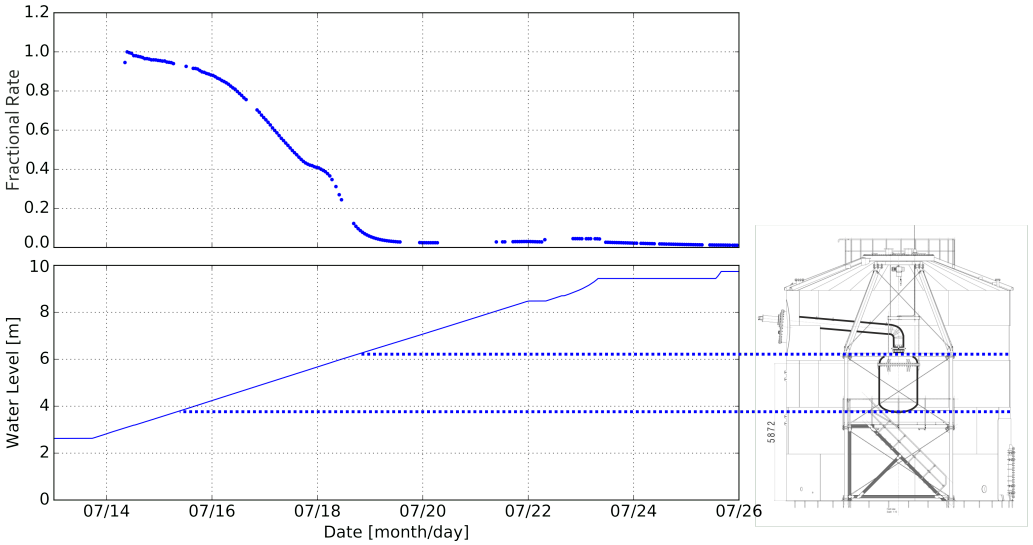

Figure 3.4: Decrease of the event rate as the water tank is filled with water.

for $m_\chi = 50\,GeV\,c^{-2}$ [18]. The total amount of 3.2 t of LXe is contained in the dual-phase TPC, installed inside a double-walled vacuum Cryostat made of 5 mm thick low-radioactivity stainless steel. The TPC is a 97 cm high cylinder with a diameter of 96 cm, enclosed in 24 interlocking and light-tight PTFE panels, whose surfaces were treated with diamond tools in order to optimize the reflectivity for vacuum ultraviolet light. The operating temperature of $T_0 = -96\,°C$ is reached following a remote cooling concept for the cryogenic system, which is installed far from the Cryostat. In this way it is possible to reduce the material close to the TPC, to minimize the mechanical vibrations and to do maintenance while the detector is running. A total of 248 PMTs of 76.2 mm diameter are used to record the signals from the TPC. They feature an average room temperature quantum efficiency of 34.5% at 178 nm [42], a high photoelectrons collection efficiency of 90% and are designed to operate in gaseous and liquid xenon at cryogenic temperature [43, 44]. The PMTs with the highest quantum efficiency were installed at the center of the bottom array to maximize the light collection efficiency. The Cryostat is surrounded by a muon Veto Čerenkov detector, consisting of a 10.2 m high tank with a diameter of 9.6 m, filled with deionized water and instrumented with 84 PMTs with a diameter of 20.3 cm (Hamamatsu R5912ASSY) [23]. It identifies muons and allows to reduce the NR background due to neutrons produced by muon spallation in the cavern rock by identifying the accompainying particle shower in the water tank. The cosmic muon flux is $(3.31 \pm 0.03) \cdot 10^{-8}\ cm^{-2}\,s^{-1}$ with an average energy of about 270 GeV in Hall B of LNGS, shielded by the 3600 meters-water-equivalent of mountain rock [45]. In order to maximize the light collection efficiency, the inner surface of the water

tank is covered by a reflective foil acting as a wavelength shifter to better overlap the Čerenkov light spectrum with the high quantum efficiency region of the PMTs, about 30% in $[300, 600]$ nm. The tagging efficiency for muons crossing the water tank is 99.5%, while it is 43% for muon-induced showers, sufficient to make the muon-induced neutron background negligible for both XENON1T and XENONnT. The water additionally provides effective shielding against environmental background radiation, as it is shown by the event rate decrease during the water tank filling in Figure (3.4).

Results from XENON1T

After a period of commissioning, XENON1T started its first science run, named Science Run 0 (SR0), on November 2016. It lasted until January 2017, when an earthquake temporarily interrupted the detector operations. It started to work again on February 2017 to February 2018 (SR1). XENON1T reached a low energy ER background of $\left[82^{+5}_{-3}(\text{syst}) \pm 3(\text{stat})\right]$ events $[\,t \cdot yr \cdot keV]^{-1}$ [46], the lowest ever achieved in a Dark Matter search detector. Calibration runs took place before and during the science runs, using ^{83m}Kr for spatial corrections, ^{220}Rn to define the ER band for low energies and ^{241}AmBe for the NR band at low energy. For the SR0 + SR1 analysis [46] a cylindrical fiducial volume of (1.30 ± 0.01) t of LXe mass is selected, based on the reconstructed spatial distribution of ER background events. The regions of interest are defined as $[1.4, 10.6]$ keV for electronic recoils and $[4.9, 40.9]$ keV for nuclear ones. The main background for the WIMP search comes from the intrinsic ER background coming from β decays of ^{85}Kr and ^{214}Pb. Other background sources are radiogenic neutrons, coherent scattering of neutrinos off xenon nuclei (CNNS), accidental coincidences of uncorrelated S1 and S2 signals, wall leakage events due to inward-reconstructed events happening on the walls [38]. As no significant deviation from the expected background were observed, an exclusion limit was set on SI WIMP-nucleon cross section at 90% CL, which improves upon the XENON100 results by one order of magnitude. The minimum at 4.1×10^{-47} cm^2 for $m_\chi = 30\,\text{GeV}\,c^{-2}$ is currently the lowest cross section ever excluded [46]. The upper limit for a wide WIMP mass range at 90% CL is shown in Figure (3.5), in comparison with the other Dark Matter search experiments based on double-phase XeTPCs. XENON1T provided results also on spin-dependent elastic WIMP-neutron cross section, reaching a minimum of 6.3×10^{-42} cm^2 at 90% CL for $m_\chi = 30\,\text{GeV}\,c^{-2}$ [47] and first results on the scalar coupling of WIMP-pion, leading to an upper limit cross section of 6.4×10^{-46} cm^2 at 90% CL for $m_\chi = 30\,\text{GeV}\,c^{-2}$ [48]. Another important result of XENON1T is the direct observation, in April 2019, of the two-neutrino double electron capture (2νCECE) in ^{124}Xe, consisting in a simultaneously conversion of two protons into neutrons

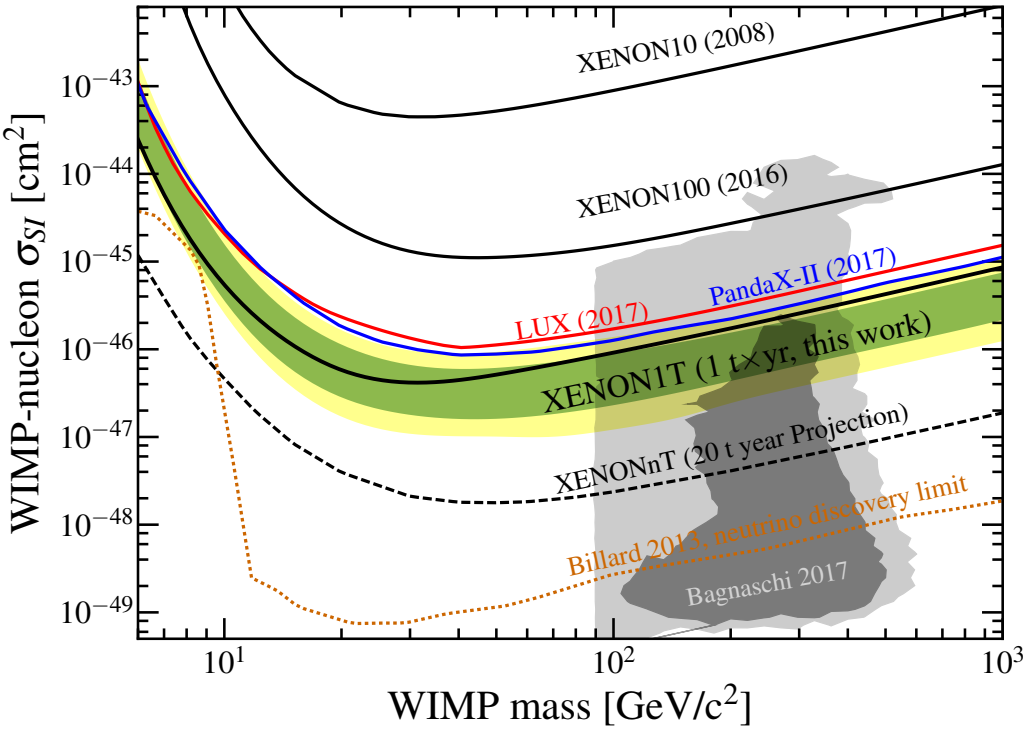

Figure 3.5: The 90% CL upper limit on SI WIMP-nucleon cross section from the XENON1T 1 t yr search with the 1σ (green) and 2σ (yellow) sensitivity bands. Previous world best results from LUX (red line) [21] and PandaX-II (blue line) [22] experiments are shown for comparison. Results from past XENON10 [19] and XENON100 [20] are drawn as black solid lines, while the predicted sensitivities for an exposure of 20 t yr for XENONnT is shown as dashed black lines. The neutrino discovery limit [49] (orange line) is also shown for reference, as well as a supersymmetric DM model [50] constrained by accelerator experiments, astrophysical observations and direct detection searches.

by the absorption of two electrons from one of the atomic shells, emitting two electron neutrinos:

$$^{124}\mathrm{Xe} \longrightarrow {}^{124}\mathrm{Te} + 2\nu_e\,.$$

The extremely long half-life of this process, about 10^{12} times the age of the Universe (1.83×10^9 yr) makes it the rarest decay ever observed [51]. This observation demonstrates that the low background and large target mass of xenon-based Dark Matter detectors make them well suited to measuring other rare processes as well, and it highlights the broad physics reach for even larger next generation experiments.

3.4 The XENONnT upgrade

XENON1T has been built with the capability to rapidly increase its sensitive target while further reducing the background from intrinsic and external sources. The current step of the XENON Project is named XENONnT, now in assembly phase at LNGS. The XENON1T detector support structure was built to stand also a heavier TPC in the same Cryostat, replacing just the inner vessel. Similarly, the XENON1T cryogenic and purification systems as well as the recovery system were designed to handle a target mass scale-up to about 8 t. Leveraging on these existing systems and overall infrastructure, thoroughly tested during XENON1T commissioning and operation, the new XENONnT inner detector is placed in the same water shield and serviced by the same systems and infrastructure. The increased Xe target mass, together with a further reduction of the intrinsic background, mainly achieved by careful material selection, active Rn-removal, improved detector and veto design and more efficient self-shielding, will allow an order of magnitude improvement in sensitivity. The largest TPC fitting in the XENON1T outer vessel can contain up to 5.9 t of LXe, for a total amount of almost 8 t of xenon in the new inner vessel leading to increase the fiducial mass by a factor 4 with respect to XENON1T. This TPC has a height of about 1.6 m and a diameter of 1.34 m and its active volume is observed by a bottom array of 241 PMTs and a top one of 253 PMTs. Among the main changes in the XENON1T subsystems, the GXe purification system will use new recirculation pumps to fasten the process and a LXe recirculation and purification systems will be used in parallel. It exploits the high density of liquid xenon to purify faster the detection medium from electronegative impurities. Moreover, a new dedicated cryogenic distillation column will operate continuously for an on-line removal of intrinsic ^{222}Rn in order to reduce its background of a factor 10, namely to $10^{-6}\,\mathrm{Bq\,kg^{-1}}$. A new Veto detector to tag neutrons which first scatter inside the TPC, leaving a single scatter nuclear recoil signal, has been added. It will be realized doping with Gd-sulphate the 700 t of water in the outer shield. Neutrons, once exiting the Cryostat, will be effectively captured on Gd and produce a gamma cascade of about 8 MeV in total. The Čherenkov light generated after neutron capture is detected with 120 additional PMTs, same model of the ones used in the muon Veto, but with higher quantum efficiency and reduced radioactivity, installed about 1 m far away from the Cryostat and inside a newly designed ePTFE reflector to improve light collection efficiency. From Monte Carlo simulations, described in Section 5.3, the expected efficiency for neutron tagging is about 87% requiring the coincidence of 10 nVeto PMTs: this reduces NR background from radiogenic neutrons by a factor ~ 5, keeping the total neutron background in the 4 t fiducial volume to about 1 event in the total exposure of 20 t yr. The sketch of the neutron Veto surrounding the outer

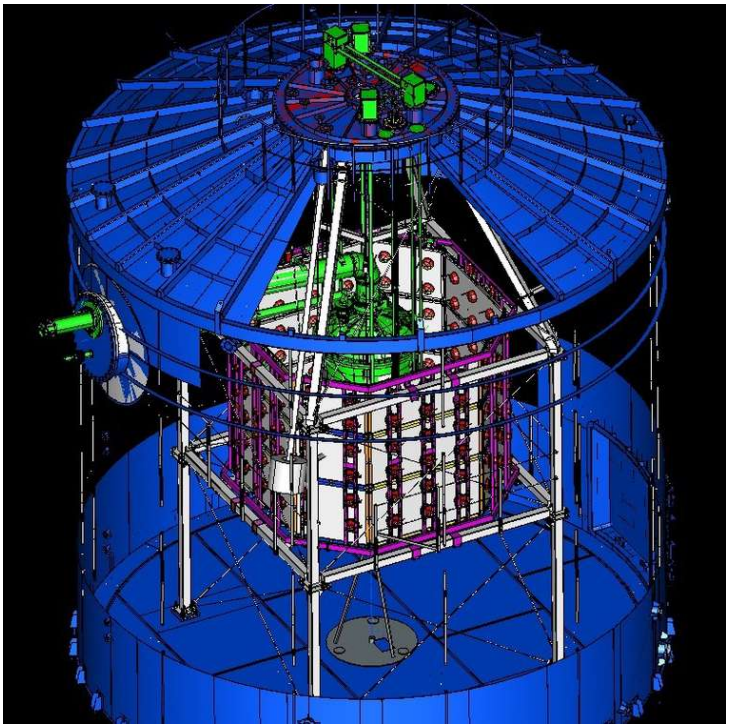

Figure 3.6: Sketch of the neutron Veto surrounded by the octagonal support structure instrumented with the 120 PMTs. The water tank, used as Čerenkov muon Veto, is shown in blue, instrumented with 84 PMTs.

Cryostat is shown in Figure (3.6). The XENONnT experiment will be sensitive to SI WIMP-nucleon cross section down $10^{-48}\,cm^2$, as shown in Figure (3.5): one order of magnitude above the so-called *neutrino floor* for WIMP masses above $100\,GeV\,c^{-2}$, where the irreducible background from coherent neutrino-nucleus scattering becomes an important limiting factor.

The following Chapters present the results obtained by XENONnT from neutrinos studies. In fact, this experiment can be used not only as Dark Matter detector, but also to detect Supernova neutrinos through two different interaction channels: through coherent elastic neutrino-nucleus scattering (CEνNS) on Xe nuclei in the TPC [52] and through Inverse Beta Decay interactions with protons in water, described in Chapter 5. About the first one, since (CEνNS) is insensitive to the neutrino flavor, the signal produced is unaffected by uncertainties from neutrino oscillation physics. For this, dual-phase Xe detectors will provide complementary information on the SN neutrino signals that are not obtainable with existing or planned neutrino telescopes, allowing to measure the average energy of all flavors neutrinos, to constrain the total explosion energy

and to reconstruct the Supernova neutrino light curve. The second one, instead, involves the electron antineutrinos only, allowing to measure the XENONnT detection efficiency for this type of interaction. Moreover dual-phase Xe detectors can be used also to research rare events, as the neutrinoless double-beta decay described in Chapter 6.

Chapter 4

Supernova neutrino emission and oscillations

Id facit exiguum clinamen principiorum
nec regione loci certa nec tempore certo.

Lucrezio
De Rerum Natura, Liber II

4.1 Dynamic of a Supernova explosion

Core collapse Supernovae are among the most energetic events that occur in the Universe, originating from the death of stars with mass $M > 8\,M_\odot$. These are also among the most powerful sources of neutrinos: during a Supernova explosion, the 99% of emitted energy $U \simeq 10^{53}\,erg$ is released by neutrinos and antineutrinos of all flavors with mean energies of tens of MeV. This particles play the role of astrophysical messengers, travelling unimpeded through the Universe. They also play an important role in the final state of a massive star: they govern the infall dynamics of the stellar core, trigger the explosion and drive the cooling and deleptonization of the new formed compact relic [53]. The SN iron core is surrounded by shells of lighter elements. Once the Chandrasekhar mass limit $M_{ch} = 1.4\,M_\odot$ is reached, the core collapse begins. It is curbed by the repulsive nuclear force in correspondence of the density value $\rho_{nuclear} = 2.8 \times 10^{14}\,g\,cm^{-3}$, when the nuclear matter becomes almost incompressible. The pressure is now sufficient to stop the collapse, causing the rebound of the inner core. Shock waves are generated and reflected from the inner to the outer layers. This mechanism can reverse the collapse of the star, generating the so called Supernova explosion.

During the propagation, the shock wave loses energy through iron nuclei dissociation. Free protons permits a fast neutronization of the stellar nucleus via electron capture, causing an emission of electronic neutrinos:

$$e^- + p \longrightarrow n + \nu_e \,. \tag{4.1}$$

The star becomes a proto-neutron star. The ν_e produced can escape until the nuclear density becomes so high to trap them. From this moment on, the ν_e produced are swept inward with the infalling matter. Within few milliseconds after trapping, the center reaches nuclear matter density. The repulsive contribution to the nuclear force between the nucleons provides resistance against further compression and the collapse of the inner core comes to an abrupt halt. The bounce shock begins to travel outwards against the ongoing collapse of the overlying iron core material. The ν_e stay trapped in the dense post shock matter until the shock reaches sufficiently low densities for the ν_e to diffuse faster than the shock propagates. Shortly after shock breakout, the loss of ν_e leads to a considerable drop of the electron lepton number in the shock-heated matter. This allows for the appearance of large concentration of positrons. When the positrons and neutrons become more abundant, e^+ capture on n also permits the emission of $\overline{\nu}_e$:

$$e^+ + n \longrightarrow p + \overline{\nu}_e \,. \tag{4.2}$$

The kinetic energy of the infalling matter is dissipated into thermal energy, leading to an abrupt deceleration of the flow and a corresponding increase of the density, temperature, pressure, and entropy behind the shock. Because of the temperature increase, heavy nuclei in the medium are completely disintegrated to free nucleons when the shock wave passes through the matter. This consumes appreciable amounts of energy, roughly $8.8\,MeV$ per nucleon. This energy drain and the additional energy losses by the ν_e burst reduce the post-shock pressure and weaken the expansion of the bounce shock. It finally stagnates at a radius between 100 and 200 km. The bounce shock mechanism therefore fails to initiate the explosion of the dying star as Supernova. The most likely mechanism to revive the stalled shock front and to initiate its expansion against the pressure of the collapsing surrounding stellar core matter is energy transfer by the intense neutrino flux radiated from the nascent neutron star. The most important reactions for depositing energy behind the shock are ν_e and $\overline{\nu}_e$ captures on free nucleons:

$$\nu_e + n \longrightarrow p + e^- \,, \tag{4.3a}$$

$$\overline{\nu}_e + p \longrightarrow n + e^+ \,. \tag{4.3b}$$

Before the Supernova shock front accelerates again outward and the Supernova blast is launched, stellar matter collapsing through the stagnant shock feeds a massive accretion flow onto the nascent neutron star. The hot accretion mantle

around the high density core of the neutron star radiates high fluxes mainly of ν_e and $\overline{\nu}_e$, which carry away the gravitational binding energy that is released in the gravitational collapse. This accretion luminosity adds to the core luminosity of all species of neutrinos and antineutrinos that diffuse out from the deeper layers. Accretion does not subside immediately after the explosion sets in. There can be an extended phase of continued mass accretion by the nascent neutron star that proceeds simultaneously to the outward acceleration of mass behind the outgoing shock. However, after hundreds of milliseconds, depending on the progenitor star and the speed of shock expansion, accretion ends and the proto-neutron star enters its cooling phase, in which it loses its remaining gravitational binding energy by the emission of neutrinos and antineutrinos of all flavors. While the proto-neutron star deleptonizes and cools by neutrino losses, the energetic neutrinos radiated from the neutrinosphere continue to deposit energy in the overlying, cooler layers, mainly by the reactions of Equations (4.3a) and (4.3b). This leads to an outflow of mass from the surface of the nascent neutron star. This is the so called neutrino driven wind, thought as a potential site for the formation of trans-iron elements. The mass loss rate and expansion velocity of this wind are sensitive functions of the neutron star radius and mass and of the luminosities and spectral hardness of the emitted neutrinos.

4.2 Supernova neutrino emission phases

The neutrino signal emitted from a SN explosion lasts for more than 10 s but the luminosity drops considerably after few seconds. Figures (4.1) and (4.2) represent the neutrino and antineutrino luminosities (4.1a), (4.2a) and mean energies (4.1b), (4.2b) for all neutrino flavors $(\nu_e, \overline{\nu}_e, \nu_x)$ as a function of post bounce time for SN progenitors of mass $M = 27\,M_\odot$ and $M = 11.2\,M_\odot$ at a distance of 10 kpc, assuming 1D spherically symmetric SN hydrodynamical simulations by the Garching group [54] and using the *Lattimer* and *Swesty* Equation of State with a nuclear incompressibility modulus of $k = 220\,MeV$ (LS220 EoS) and the *Shen* Equation of State, respectively, the same used in [52].
There are three main phases of the SN neutrino signal [55], corresponding to the dynamical evolution stages described in the previous Section (4.1): the neutronization burst, the post-bounce accretion phase and the cooling phase. The neutronization burst, shown in the left panel of both Figures (4.1) and (4.2), starts while the shock wave is moving outwards through the iron core, when the nuclear matter goes from being opaque to transparent for neutrinos. Free protons and neutrons are released as the shock wave dissociates iron nuclei. The large number of electron neutrinos created by electron capture on free protons in

the shock-heated matter can ultimately escape. The ν_e luminosity burst and the rise phase of the $\overline{\nu}_e$ and ν_x luminosities show a behavior with no dependence on the progenitor mass and EoS. The ν_e burst reaches a peak luminosity near $3.5 \times 10^{53}\, erg\, s^{-1}$ during the first 10 ms. In the same time window the mean energy of the radiated ν_e reaches a peak value of $\simeq 12\, MeV$. The post-bounce accretion phase, in the middle panel of both Figures (4.1) and (4.2), follows when the shock wave loses energy while moving outward until it stalls at a radius between 100 and 200 km. During this phase the ν_e luminosity declines from the maximum and levels off into a plateau. Both ν_e and $\overline{\nu}_e$ are produced in large numbers in the hot mantle of the proto-neutron star, as the capture of electrons (Equation (4.1)) and positrons (Equation (4.2)) on free nucleons starts to become more efficient. The ν_e and $\overline{\nu}_e$ luminosities are very similar during this phase with a slight number excess of ν_e because of ongoing deleptonization. In contrast, the individual luminosities of ν_x, produced via neutral current processes, are considerably lower. The mean energies of all neutrino flavors show an overall trend of increase which is steeper for ν_e and $\overline{\nu}_e$ than for ν_x. During the accretion phase, the neutrino emissions show large variation between different progenitor masses: in fact, progenitors with higher masses radiate higher luminosities having harder neutrino spectra. During the cooling phase, shown in the right panel of both Figures (4.1) and (4.2), neutrino signals gradually decrease as the proto-neutron star cools and deleptonizes. After the explosion, the proto-neutron star continues to radiate lepton number and energy by high neutrino fluxes. The luminosities of all neutrino and antineutrino flavors become similar and decline with time, reflecting the gradual cooling of the outer layers of the proto-neutron star.

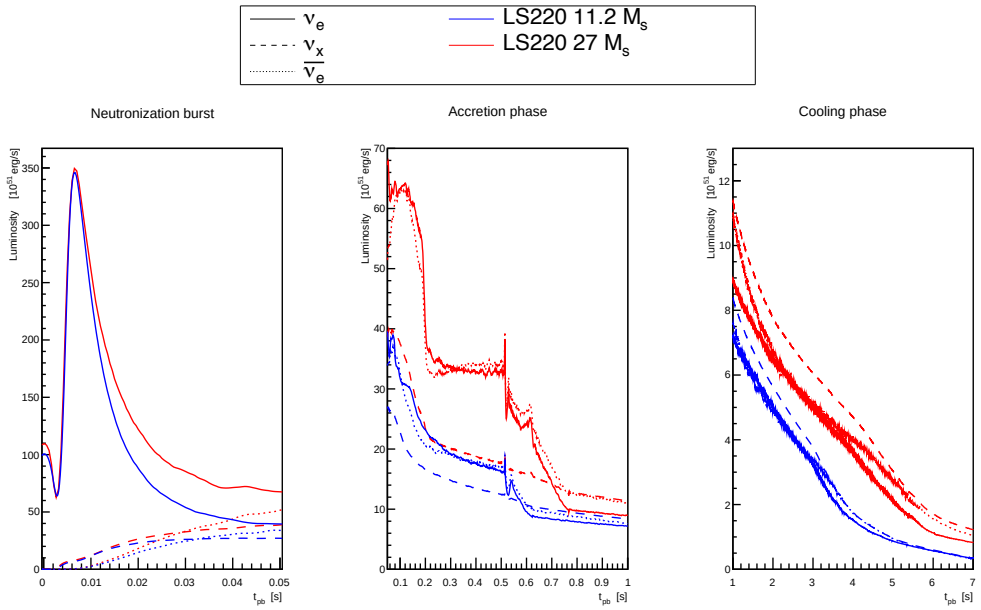

(a)

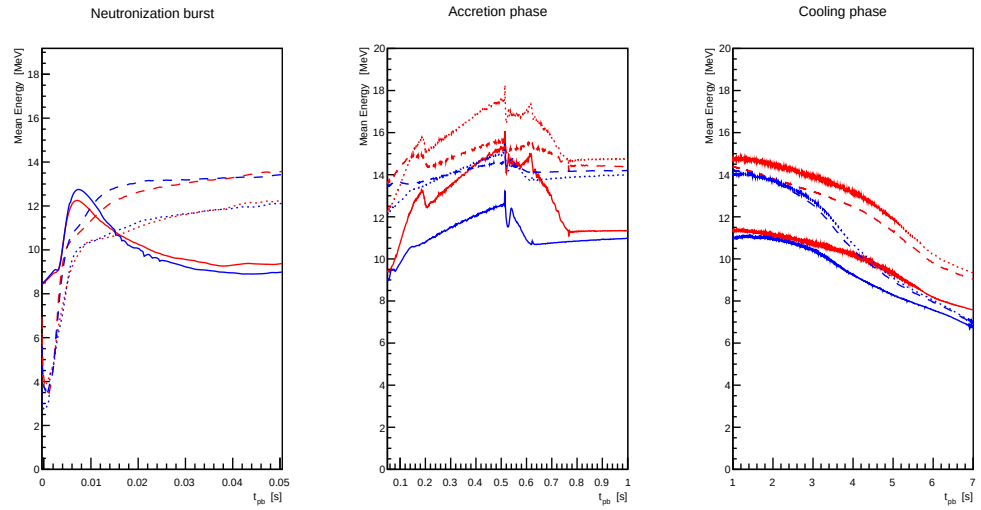

(b)

Figure 4.1: Neutrino and antineutrino luminosity (on top) and mean energy (on bottom) as functions of post-bounce time t_{pb} from different SN progenitor masses, using the LS220 EoS, during the three main phases of the emitted signal: the left panel shows the neutronization burst phase, the middle panel reports the accretion phase and the right one the final cooling phase. The differences in the neutrino properties from different progenitors during the neutronization burst are small, but become considerable at later times.

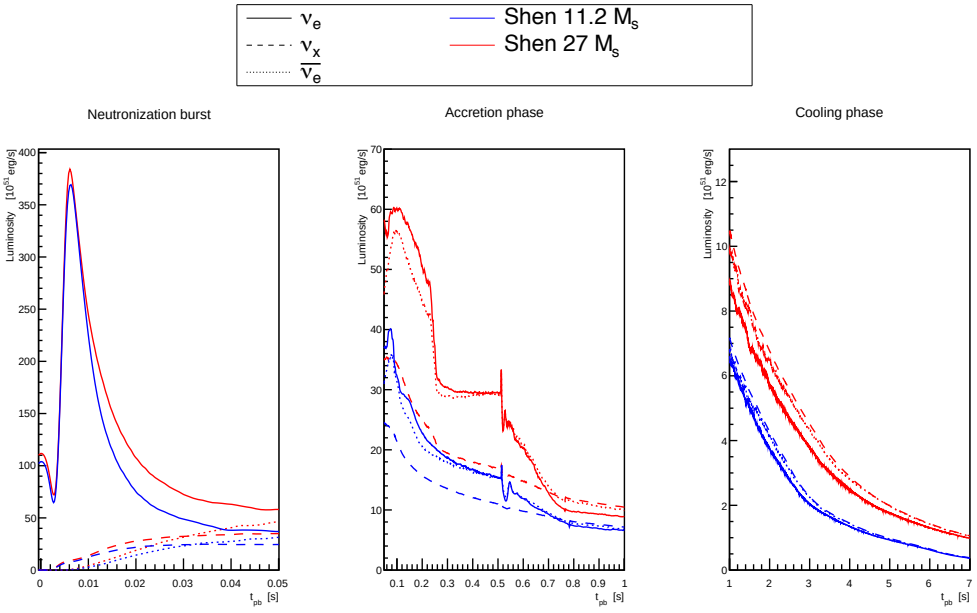

(a)

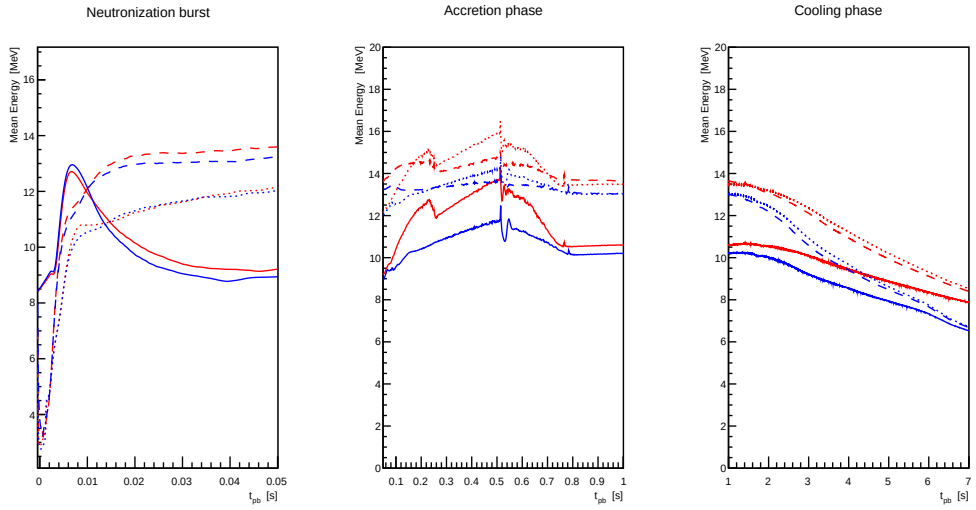

(b)

Figure 4.2: Neutrino and antineutrino luminosity (on top) and mean energy (on bottom) as functions of post-bounce time t_{pb} from different SN progenitor masses, using the Shen EoS, during the three main phases of the emitted signal: the left panel shows the neutronization burst phase, the middle panel reports the accretion phase and the right one the final cooling phase. The differences in the neutrino properties from different progenitors during the neutronization burst are small, but become considerable at later times.

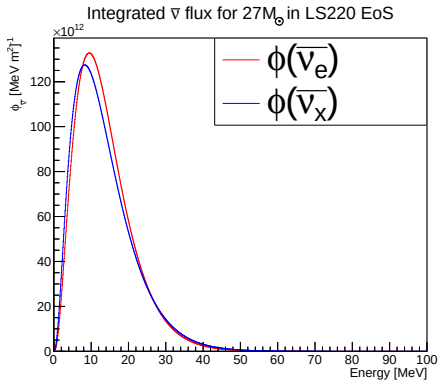

Figure 4.3: Comparison between integrated fluxes of non oscillated $\overline{\nu}_e$ and $\overline{\nu}_x$ for $27M_\odot$ progenitor star in LS220 EoS.

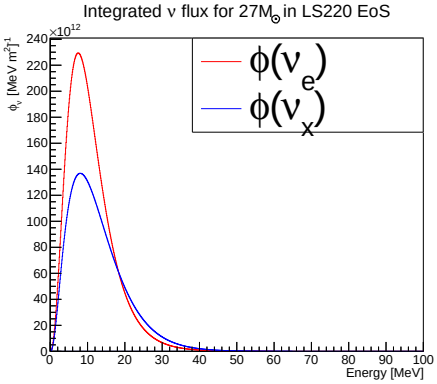

Figure 4.4: Comparison between integrated fluxes of non oscillated ν_e and ν_x for $27M_\odot$ progenitor star in LS220 EoS.

4.3 Supernova neutrino fluxes and oscillations

The differential flux for each neutrino flavor ν_β at a time t_{pb} after the SN core bounce at a distance d is parametrized by [52]

$$\Phi_{\nu_\beta}(E, t_{pb}) = \frac{L_{\nu_\beta}(t_{pb})}{4\pi d^2} \frac{\varphi_{\nu_\beta}(E, t_{pb})}{\langle E_{\nu_\beta}(t_{pb})\rangle}, \tag{4.4}$$

where $L_{\nu_\beta}(t_{pb})$ is the ν_β luminosity, $\langle E_{\nu_\beta}(t_{pb})\rangle$ the mean energy and $\varphi_{\nu_\beta}(E, t_{pb})$ is the neutrino energy distribution, defined as:

$$\varphi_{\nu_\beta}(E, t_{pb}) = \xi_\beta(t_{pb}) \left(\frac{E}{\langle E_{\nu_\beta}(t_{pb})\rangle}\right)^{\alpha_\beta(t_{pb})} \exp\left\{\frac{-[\alpha_\beta(t_{pb})+1]E}{\langle E_{\nu_\beta}(t_{pb})\rangle}\right\}. \tag{4.5}$$

The parameter $\alpha_\beta(t_{pb})$ satisfies the relation:

$$\alpha_\beta(t_{pb}) = \frac{2\langle E_{\nu_\beta}(t_{pb})\rangle^2 - \langle E^2_{\nu_\beta}(t_{pb})\rangle}{\langle E^2_{\nu_\beta}(t_{pb})\rangle - \langle E_{\nu_\beta}(t_{pb})\rangle^2}, \tag{4.6}$$

while $\xi_\beta(t_{pb})$ is a normalization factor defined such that

$$\int \varphi_{\nu_\beta}(E, t_{pb})\, dE = 1. \tag{4.7}$$

Considering the case of SN progenitor of mass $M = 27M_\odot$ at a distance of 10 kpc, using the LS220 EoS, Figures (4.3) and (4.4) show, respectively, the comparison between the integrated flux of non oscillated $\overline{\nu}_e$ and $\overline{\nu}_x$ and of ν_e and

ν_x. Here ν_x indicates ν_μ and ν_τ, while $\overline{\nu}_x$ their respective antineutrinos. In the study of SN neutrinos these are indistinguishable because the differences in their interactions are rather small and, correspondingly, also their emitted spectra are very similar.
Taking into account the neutrino oscillations, the integrated fluxes of Figures (4.3) and (4.4) are modified. As studied in Section (2.1.2), there is compelling experimental evidence that the three known active neutrino states with definite flavor ν_l $(l = e, \mu, \tau)$ are linear combinations of the mass eigenstates n_k $(k = 1, 2, 3)$, (2.26). In the standard three-flavors scenario, in fact, the three know flavor eigenstates are mixed with the three mass eigenstates through the unitary matrix U defined in (2.27). Here extra phases, possible if neutrinos are Majorana particles, are neglected, since these are not relevant in oscillations.
The current neutrino phenomenology implies that the three-neutrino mass spectrum m_k, $(k = 1, 2, 3)$, is made by a doublet of relatively close states and by a third lone neutrino state, which may be either heavier than the doublet (normal ordering, NO) or lighter (inverted ordering, IO) [53]. Typically, the lightest neutrino in the doublet is n_1 and the heaviest one is n_2: the corresponding mass squared difference, named as the solar mass squared difference, is defined, by convention, as

$$\Delta m^2_{sol} = m_2^2 - m_1^2 > 0\,. \tag{4.8}$$

The lone state is then labeled as n_3. The second independent squared mass difference Δm^2_{atm}, called atmospheric mass squared difference, is defined as

$$\Delta m^2_{atm} = \left| m_3^2 - \frac{m_1^2 + m_2^2}{2} \right|, \tag{4.9}$$

and its physical sign distinguishes the ordering of neutrino mass spectrum: for the normal ordering we have $\Delta m^2_{atm} > 0$ with $m_1 < m_2 < m_3$, for the inverted one $\Delta m^2_{atm} < 0$ with $m_3 < m_1 < m_2$. The existing data do not allow one to determine its sign. Numerically, it results that

$$\left|\Delta m^2_{atm}\right| \gg \Delta m^2_{sol}\,. \tag{4.10}$$

The latest solar, reactor and long-baseline neutrino oscillation analyses indicate the 3σ ranges for each parameter, reported in Table (4.1) [15, 56]. The measurement of a large value of the mixing angle $\theta_{13} \simeq 8.13°$ has significantly reduced the ambiguity in characterizing the SN neutrino oscillations.
Streaming through the outer layers of the stellar envelope, as the SN matter potential declines, neutrino and antineutrinos would feel ordinary matter effects. In their path from the high density region where they are generated to the lower density one where they escape the star, they cross two resonance layers, called Mikheyev-Smirnov-Wolfenstein resonance layers [57]. These two resonant regions are rather separated because of relation (4.10) between the two squared

Table 4.1: The best-fit values and 3σ allowed ranges of the three neutrino oscillation parameters, derived from a global fit of the current neutrino oscillation data. For the Dirac phase δ we give the best fit value and the 2σ allowed range. The values correspond to NO mass spectrum, while that in brackets correspond to the IO one. We give the values of $\Delta m^2_{31} > 0$ for NO and of Δm^2_{23} for IO.

Parameter	Best-fit	3σ
$\Delta m^2_{sol}\,[10^{-5}\ eV^2]$	7.37	$6.93 - 7.96$
$\Delta m^2_{31(23)}\,[10^{-3}\ eV^2]$	2.56 (2.54)	$2.45 - 2.69$ $(2.42 - 2.66)$
$\sin^2\theta_{12}$	0.297	$0.250 - 0.354$
$\sin^2\theta_{23}$, $\Delta m^2_{31(23)} > 0$	0.425	$0.381 - 0.615$
$\sin^2\theta_{23}$, $\Delta m^2_{23(31)} < 0$	0.589	$0.384 - 0.636$
$\sin^2\theta_{13}$, $\Delta m^2_{31(23)} > 0$	0.0215	$0.0190 - 0.0240$
$\sin^2\theta_{13}$, $\Delta m^2_{23(31)} < 0$	0.0216	$0.0190 - 0.0242$
Dirac phase	Best-fit	2σ
δ/π	1.38 (1.31)	$1.0 - 1.9$ $(0.92 - 1.88)$

masses. The oscillation scheme of SN neutrinos for normal ordering is

$$\Phi_{\nu_e} = P_H U^2_{e2} \Phi^0_{\nu_e} + (1 - P_H U^2_{e2}) \Phi^0_{\nu_x}\,; \tag{4.11a}$$

$$\Phi_{\bar{\nu}_e} = U^2_{e1} \Phi^0_{\bar{\nu}_e} + U^2_{e2} \Phi^0_{\bar{\nu}_x}\,, \tag{4.11b}$$

while the one for inverted ordering is

$$\Phi_{\nu_e} = U^2_{e2} \Phi^0_{\nu_e} + U^2_{e1} \Phi^0_{\nu_x}\,; \tag{4.12a}$$

$$\Phi_{\bar{\nu}_e} = P_H U^2_{e1} \Phi^0_{\bar{\nu}_e} + (1 - P_H U^2_{e1}) \Phi^0_{\bar{\nu}_x}\,, \tag{4.12b}$$

[58], where P_H is the probability to jump onto an adjacent mass eigenstate crossing the H-resonance layer, Φ^0 is referred to non oscillated flux and, from the neutrino mixing matrix defined in (2.27):

$$U^2_{e1} = \cos^2\theta_{13} \cos^2\theta_{12} \simeq \cos^2\theta_{12}\,; \tag{4.13a}$$

$$U^2_{e2} = \cos^2\theta_{13} \sin^2\theta_{12} \simeq \sin^2\theta_{12}\,. \tag{4.13b}$$

Figures (4.5) and (4.6) show level crossing diagrams for the two mass spectra with normal ordering and inverted one, respectively. Blue lines represent the eigenvalues of the effective Hamiltonian as function of electron number density. Black dotted lines correspond to the energy of the flavor levels ν_e and ν_x. Negative values of the electron number density are related to the antineutrino

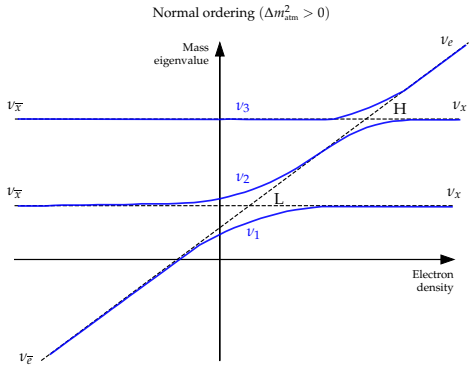

Figure 4.5: Level crossing diagrams for mass spectrum with normal ordering.

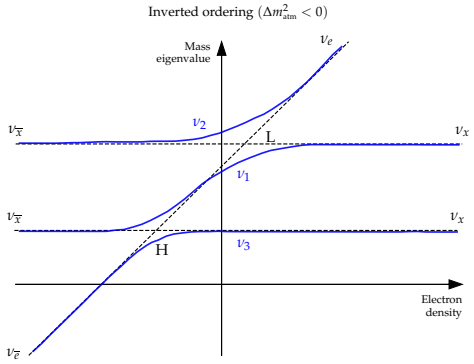

Figure 4.6: Level crossing diagrams for mass spectrum with inverted ordering.

channel: these are represented on the same level crossing diagram as neutrinos traveling through matter with effectively negative electron density. For typical SN simulations, the matter density profile declines so slowly that the neutrino propagation is adiabatic: each mass eigenstate in Figures (4.5) and (4.6) remains the same. However this condition is violated at the shock fronts where, due to the abrupt density change, strong non adiabatic conversions occur. For θ_{13} as large as recently measured, the H-resonance is adiabatic, so the flip probability is null: $P_H = 0$. Instead, at the shock fronts, this resonance is completely non adiabatic, so the flip probability is $P_H = 1$. The L-resonance intercepts the shock front only at relatively late times $\left(t_{pb} > 10\ s\right)$ and it is never strongly non adiabatic: sub-leading effects related to level crossing probability $P_L \neq 0$ are typically neglected. In adiabatic conditions, the oscillation schemes of Equations (4.11) and (4.12) become

$$\Phi_{\nu_e} = \Phi^0_{\nu_x}\,; \tag{4.14a}$$

$$\Phi_{\bar{\nu}_e} = \cos^2\theta_{12}\Phi^0_{\bar{\nu}_e} + \sin^2\theta_{12}\Phi^0_{\bar{\nu}_x}\,, \tag{4.14b}$$

for the normal ordering and

$$\Phi_{\nu_e} = \sin^2\theta_{12}\Phi^0_{\nu_e} + \cos^2\theta_{12}\Phi^0_{\nu_x}\,; \tag{4.15a}$$

$$\Phi_{\bar{\nu}_e} = \Phi^0_{\bar{\nu}_x}\,, \tag{4.15b}$$

for the inverted one. Replacing the numerical values of $\sin^2\theta_{12}$ and $\cos^2\theta_{12}$, we obtain the fluxes of Figures (4.7), (4.8), (4.9) and (4.10).

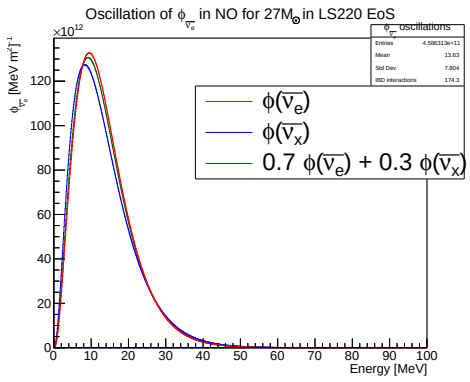

Figure 4.7: Comparison between fluxes of $\overline{\nu}_e$, $\overline{\nu}_x$ and $\overline{\nu}_e$ oscillated in Normal adiabatic ordering for $27M_\odot$ progenitor star in LS220 EoS. The green line represents the oscillated flux of $\overline{\nu}_e$ of Equation (4.14b).

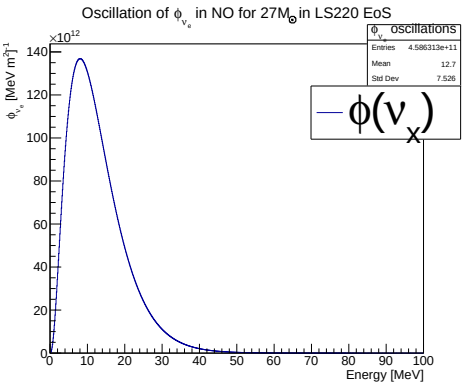

Figure 4.8: Flux of ν_e in Normal adiabatic ordering for $27M_\odot$ progenitor star in LS220 EoS. From Equation (4.14a), the oscillated flux of ν_e is equal to that of non oscillated ν_x.

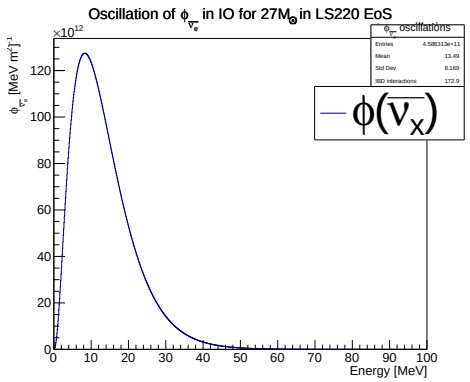

Figure 4.9: Flux of $\overline{\nu}_e$ in Inverted adiabatic ordering for $27M_\odot$ progenitor star in LS220 EoS. From Equation (4.15b), the oscillated flux of $\overline{\nu}_e$ is equal to that of non oscillated $\overline{\nu}_x$.

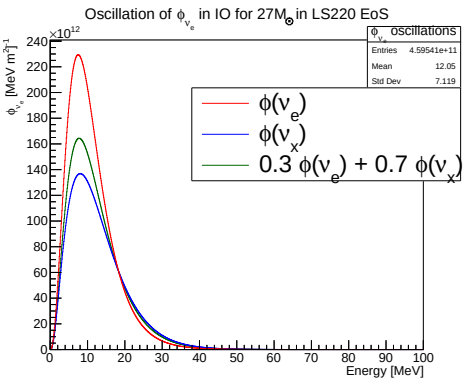

Figure 4.10: Comparison between fluxes of ν_e, ν_x and ν_e oscillated in Inverted adiabatic ordering for $27M_\odot$ progenitor star in LS220 EoS. The green line represents the oscillated flux of ν_e of Equation (4.15a).

Chapter 5

Supernova neutrino detection with nVeto and mVeto

E tu, Cielo, dall'alto dei mondi,
sereni, infinito, immortale,
oh! d'un pianto di stelle lo inondi
quest'atomo opaco del Male.

Giovanni Pascoli
X Agosto

In this Chapter, we study the detection efficiencies of XENONnT muon and neutron Vetoes for inverse beta decay interactions of SN electron antineutrinos in water. Positrons and captured neutrons produce Čerenkov light in Gd-doped water (at 0.2% mass concentration), that can be detected by the array of 84 mVeto and 120 nVeto PMTs. Positrons and neutrons are generated through a Monte Carlo simulations, performed using the XENONnT GEANT4 code. Focusing on neutrinos coming from two different SN progenitors of $27M_{\odot}$ in LS220 EoS and of $11.2M_{\odot}$ in Shen EoS, the XENONnT detection efficiencies are obtained.

5.1 Inverse beta decay process

Water is rich in free protons, which have a rather large and well known cross section for interaction with low energy electron antineutrinos $\overline{\nu}_e$ via inverse beta decay process:

$$\overline{\nu}_e + p \longrightarrow n + e^+ . \tag{5.1}$$

Figure (5.1) shows the cross section of the inverse beta decay as a function of

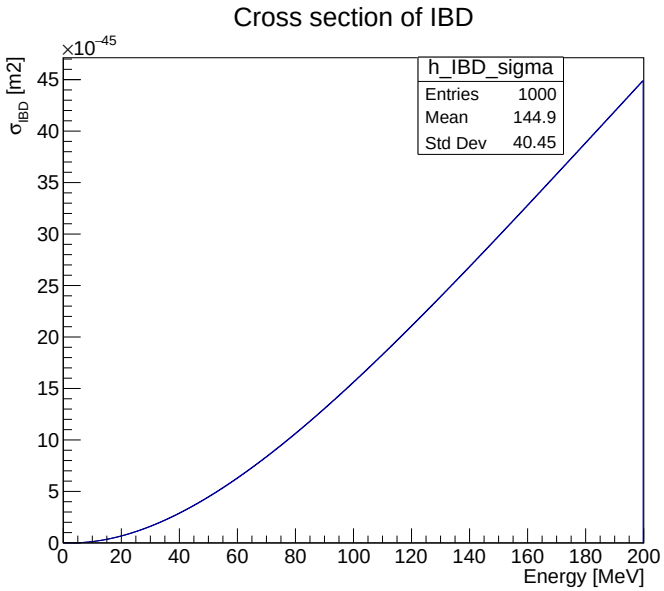

Figure 5.1: Cross section of the IBD process as function of energy.

energy. The threshold energy for this process is given by:

$$E_{\overline{\nu}_e} = m_n + m_{e^+} - m_p = 1.806\,MeV\,, \tag{5.2}$$

where m_n, m_{e^+} and m_p are the rest masses of neutron, positron and proton respectively. Most of the antineutrino energy is taken by the positron because $m_{e^+} \ll m_n$. Produced e^+, after depositing their kinetic energy in the medium, undergoes annihilation with e^-, while produced n can be detected after moderation and capture in water. If captured on a free proton:

$$n + p \longrightarrow d + \gamma\,, \tag{5.3}$$

a photon γ of $2.2\,MeV$ is produced. Other nuclei, as the gadolinium (Gd), can also capture neutrons with higher cross section, and the subsequent de-excitation photons of $8\,MeV$ can be detected. The timing of the delayed capture is about $(200 \div 300)$ µs after IBD starts. The timing and spatial coincidences between the positron annihilation and the neutron capture provide a clear IBD signature in neutrino detector, allowing for discrimination from background. The IBD signal is the main one in water Čerenkov detectors and scintillators: it is given by a continuous spectrum due to the positron energy release, directly connected with the $\overline{\nu}_e$ energy. In fact, the emitted positrons have energy given by

$$E_{e^+} = E_{\overline{\nu}_e} - 1.806\,MeV\,, \tag{5.4}$$

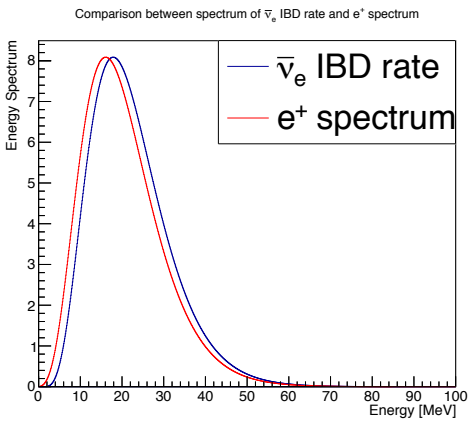

Figure 5.2: Comparison between blue line, which represents the rate of IBD interactions of non oscillated electron antineutrinos $\bar{\nu}_e$ originated from SN progenitor of $27M_\odot$ in LS220 EoS as a function of energy, and the red one, which is the energy spectrum of positrons produced via IBD, given in Equation (5.4).

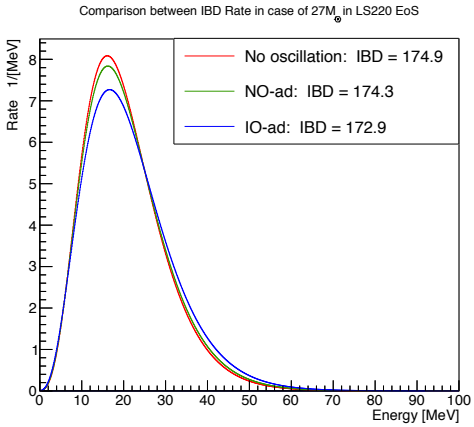

Figure 5.3: Comparison between spectra of positrons produced via IBD from interaction of non oscillated $\bar{\nu}_e$ (red line), oscillated $\bar{\nu}_e$ in NO (green line) and oscillated $\bar{\nu}_e$ in IO (blue line) originated from SN progenitor of $27M_\odot$ in LS220 EoS. It is easy to see that the expected number of IBD interactions is not very different in the three cases because the three spectra are very similar.

and its shape is shown by the red line of Figure (5.2).
Considering a target volume of 700 t of pure water, with the non oscillated electron antineutrino spectrum from SN progenitor of mass $27M_\odot$ in LS220 EoS, the red one in Figure (4.7), the total number of expected IBD interactions is about 175. The shape of IBD events rate as a function of energy is shown by the blue line in Figure (5.2).
Neutrino oscillations do not modify significantly the expected number of IBD interactions, indeed, in this particular SN model, the temperatures of the $\bar{\nu}_e$ and $\bar{\nu}_x$ neutrino-spheres are very similar. In fact, considering again a target volume of 700 t of pure water, we obtain the results of Figure (5.3): in adiabatic conditions and in case of mass spectrum with normal ordering, we expect about 174 IBD interactions while, in case of mass spectrum with inverted one, we expect about 173 IBD interactions. Considering now both cases of SN progenitor masses and Equations of State analyzed in Figures (4.1) and (4.2), taking into account the oscillations effects described by Equations (4.14) and (4.15), we obtain the comparison between different numbers of expected IBD interactions in both Normal and Inverted mass ordering, shown, respectively, in Figures (5.4) and (5.5). To make clear the differences in expected IBD interactions related to

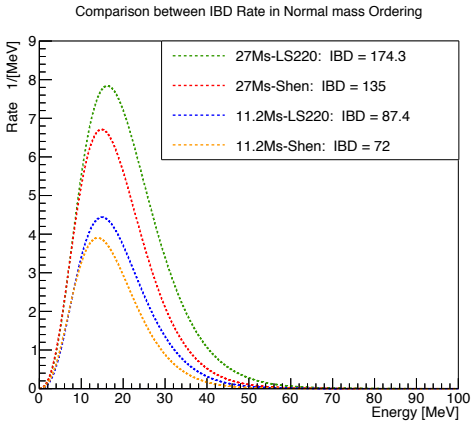

Figure 5.4: Comparison between expected IBD rate for different SN progenitors in both LS220 and Shen EoS assuming Normal ordering mass spectra.

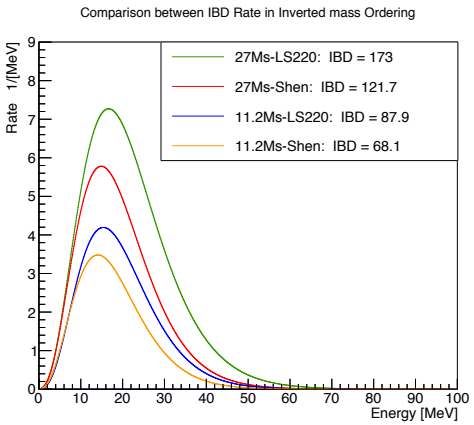

Figure 5.5: Comparison between expected IBD rate for different SN progenitors in both LS220 and Shen EoS assuming Inverted ordering mass spectra.

the same SN progenitor due to the different oscillation scenarios and Equation of State adopted, Figure (5.6) and Figure (5.7) show the expected IBD rate of SN progenitors of masses $27M_{\odot}$ and $11.2M_{\odot}$, respectively. The interest of the following analysis is in determining the detection efficiency ϵ of XENONnT nVeto and mVeto, that is the probability that the detectors can observe the interactions of positrons and neutrons.

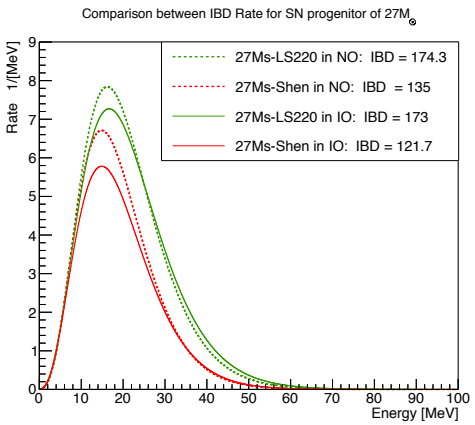

Figure 5.6: Comparison between the expected IBD rate for different oscillation scenarios and Equations of State used, for SN progenitor of $27M_{\odot}$.

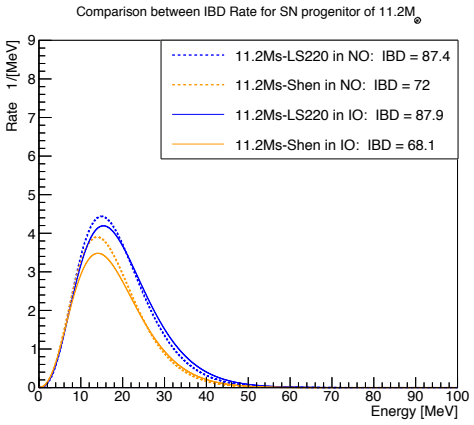

Figure 5.7: Comparison between the expected IBD rate for different oscillation scenarios and Equations of State used, for SN progenitor of $11.2M_{\odot}$.

5.2 Detection efficiency of positrons in water

Assuming the nVeto Box configuration with 120 PMTs and three small holes for the interference with calibration system, we simulated, isotropically in the whole water volume, 10^5 positrons from IBD interactions of non oscillated electron antineutrinos produced by SN progenitor of mass $27M_\odot$ in LS220 Equation of State, with energy spectrum given by the red line of Figure (5.2). To get an idea about the number of events generated in mVeto and nVeto, we can observe their respective volumes:

- volume of mVeto: $611.3\,m^3$,
- volume of nVeto: $52.5\,m^3$.

The volume of nVeto is about 8% of that of mVeto, so we expect that the most of events are generated outside the nVeto. Requiring a certain PMTs multiplicity, without any distinction between the two detectors, we obtain the efficiency plot in Figure (5.8): blue line represents the detection efficiency as a function of the number of PMTs required in coincidence, while the red one shows the detection efficiency, always as a function of the number of PMTs in coincidence, with all of them from nVeto or mVeto. Requiring 10 PMTs in coincidence, blue line shows that the total detection efficiency for simulated positrons is $\epsilon = 0.99$. Given this value, it is possible to compute the number of detected IBD interactions: in fact, not all the expected events are effectively observed. Taking into account the neutrino oscillations, referring to Figures (5.4) and (5.5) and requiring 10 PMTs in coincidence, we obtain the effective number of detected IBD interaction. Considering another SN progenitor, the one with mass of $11.2M_\odot$ in the Shen Equation of State, the comparison between the expected number of IBD events and the detected one, in both SN mass cases, is shown in Table (5.1). Figure (5.9) reports the energy deposited in water: blue line represents the energy of all events and the red dotted one is the energy tagged with 10 PMTs in coincidence. We can see that, for energies greater than $6\,MeV$, all events are detected as the tagging efficiency in Figure (5.10) shows. Figure (5.11) and Figure (5.12) represent, respectively, the distribution of the total number of detected photoelectrons over the total number of PMTs and the distribution of detected photoelectrons in each PMT. A separate analysis on nVeto and mVeto detectors, always considering events generated isotropically in both volumes without any distinction, produces the plots in Figures (5.13) and (5.14): red lines represent the contribution to the detection efficiency of events generated outside the detector to which we are referring, while blue ones are the contribution to the detection efficiency of events generated in the detector itself. Green lines show the sum of the two contribution, so the total efficiency in both cases. In case of nVeto in Figure (5.13) we observe the peak at low multiplicity, due to the fact that most of

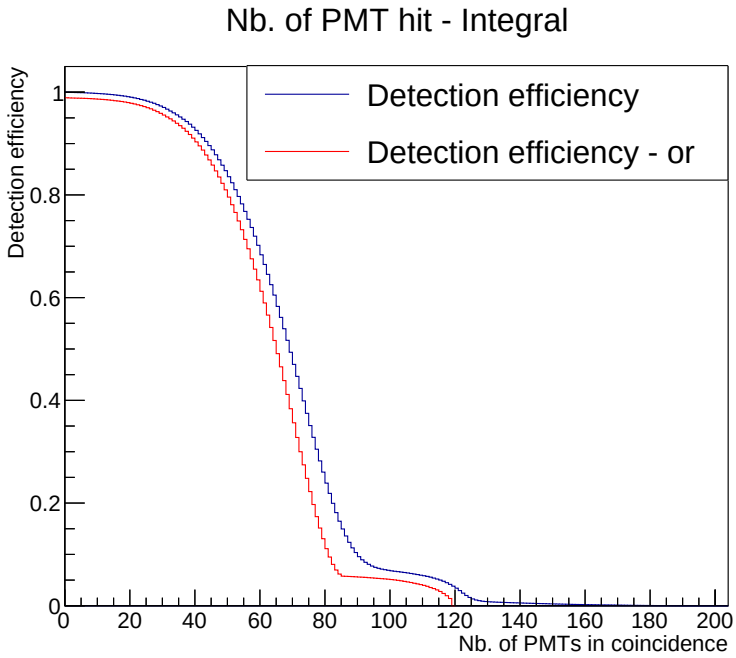

Figure 5.8: Comparison between the detection efficiency of positrons generated by interactions of $\overline{\nu}_e$ produced by SN progenitor of $27M_\odot$ in LS220 EoS as a function of the number of PMTs required in coincidence, with no distinction between nVeto and mVeto (blue line) and requiring that all the PMTs in coincidence belong to nVeto or mVeto (red line).

simulated events are detected by both nVeto and mVeto detectors. Considering instead the detection efficiency of nVeto and mVeto for events generated only in their respective volumes, we obtain the results of Figures (5.15) and (5.16). In both nVeto and mVeto, with 10 PMTs in coincidence, we obtain an efficiency of $\epsilon = 0.99$. Green lines of Figure (5.17) and Figure (5.18) show, respectively, the distribution of the total number of photoelectrons in nVeto and mVeto. Here, red lines represent the contribution due to events generated in nVeto, while blue lines the one due to events generated in mVeto. As we expect, most of the light is produced by events generated in the detector we are considering. Figures (5.19) and (5.20) show the distribution of detected photoelectrons in each PMT of nVeto and mVeto, respectively.
Performing this same analysis on positrons produced via IBD interactions of non oscillated electron antineutrinos by SN progenitor of mass $11.2M_\odot$ in the Shen Equation of State, we obtained the efficiency plots of Figures (5.21), (5.22), (5.23), (5.24) and (5.25).

Figure (5.21), as Figure (5.8), shows the comparison between blue line, which

Table 5.1: Comparison between different numbers of expected IBD interactions and detected IBD interactions, requiring 10 PMTs in coincidence, coming from different SN progenitors in both Equations of State and mass orderings. Thanks to the high value of detection efficiency, almost all IBD events are detected.

Solar Mass	EoS	Mass Ordering	Expected IBD	Detected IBD
$27M_{\odot}$	LS220	NO	174.3	173.9
		IO	172.9	172.5
	Shen	NO	135.0	134.7
		IO	121.7	121.4
$11.2M_{\odot}$	LS220	NO	87.4	87.2
		IO	87.9	87.7
	Shen	NO	71.9	71.8
		IO	68.1	67.9

is the detection efficiency of positrons as a function of the number of PMTs required in coincidence, with no distinction between nVeto and mVeto detectors and the red one, which is the detection efficiency requiring that all the PMTs in coincidence belong to nVeto or mVeto. Also in this case blue line shows that, requiring 10 PMTs in coincidence, the detection efficiency is $\epsilon = 0.99$.
Figures (5.22) and (5.23), as Figures (5.13) and (5.14), show, respectively, the contributions to nVeto and mVeto efficiency due to all events generated in nVeto and outside it: green lines represent the sum of two contributions.
Figures (5.24) and (5.25), as Figures (5.15) and (5.16), represent, respectively, the nVeto and mVeto efficiency considering only positrons generated in the detector itself.
Also in this case, requiring 10 PMTs in coincidence, both nVeto and mVeto measure an efficiency of $\epsilon = 0.99$.

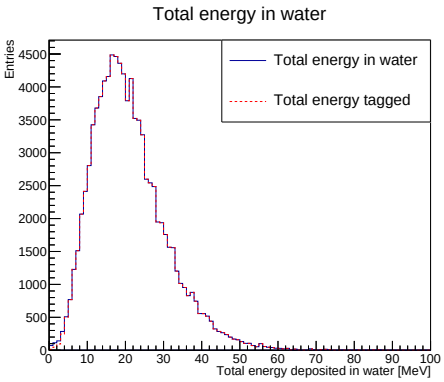

Figure 5.9: Comparison between total energy deposited in water (blue line) and total energy tagged requiring 10 PMTs in coincidence (red dotted line).

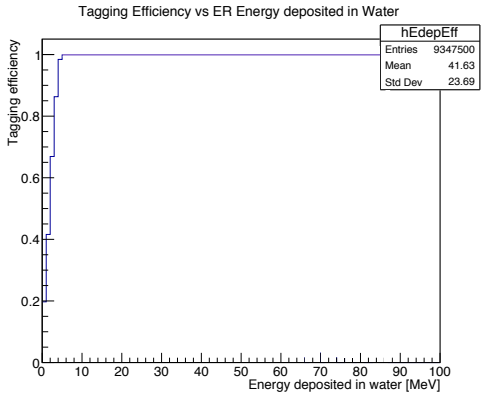

Figure 5.10: Tagging efficiency as a function of the deposited energy in water. For energies greater than about $6\,MeV$, all events are tagged.

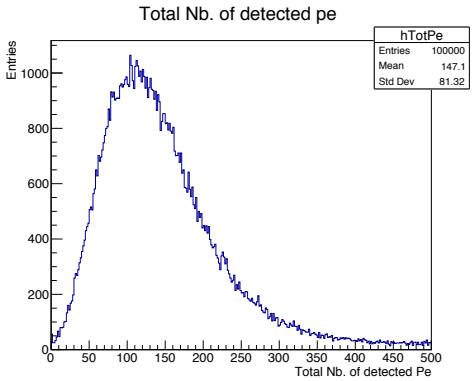

Figure 5.11: Distribution of the total number of detected photoelectrons over the total number of PMTs.

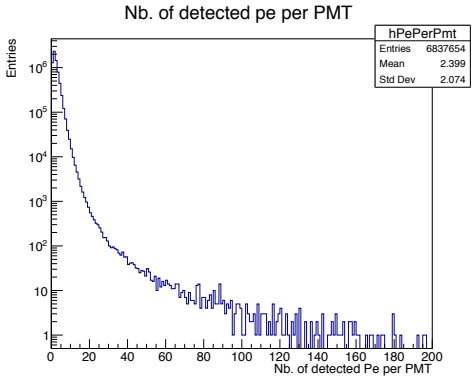

Figure 5.12: Distribution of detected photoelectrons in each PMT.

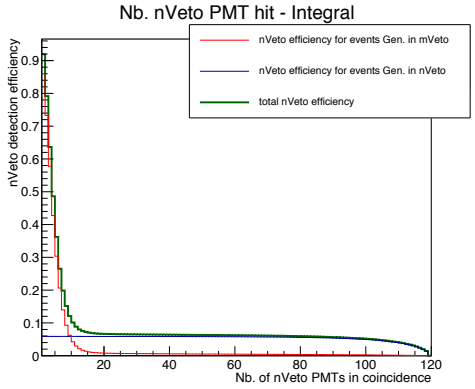

Figure 5.13: Detection efficiency of nVeto detector as a function of the number of PMTs required in coincidence for positrons from SN progenitor of $27M_{\odot}$ in LS220 EoS. Red line shows the contribution to the nVeto detection efficiency of events generated in mVeto, blue one the contribution of events generated in nVeto. Green line is the sum of the two contributions.

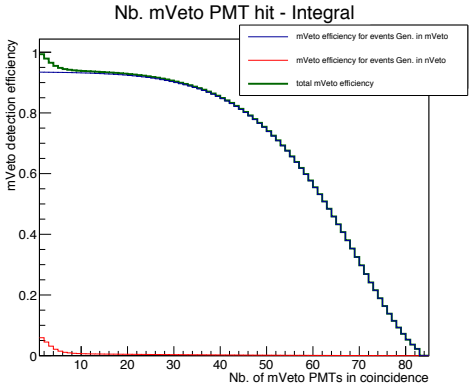

Figure 5.14: Detection efficiency of mVeto detector as a function of the number of PMTs required in coincidence for positrons from SN progenitor of $27M_{\odot}$ in LS220 EoS. Red line shows the contribution to the mVeto detection efficiency of events generated in nVeto, blue one the contribution of events generated in mVeto. Green line is the sum of the two contributions.

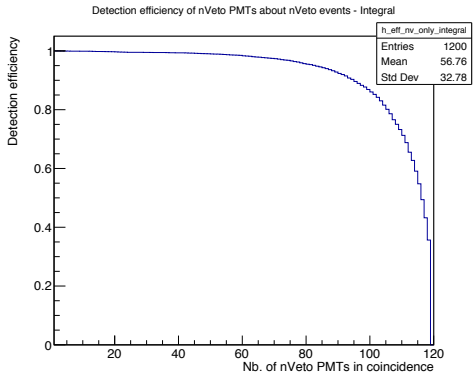

Figure 5.15: Detection efficiency of nVeto detector as a function of the number of PMTs required in coincidence only for positrons from SN progenitor of $27M_{\odot}$ in LS220 EoS generated in the nVeto itself.

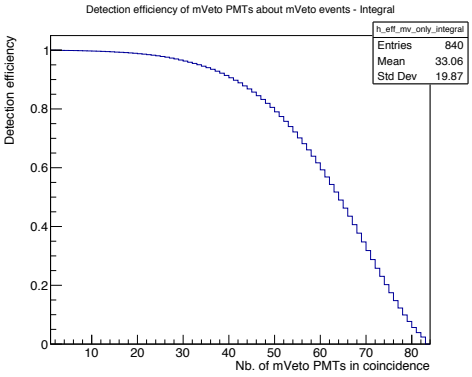

Figure 5.16: Detection efficiency of mVeto detector as a function of the number of PMTs required in coincidence only for positrons from SN progenitor of $27M_{\odot}$ in LS220 EoS generated in the mVeto itself.

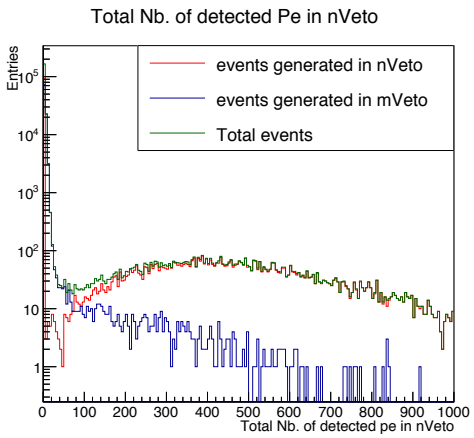

Figure 5.17: Distribution of the total number of detected photoelectrons in nVeto. Red line shows the contribution of events generated inside the nVeto while the blue one shows that of events generated inside the mVeto. Green line is the sum of two contributions.

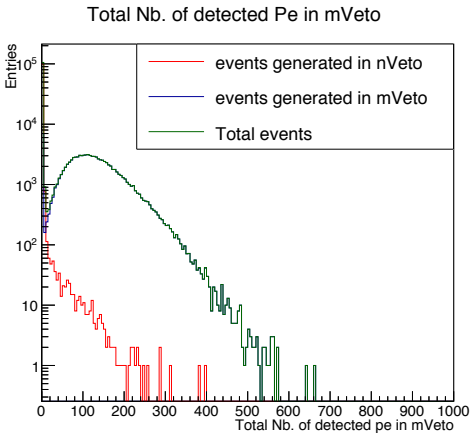

Figure 5.18: Distribution of the total number of detected photoelectrons in mVeto. Red line shows the contribution of events generated inside the nVeto while the blue one shows that of events generated inside the mVeto. Green line is the sum of two contributions.

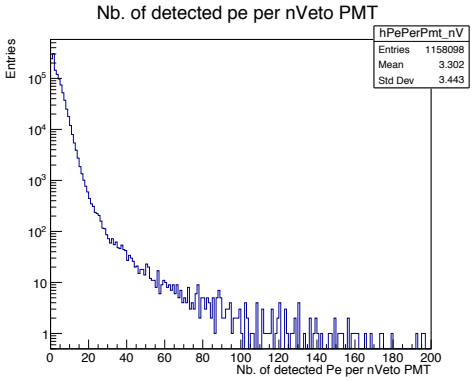

Figure 5.19: Distribution of detected photoelectrons in each PMT of nVeto.

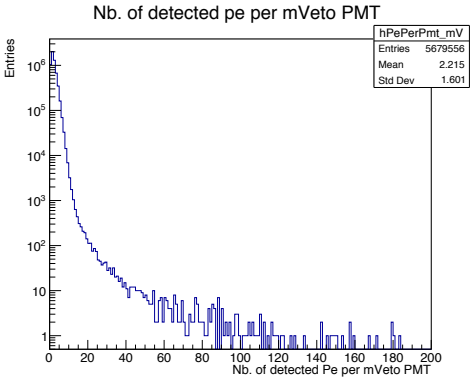

Figure 5.20: Distribution of detected photoelectrons in each PMT of mVeto.

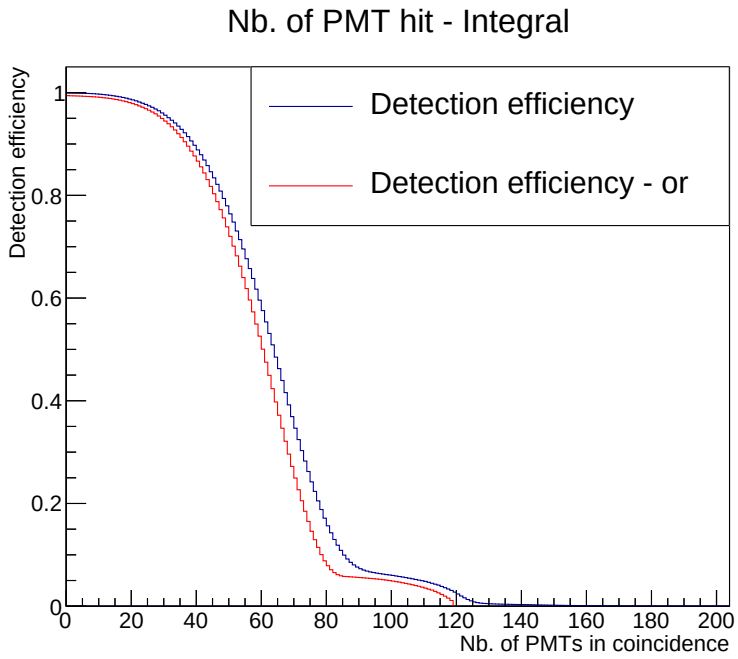

Figure 5.21: Comparison between the detection efficiency of positrons generated by interactions of $\overline{\nu}_e$ produced by SN progenitor of $11.2M_\odot$ in Shen EoS as a function of the number of PMTs required in coincidence, with no distinction between nVeto and mVeto (blue line) and requiring that all the PMTs in coincidence belong to nVeto or mVeto (red line).

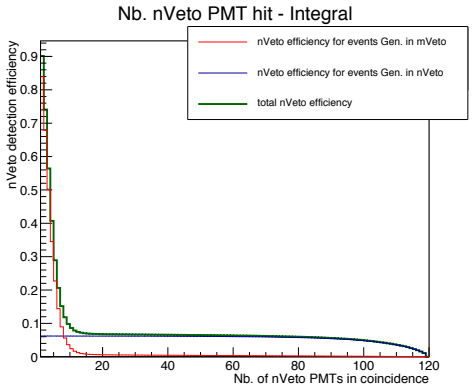

Figure 5.22: Detection efficiency of nVeto detector as a function of the number of PMTs required in coincidence for positrons from SN progenitor of $11.2M_{\odot}$ in Shen EoS. Red line shows the contribution to the nVeto detection efficiency of positrons generated in mVeto, blue one the contribution of positrons generated in nVeto. Green line is the sum of two contributions.

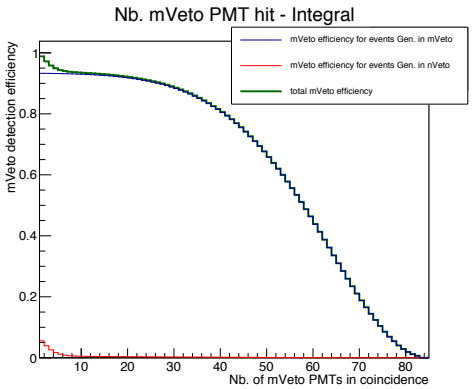

Figure 5.23: Detection efficiency of mVeto detector as a function of the number of PMTs required in coincidence for positrons from SN progenitor of $11.2M_{\odot}$ in Shen EoS. Red line shows the contribution to the mVeto detection efficiency of positrons generated in nVeto, blue one the contribution of positrons generated in mVeto. Green line is the sum of two contributions.

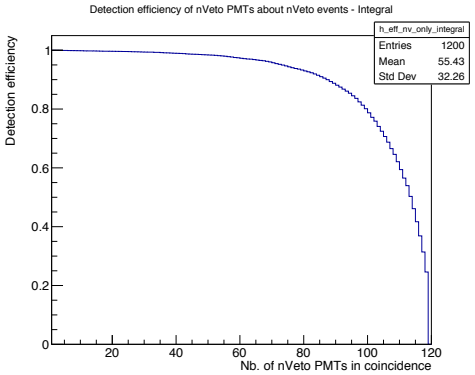

Figure 5.24: Detection efficiency of nVeto detector as a function of the number of PMTs required in coincidence only for positrons from SN progenitor of $11.2M_{\odot}$ in Shen EoS generated in the nVeto itself.

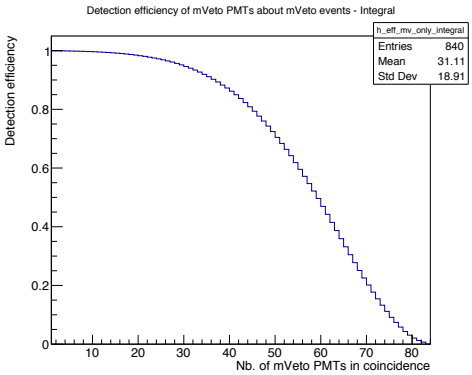

Figure 5.25: Detection efficiency of mVeto detector as a function of the number of PMTs required in coincidence only for positrons from SN progenitor of $11.2M_{\odot}$ in Shen EoS generated in the mVeto itself.

5.3 Detection efficiency of neutrons in Gd-doped water

As described in Section 3.4, doping the water of the outer shield with Gd-sulphate at 0.2% mass concentration, the neutrons capture efficiency will be improved. Once a neutron interacts in the detector, there is an high probability it will be captured on Gd nuclei, releasing a cascade of gammas with total energy of about $8\,MeV$. The presence of Gd in water, together with the presence of nVeto, improves considerably the possibility to discriminate NR background events in the TPC, reducing the background for the WIMPs search. In fact a NR event in the TPC, in coincidence with a neutron capture, allows to tag this NR event as a background event, due to the previous interaction of the same captured neutron in the TPC. With the presence of Gd and of the nVeto, the detection efficiency of neutrons will increase. Thanks to this point we are able to study also the detection efficiency of XENONnT to neutrons produced by IBD process (5.1).

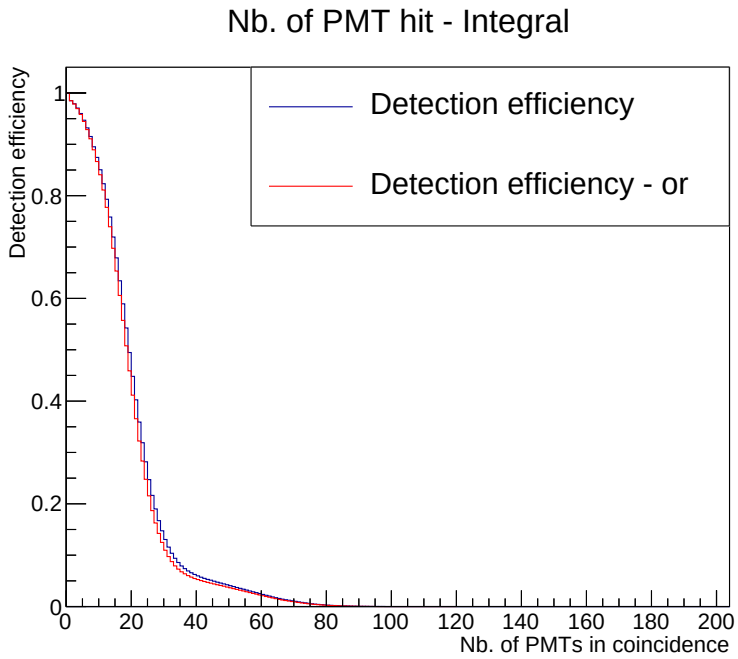

Figure 5.26: Comparison between the detection efficiency of neutrons as a function of the number of PMTs in coincidence, with no distinction of nVeto or mVeto PMTs (blue line) and requiring that all of the PMTs in coincidence belong to nVeto or mVeto (red line).

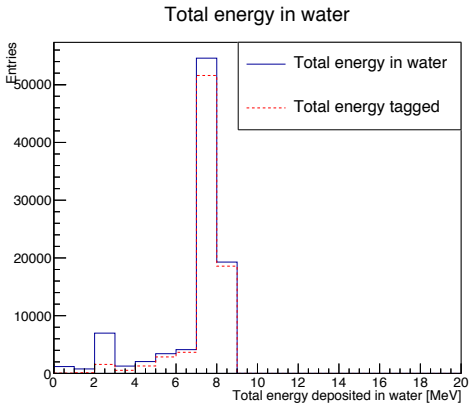

Figure 5.27: Comparison between total energy deposited in water (blue line) and total energy tagged requiring 10 PMTs in coincidence (red dotted line).

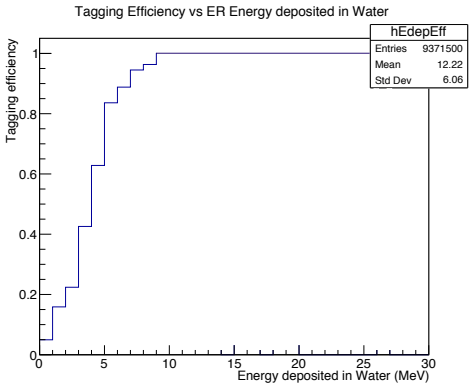

Figure 5.28: Tagging efficiency as a function of the deposited energy in water.

We generated isotropically in the whole water volume, 10^5 neutrons of 1 keV energy. Performing the same analysis done in the positrons case, we estimate the detection efficiency of XENONnT detectors for this type of event. Without any distinction between nVeto and mVeto detectors, the total detection efficiency is shown by the blue line of Figure (5.26). Here is shown the comparison with the red line, which represents the detection efficiency requiring that all of the PMTs in coincidence belong to nVeto or mVeto. Requiring 10 PMTs in coincidence, blue line shows that the total detection efficiency for simulated neutrons is $\epsilon = 0.87$. Figure (5.27) reports the energy deposited in water: blue line represents the energy of all events and the red dotted one is the energy tagged with 10 PMTs in coincidence. Here are evident the two peaks corresponding to the capture of neutrons on protons (around 2 MeV) and on Gd nuclei (around 8 MeV). Figure (5.28) shows instead the tagging efficiency as a function of the deposited energy in water. Figure (5.29) and Figure (5.30) represents, respectively, the distribution of the total number of detected photoelectrons over the total number of PMTs and the distribution of detected photoelectrons in each PMT. Also for neutrons we performed a separate analysis on nVeto and mVeto detectors, always considering events generated isotropically in both volumes without any distinction obtaining the results showed in in Figures (5.31) and (5.32): red lines represent the contribution to the detection efficiency of events generated outside the detector to which we are referring, while blue ones are the contribution to the detection efficiency of events generated in the detector itself. Green lines show the sum of the two contribution, so the total efficiency in both cases. Considering now the detection efficiency of nVeto and mVeto for events generated only in their

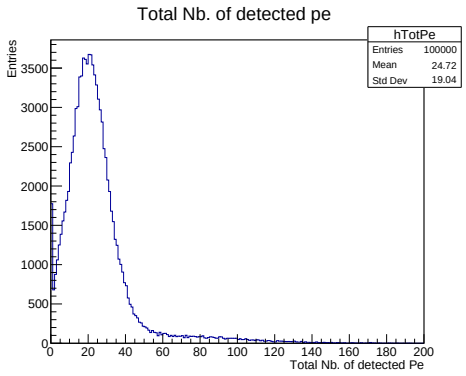

Figure 5.29: Distribution of the total number of detected photoelectrons over the total number of PMTs.

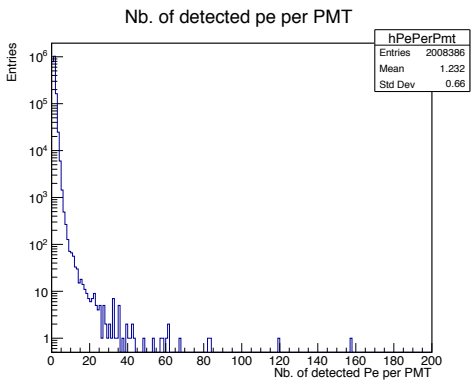

Figure 5.30: Distribution of detected photoelectrons in each PMT.

respective volumes, we obtain the results of Figures (5.33) and (5.34). Requiring 10 PMTs in coincidence, the detection efficiency of nVeto is $\epsilon = 0.94$ while that of mVeto is $\epsilon = 0.85$. Green lines of Figure (5.35) and Figure (5.36) show, respectively, the distribution of the total number of photoelectrons in nVeto and mVeto. Here, red lines represent the contribution due to neutrons generated in nVeto, while blue lines the one due to neutrons generated in mVeto. As we expect, most of the light is produced by neutrons generated in the detector we are considering. Figures (5.37) and (5.38) show, respectively, the distribution of detected photoelectrons in each PMT of nVeto and mVeto.

In conclusion, we demonstrated that a high detection efficiency can be obtained for both the products of IBD interactions of SN neutrinos. The combined detection of positrons and neutrons, inside the few seconds window typical of SN neutrino emission, allows XENONnT to be sensitive to this very rare and precious signal.

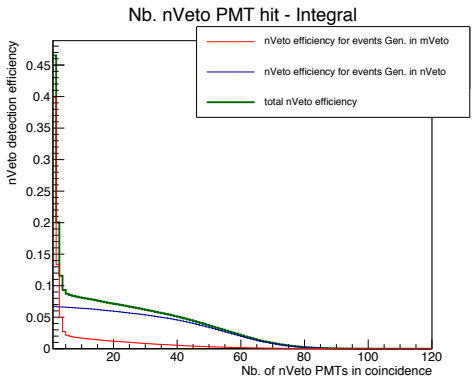

Figure 5.31: Detection efficiency of nVeto detector as a function of the number of PMTs required in coincidence for 1 keV neutrons. Red line shows the contribution to the nVeto detection efficiency of events generated in mVeto, blue one the contribution of events generated in nVeto. Green line is the sum of the two contributions.

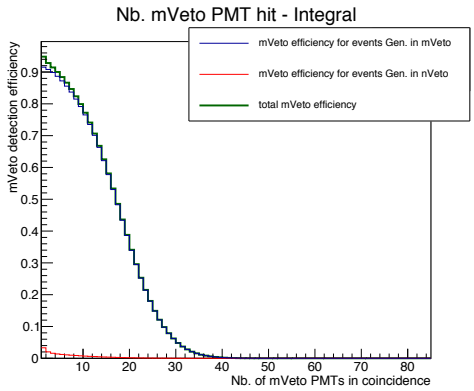

Figure 5.32: Detection efficiency of mVeto detector as a function of the number of PMTs required in coincidence for 1 keV neutrons. Red line shows the contribution to the mVeto detection efficiency of events generated in nVeto, blue one the contribution of events generated in mVeto. Green line is the sum of the two contributions.

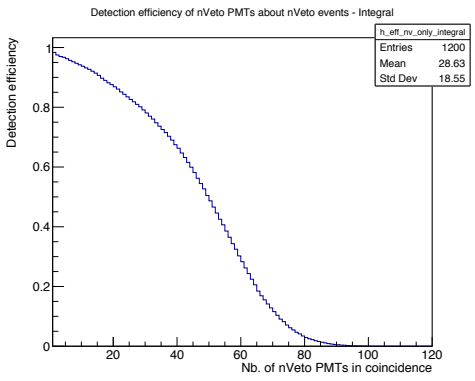

Figure 5.33: Detection efficiency of nVeto detector as a function of the number of PMTs required in coincidence only for 1 keV neutrons generated in the nVeto itself.

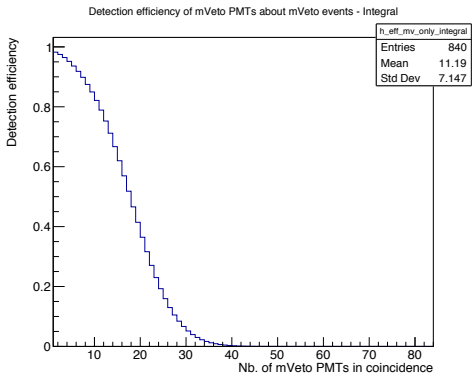

Figure 5.34: Detection efficiency of mVeto detector as a function of the number of PMTs required in coincidence only for 1 keV neutrons generated in the mVeto itself.

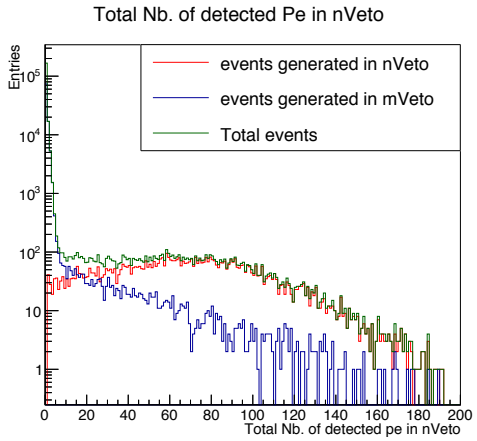

Figure 5.35: Distribution of the total number of detected photoelectrons in nVeto. Red line shows the contribution of neutrons generated inside the nVeto while the blue one shows that of neutrons generated inside the mVeto. Green line is the sum of two contributions.

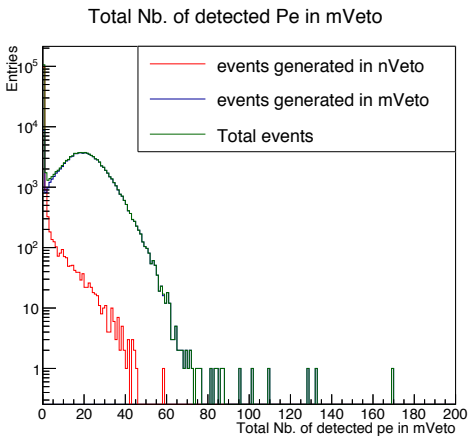

Figure 5.36: Distribution of the total number of detected photoelectrons in mVeto. Red line shows the contribution of neutrons generated inside the nVeto while the blue one shows that of neutrons generated inside the mVeto. Green line is the sum of two contributions.

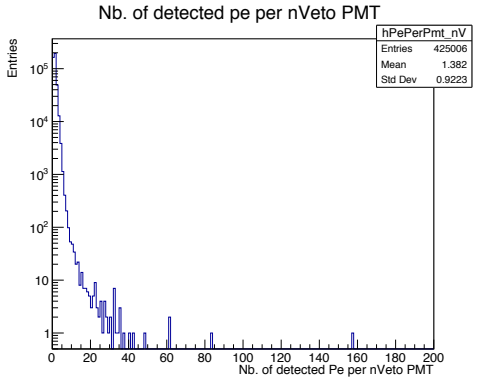

Figure 5.37: Distribution of detected photoelectrons in each PMT of nVeto.

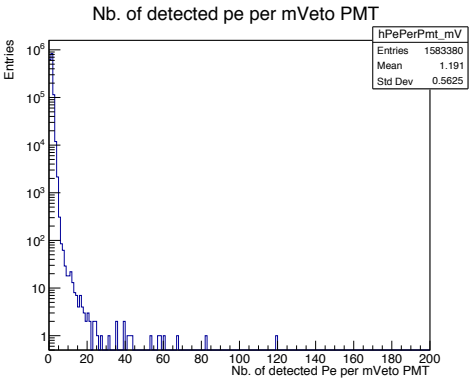

Figure 5.38: Distribution of detected photoelectrons in each PMT of mVeto.

Chapter 6

Neutrinoless double beta decay search with XENONnT

Misura ciò che è misurabile e rendi
misurabile ciò che non lo è.

Galileo Galilei

6.1 Neutrinoless double beta decay

Experiments searching for neutrinoless double beta decay are considered as the most promising way to determine if neutrinos are Majorana fermions. In order to introduce $0\nu\beta\beta$, we first consider the so called two neutrinos double beta decay which first suggested by M. Goeppert-Mayer in 1935 [59]. $2\nu\beta\beta$ is a very rare process which arises at the second order in the weak interactions, corresponding to the simultaneous decay of two neutrons in a nucleus:

$$(A, Z) \longrightarrow (A, Z+2) + 2e^{-} + 2\overline{\nu}_e \,.$$

Since the $2\nu\beta\beta$ have a four body leptonic final state, the sum of the kinetic energies of the two decay electrons have a continuous spectrum from zero to the Q-value of the decay process, defined as

$$Q_{\beta\beta} = M_i - M_f - 2m_e \,; \tag{6.1}$$

where M_i and M_f are the masses of the initial and final nuclei and m_e is the electron mass. This transition is strongly suppressed and observable only for isotopes where the single beta decay is forbidden. Despite its rarity, today it was observed for 11 nuclei with typical half-lives ranging from 10^{18} to 10^{24} years.

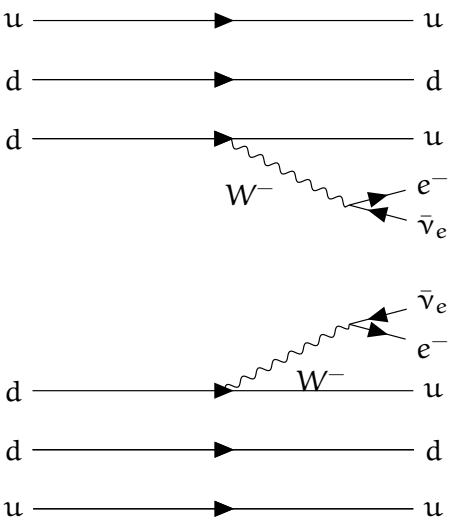

Figure 6.1: Feynman diagram of $2\nu\beta\beta$.

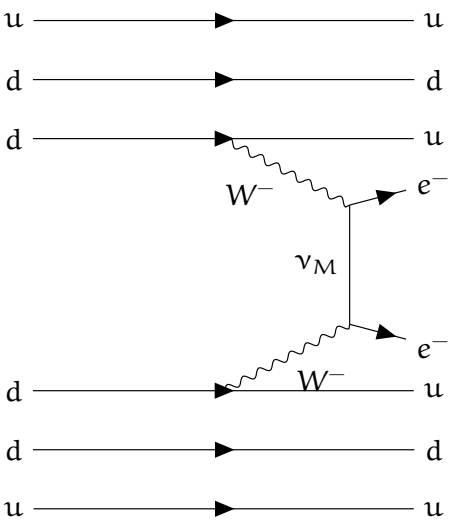

Figure 6.2: Feynman diagram of $0\nu\beta\beta$.

Neutrinoless double beta decay, proposed by Furry in 1939 [60], is a nuclear process in which two neutrons in a nucleus simultaneously decay into protons with no neutrino emission:

$$(A, Z) \longrightarrow (A, Z+2) + 2e^{-}\,.$$

The signature of this transition is a monoenergetic peak at $Q_{\beta\beta}$ of $2\nu\beta\beta$. A nucleus which can decay through a $2\nu\beta\beta$ can also decay through a $0\nu\beta\beta$, albeit with a different lifetime. Figures (6.1) and (6.2) show, respectively, the Feynman diagrams of $2\nu\beta\beta$ and $0\nu\beta\beta$: in the latter ν_M indicates the Majorana neutrinos exchanged. Their different signatures are shown in Figure (6.3).
The most evident feature of the $0\nu\beta\beta$ is the explicit violation of the leptonic number: the prized observation of this decay would therefore demonstrate that lepton number is not a symmetry of nature. So far, no elementary process where the number of total leptons varies has been observed. This suggests the hypothesis that the total lepton number follows a conservation law and is considered a global symmetry of the Standard Model. This is sufficient to forbid $0\nu\beta\beta$ transition in the Standard Model. However, we do not have any deep justification for which this law should be exact. In fact, it is possible to suspect that its validity is just approximate or circumstantial. This fact would support the theoretical picture that leptons played an important role in the creation of the matter-antimatter asymmetry in the Universe. $0\nu\beta\beta$ is also a key tool for studying neutrinos, probing if their nature is the one of Majorana fermions and providing us with precious informations on the neutrino mass scale and ordering: since the discovery of neutrino oscillations and neutrino mass furnished the

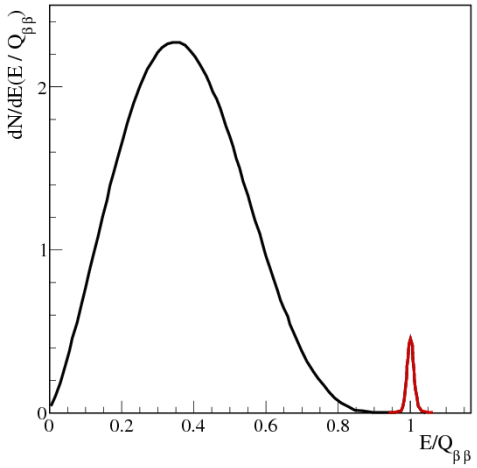

Figure 6.3: Different signatures of $2\nu\beta\beta$ (black line) and $0\nu\beta\beta$ decays (red line).

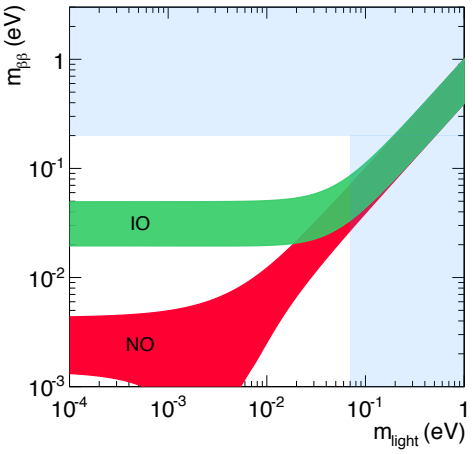

Figure 6.4: The effective Majorana mass ($m_{\beta\beta}$) as a function of the lightest neutrino mass (m_{light}). The green band corresponds to the inverted ordering of neutrino mass wile the red one to the normal ordering.

first evidence of physics beyond the Standard Model, an hypothetical evidence for such a transition would enforces this idea. Therefore, the question of how modify the Standard Model would become of central importance. The observable of $0\nu\beta\beta$ is its half-life $T^{0\nu}_{1/2}$, which theoretical expression can be factorized as

$$\left(T^{0\nu}_{1/2}\right)^{-1} = G^{0\nu}(Q_{\beta\beta}, Z)\left|M^{0\nu}\right|^2\left(\frac{m_{\beta\beta}}{m_e}\right)^2; \tag{6.2}$$

where $G^{0\nu}(Q_{\beta\beta}, Z)$ is the phase space factor, $\left|M^{0\nu}\right|$ is the nuclear matrix element and $m_{\beta\beta}$ is called the *effective Majorana mass* that rules the transition and is defined as

$$m_{\beta\beta} = \left|\sum_i = U^2_{ei} m_i\right|; \tag{6.3}$$

where the index $i = 1, 2, 3$ runs over the three light neutrinos with given mass, and U_{ei} is the matrix element of the Majorana mixing matrix of Equation (2.45). Thanks to the knowledge of the oscillation parameters, it is possible to put a series of constraints on $m_{\beta\beta}$. We can derive a range of its possible values as a function of the lightest neutrino mass [61, 62]. This relationship is shown in Figure (6.4): green band corresponds to the inverted ordering of neutrino masses, for which $m_{light} = m_3$, while the red one corresponds to the normal ordering, for which $m_{light} = m_1$. The width of the two bands is due to the unknown CP

Table 6.1: $T^{0\nu}_{1/2}$ and $m_{\beta\beta}$ current limits from EXO and KamLAND-Zen experiments.

^{136}Xe	$T^{0\nu}_{1/2}$ $(10^{25}$ yr)	$m_{\beta\beta}$ (eV)
KamLAND-Zen	> 10.7	$< (0.061 \div 0.165)$
EXO	> 1.8	$< (0.15 \div 0.40)$

violation phases and to the uncertainties in the measured oscillation parameters. The upper bound on the effective Majorana mass, $m_{\beta\beta} < 0.2\,eV$, comes from cosmological bounds [63], while the one on the lightest neutrino mass, $m_{light} < 0.07\,eV$, from $0\nu\beta\beta$ constraints [64]. We have:

- $m_{\beta\beta} = [15 \div 50]$ meV if neutrino masses follow the inverted ordering;
- $m_{\beta\beta} < 5$ meV if neutrino masses follow the normal ordering.

These ranges are then converted into an expectation value for $T^{0\nu}_{1/2}$ according to Equation (6.2). The prediction of $T^{0\nu}_{1/2}$ suffers from numerous uncertainties, especially in the measurement of the nuclear matrix element: this is due to the fact that the nuclear model describing the $0\nu\beta\beta$ transition is still unknown. Theoretical calculations allow to estimate:

- $T^{0\nu}_{1/2} \sim [10^{26} \div 10^{28}]$ yr according to the inverted ordering;
- $T^{0\nu}_{1/2} > 10^{28}$ yr according to the normal ordering.

The current best limits on $0\nu\beta\beta$ come from EXO [64] and, in particular, from KamLAND-Zen [65] experiments: Table (6.1) reports the limits obtained on the measurements of $T^{0\nu}_{1/2}$ and $m_{\beta\beta}$ by both these experiments.
In XENONnT there is the possibility to study the double beta decay of the ^{136}Xe isotope:

$$^{136}\text{Xe} \longrightarrow {}^{136}\text{Ba} + 2e^- + 2\overline{\nu}_e\,,$$

with a $Q_{\beta\beta}$ of (2457.83 ± 0.37) keV and a lifetime of $T^{2\nu}_{1/2} = 2.11 \times 10^{21}$ yr [66]. It is also possible to search for neutrinoless double beta decay of the same isotope:

$$^{136}\text{Xe} \longrightarrow {}^{136}\text{Ba} + 2e^-\,.$$

6.2 Estimation of Electronic Recoil background in XENONnT

To study the sensitivity of XENONnT for neutrinoless double beta decay, we estimate the background rate induced in the detector by the radioactive contam-

inations of its materials in the region of interest (ROI) for the $0\nu\beta\beta$ search. The latter was chosen between 2.35 MeV and 2.55 MeV. The following analysis is focused only on the Cryostat and the PMTs from which we expect the major contribution in terms of ER background. We generated the decays of all the isotopes having the most relevant background contribution in the ROI. We consider as background events those releasing energy in the ROI. They are due to γ rays that reach the most internal volume of the LXe active region, called fiducial volume, producing a single Compton scatter and exiting the detector without other interactions. For this reason, we select the background events requiring a single scatter interaction in the TPC occurring in the fiducial volume. The fiducial volume is defined as a super-ellipsoid centered in the middle of the active region. Its mathematical expression is the following:

$$\left(\frac{|z_{fv}|}{z_{max}}\right)^n + \left(\frac{R^2}{R^2_{max}}\right)^n = 1\,; \tag{6.4}$$

where

$$R^2_{max} = z^2_{max}\,, \tag{6.5}$$

and, since the top of the TPC is defined with $z = 0$, the coordinate along the z axis is shifted as

$$z_{fv} = z + \frac{h_{TPC}}{2}\,, \tag{6.6}$$

with $\frac{h_{TPC}}{2} = 738.75\,mm$ is the semi height of the TPC. Changing the parameters z_{max} and n, different shapes of the fiducial volume are obtained. For XENONnT, a fiducial volume of 4 t is considered, obtained with $z_{max} = 634\,mm$ and $n = 3$: its shape is shown in Figure (6.7).

6.2.1 Radioactive contamination in Cryostat and PMTs

The radiogenic nuclides with the most relevant contribution for the ER background in the ROI are ^{60}Co, ^{232}Th and ^{238}U. We generated 10^8 decays for each radioactive isotope (j) of Cryostat and PMTs (i). By using the selection criteria described before, we obtain the number of surviving events N_{ij}. The differential rate R_{ij} is given by [28]:

$$R_{ij} = \frac{N_{ij}}{T_{ij}\, M_{fv}\, \Delta E}\,; \tag{6.7}$$

where M_{fv} is the fiducial volume, ΔE is the considered energy range and T_{ij} is the effective livetime given by

$$T_{ij} = \frac{N^{gen}_{ij}}{M_i\, A_{ij}}\,, \tag{6.8}$$

Table 6.2: Contaminations of the materials considered in the XENONnT Monte Carlo simulations.

Component	Quantity: M_i	Unit	Contamination: A_{ij} (mBq/Unit)				
			^{60}Co	^{232}Th	^{228}Th	^{238}U	^{226}Ra
Cryostat	1860.5	kg	16.30	0.18	1.84	2.58	1.73
PMTs	494	PMT		0.5	0.5	8	0.5

where N_{ij}^{gen} is the total number of generated events and M_i and A_{ij} are the masses and the specific activities reported in Table (6.2). We consider the disequilibrium in the ^{238}U and ^{232}Th chains, splitting them into two parts:

- $^{238}\text{U} \longrightarrow {}^{230}\text{Th}$ and $^{226}\text{Ra} \longrightarrow {}^{206}\text{Pb}$;
- $^{232}\text{Th} \longrightarrow {}^{228}\text{Ac}$ and $^{228}\text{Th} \longrightarrow {}^{208}\text{Pb}$.

The main exception is the first part of the ^{238}U chain, where very few and low energy gammas are emitted. So the contaminations we used in the estimation of ER background come from the second part of ^{238}U chain and from both the parts of ^{232}Th chain. The results of this background rate estimate are shown in Figures (6.5) and (6.6): the first one shows, as a function of the energy, the separate contributions from the various components to the total ER background rate considering only single scatter events in the 4 t fiducial volume, while in the second one the total contributions of Cryostat and PMTs are shown separately. In both, the pink line represents the total contributions of all components. From this results is evident that the highest contribution of the total ER background comes from the Cryostat, mainly from its ^{60}Co contamination. All the contributions of Cryostat and PMTs components are reported in Table (6.3). From

Table 6.3: Different contributions to the total ER background of different components.

Component (i)	Isotope (j)	% over the total	% over the i total
Cryostat (99.4%)	^{60}Co	88.65	89.17
	^{232}Th	4.08	4.11
	^{238}U	6.67	6.71
PMTs (0.6%)	^{232}Th	0.29	50.64
	^{238}U	0.29	49.36

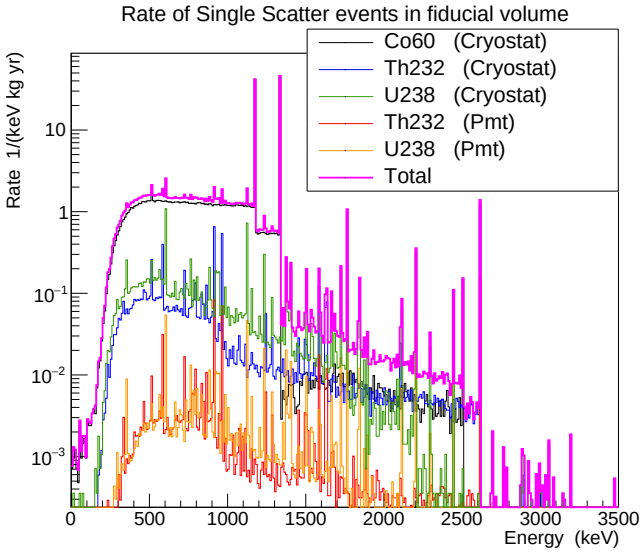

Figure 6.5: Separate contributions to the total ER background rate coming from all different isotopes considered. Different colors corresponds to different contributions: black, green and blue lines correspond, respectively, to the ^{60}Co, ^{238}U and ^{232}Th from the Cryostat, while orange and red ones to the ^{238}U and ^{232}Th from the PMTs. Pink line is the sum of all contributions.

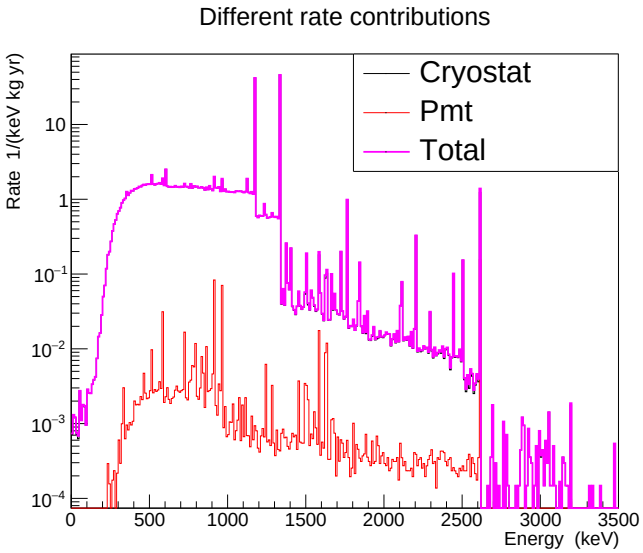

Figure 6.6: Contributions to the total ER background rate from Cryostat (blue line) and PMTs (red line). Pink line is the sum of all contributions.

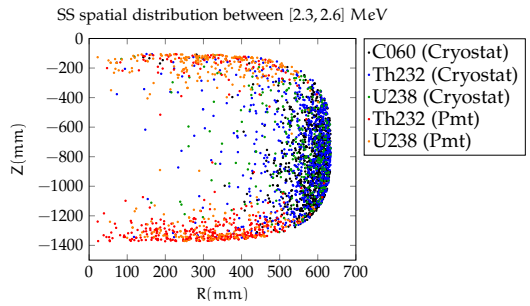

Figure 6.7: Spatial distribution of single scatter events with energy between $[2.3, 2.6]$ MeV inside the 4 t fiducial volume.

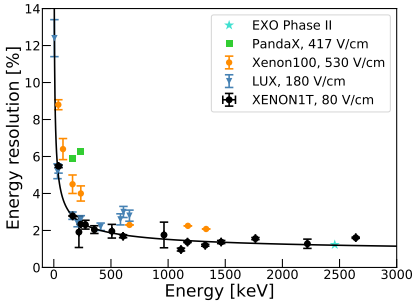

Figure 6.8: Energy resolution for different γ-lines in the XENON1T detector compared to other double-phase XeTPC experiments. The solid line is the best fit for the dependence in Equation (6.9) with parameters given by Equations (6.10a) and (6.10b).

this study, the ER background rate in the ROI is of the order of 2×10^{-2} events $[\,\mathrm{kg} \cdot \mathrm{keV} \cdot \mathrm{yr}]^{-1}$. The spatial distribution of simulated single scatter events occurring in the 4 t fiducial volume in $[2.3, 2.6]$ MeV is shown in Figure (6.7).

6.2.2 Energy resolution of XENONnT

Due to the finite energy resolution of any detector, the monoenergetic signals do not appear as sharp lines but follow a normal distribution whose width, divided by its mean value, the central energy, is the resolution. Spectra in Figures (6.5) and (6.6) and the monoenergetic peak at $Q_{\beta\beta}$ of $0\nu\beta\beta$ signal must be smeared based on the energy resolution measured from the peaks of the real background data. The analytical expression of the energy resolution is given by

$$\frac{\sigma_E}{E} = \frac{a}{\sqrt{E}} + b\,; \tag{6.9}$$

where E is the energy of each monoenergetic peak and a and b are the resolution parameters. For the XENON1T experiment, we obtain from the fit in Figure (6.8):

$$a = (30.98 \pm 0.43)\,\sqrt{\mathrm{keV}}\,; \tag{6.10a}$$

$$b = (0.37 \pm 0.03)\,. \tag{6.10b}$$

Applying now this energy resolution to the background spectra of Figure (6.5), we obtain Figure (6.9). At the $Q_{\beta\beta}$, we have an energy resolution of about 1%. The zoom of the smeared spectra in the ROI is reported in Figure (6.10), where the shaded area represents the $0\nu\beta\beta$ signal region around $Q_{\beta\beta}$.

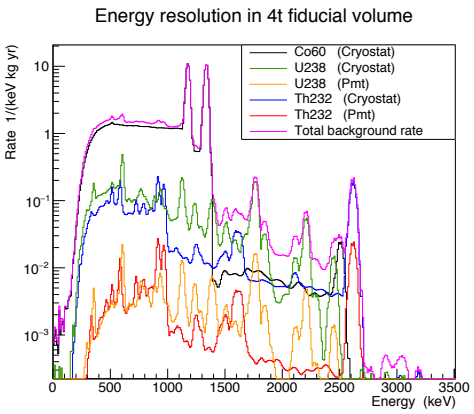

Figure 6.9: Smearing of all contributions to the total ER background rate in 4 t fiducial volume.

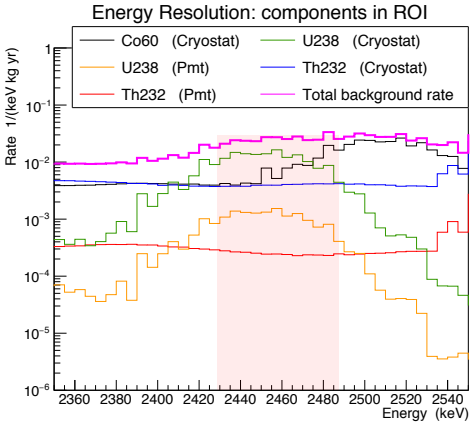

Figure 6.10: Smearing of all contributions to the total ER background rate in the ROI. The shaded area represents the $0\nu\beta\beta$ signal region around $Q_{\beta\beta}$.

6.3 Sensitivity for neutrinoless double beta decay in XENONnT

As a starting point, we calculated the expected sensitivity for neutrinoless double beta decay in XENONnT using the current background rate and energy resolution. Experimental sensitivity, defined as the 90% CL upper limit, is [67]

$$S^{0\nu} = \frac{\ln 2}{1.64}\,\epsilon\,\frac{ia}{A}\sqrt{\frac{M_{fv}\cdot t}{\Gamma\cdot b}}\,; \tag{6.11}$$

where ϵ is the efficiency, ia the isotopic abundance of the used isotope, A its atomic mass number, M_{fv} the fiducial mass, t the livetime, b the background rate in the ROI and Γ is the full width at half maximum, defined as

$$\Gamma = \sigma_E \cdot 2.355\,; \tag{6.12}$$

where σ_E is the energy resolution at $Q_{\beta\beta}$. For this analysis we adopt the following numeric values:

- an efficiency $\epsilon = 1$;
- using the ^{136}Xe isotope, its atomic mass number is $A = 135.91\,\text{uma} = 2.25\times10^{-25}$ kg and its isotopic abundance is $ia = 8.9\%$;
- a fiducial mass of 4 t;
- an energy resolution $\sigma_E = 25\,keV$, so $\Gamma = 58.9\,keV$;

- the background rate in the ROI is 2×10^{-2} events $[\,\mathrm{kg} \cdot \mathrm{keV} \cdot \mathrm{yr}]^{-1}$.

With these numbers, the sensitivity as a function of the livetime is reported in Figure (6.11): after one year, with a fiducial volume of 4 t, XENONnT will reach a sensitivity of 9.67×10^{24} yr. To improve the sensitivity we can use a different fiducial volume, by varying the super-ellipsoid parameter z_{max}. We can estimate the best one for the $0\nu\beta\beta$ search considering that in a smaller volume there is a smaller amount of the double beta emitter, but also a reduced ER background. In Figure (6.12) we describe the dependence of the total background rate in the ROI by varying the fiducial mass. The sensitivity parameter is defined, following Equation (6.11), as the fiducial mass over the square root of background counts $B = b \cdot \Delta E \cdot M_{fv} \cdot t$ in the ROI, $\frac{M_{fv}}{\sqrt{B}}$, and its dependency on the chosen fiducial mass is reported in Figure (6.13). The analysis shows that the fiducial mass which maximizes the sensitivity parameter for the $0\nu\beta\beta$ search is the 1.6 t super-ellipsoid volume.
We can now consider the 1.6 t fiducial volume, whose smeared spectra of all contributions to the ER background rate are reported in Figure (6.14). In the ROI, the total ER background rate is about 2.14×10^{-3} events $[\,\mathrm{kg} \cdot \mathrm{keV} \cdot \mathrm{yr}]^{-1}$ and the spectra of all components are given by Figure (6.15). Repeating, in this case, the estimation of sensitivity in Equation (6.11), its dependency on lifetime is shown in Figure (6.16): after one year, with 1.6 t fiducial volume, XENONnT will reach a sensitivity of 1.87×10^{25} yr.

6.4 Expected number of neutrinoless double beta decays

The expected number of $0\nu\beta\beta$ decays is given by [68]

$$N = \ln 2 \, \frac{\epsilon \cdot m \cdot N_A}{W} \, \frac{t}{T^{0\nu}_{1/2}} \, ; \tag{6.13}$$

where ϵ is the detection efficiency, m is the mass of the $\beta\beta$ emitting isotope, W is its molar mass, N_A is the Avogadro constant, t is the observation time and $T^{0\nu}_{1/2}$ is the half-life of the decay. The xenon molar mass is $W = 131.29 \times 10^{-3}$ kg mol^{-1}.

6.4.1 Signal events in 4 t fiducial volume

Considering the isotopic abundance of ^{136}Xe isotope, its mass, contained in the 4 t fiducial volume, is $m = 356$ kg. Assuming an efficiency of $\epsilon = 1$, a time of $t = 1$ yr and an half-life equal to the value obtained by Figure (6.11) for XENONnT after one year of activity, we estimate about $N = 116.5$ events of $0\nu\beta\beta$

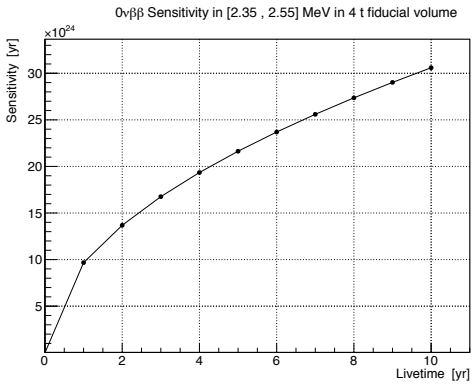

Figure 6.11: Sensitivity to neutrinoless double beta decay of XENONnT as a function of the livetime, considering a fiducial volume of 4 t. After 1 yr, XENONnT will reach a sensitivity of 9.67×10^{24} yr.

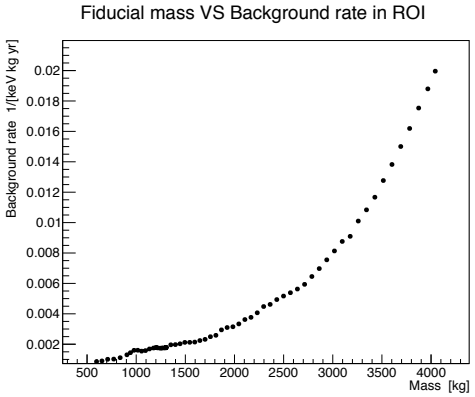

Figure 6.12: Dependence of the background rate of single scatter events in the ROI on the different fiducial mass chosen.

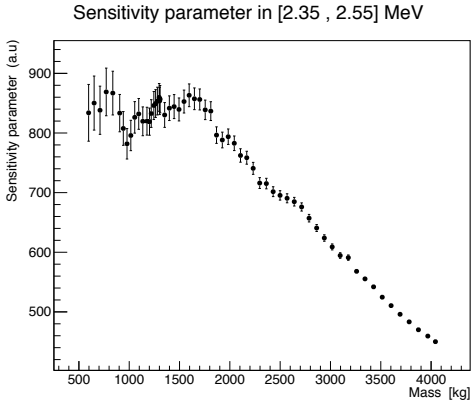

Figure 6.13: Sensitivity dependency on the fiducial mass in the super-ellipsoid fiducial volume for single scatter events in the ROI. The best fiducial mass for the neutrinoless double beta decay study is given by 1.6 t super-ellipsoid volume.

decays. Adding the peak due to the $0\nu\beta\beta$ signal and applying the smearing to it and to the total background spectrum, we obtain the spectra of Figure (6.17).

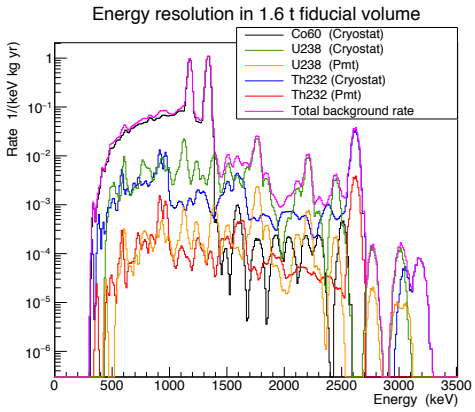

Figure 6.14: Smearing of all contributions to the total ER background rate in 1.6 t fiducial volume.

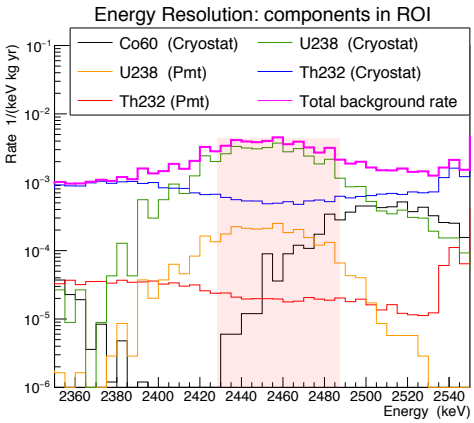

Figure 6.15: Smearing of all contributions to the total ER background rate in the ROI, with 1.6 t fiducial volume. The shaded area represents the $0\nu\beta\beta$ signal region around $Q_{\beta\beta}$.

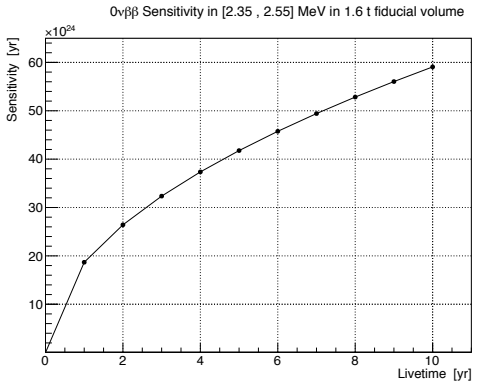

Figure 6.16: Sensitivity to neutrinoless double beta decay of XENONnT as a function of the livetime, considering a fiducial volume of 1.6 t. After 1 yr, XENONnT will reach a sensitivity of 1.87×10^{25} yr.

The rate of $0\nu\beta\beta$ is about 2.9×10^{-2} events $[\mathrm{kg} \cdot \mathrm{keV} \cdot \mathrm{yr}]^{-1}$. After five years of XENONnT activity, with a fiducial mass of 4 t, we will achieve a sensitivity of 2.16×10^{25} yr.

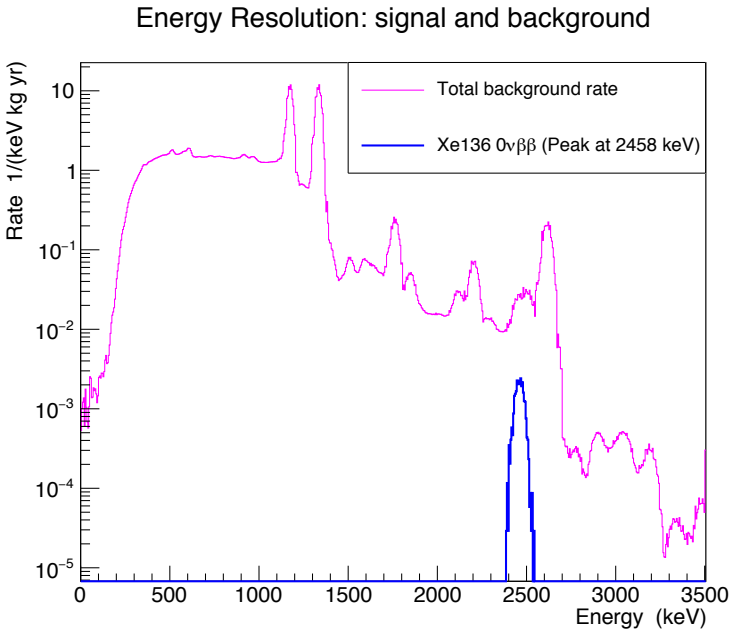

Figure 6.17: Comparison between the smeared spectrum of the total ER background rate (pink line) and the one of the $0\nu\beta\beta$ signal (blue line) in 4 t fiducial volume.

6.4.2 Signal events in 1.6 t fiducial volume

Considering now the ^{136}Xe isotope contained in the 1.6 t fiducial volume, its mass is $m = 142\,kg$. Assuming again an efficiency of $\epsilon = 1$, a time of $t = 1\,yr$ and an half-life equal to the value obtained by Figure (6.16) for XENONnT after one year of activity, we estimate about $N = 24.04$ events of $0\nu\beta\beta$ decays. Performing the same study previously done, adding the peak due to the $0\nu\beta\beta$ signal, applying the smearing to it and to the total background spectrum, we obtain the spectra of Figure (6.18). The rate of $0\nu\beta\beta$ is about 1.5×10^{-2} events $[kg \cdot keV \cdot yr]^{-1}$. In this case, considering the sum of signal and background contributions, and comparing this one with the total background rate, we obtained the results in Figures (6.19) and (6.20): assuming the 1.6 t fiducial volume, after one year, the signal peak would become visible. After five years of XENONnT activity, with a fiducial mass of 1.6 t, we will achieve a sensitivity of 4.18×10^{25} yr.

With this study we demonstrated that, after five year of activity, XENONnT will achieve sensitivity value comparable with the current limit of EXO reported in Table (6.1).

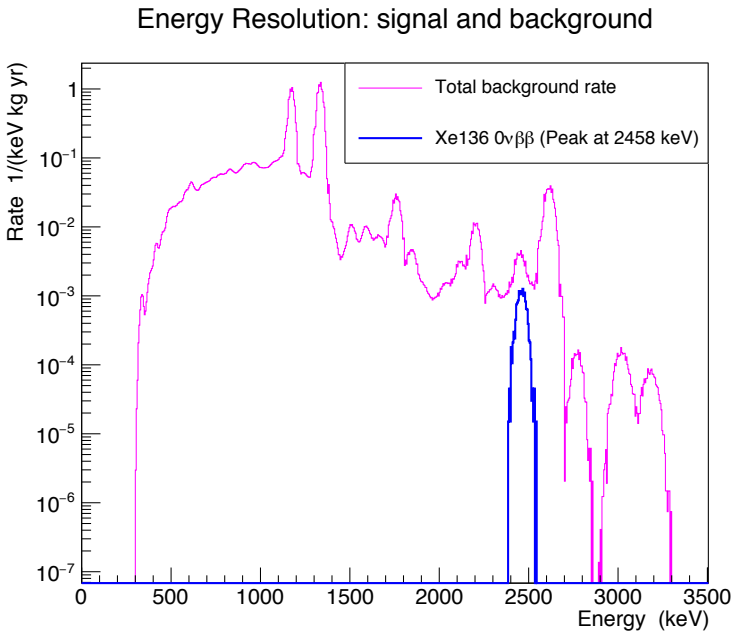

Figure 6.18: Comparison between the smeared spectrum of the total ER background rate (pink line) and the one of the $0\nu\beta\beta$ signal (blue line) in 1.6 t fiducial volume.

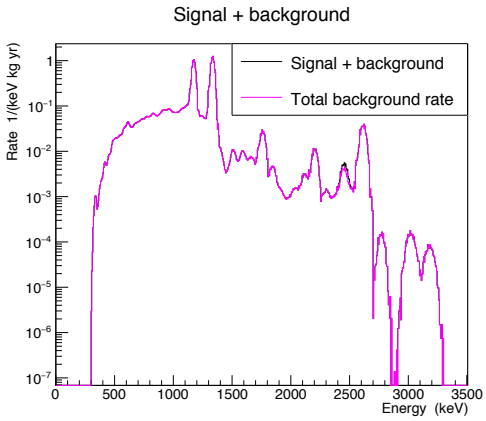

Figure 6.19: Comparison between pink line, which represents the total contribution of ER background rate in 1.6 t fiducial volume, and black one, which is the sum of both contribution of signal and background of Figure (6.18).

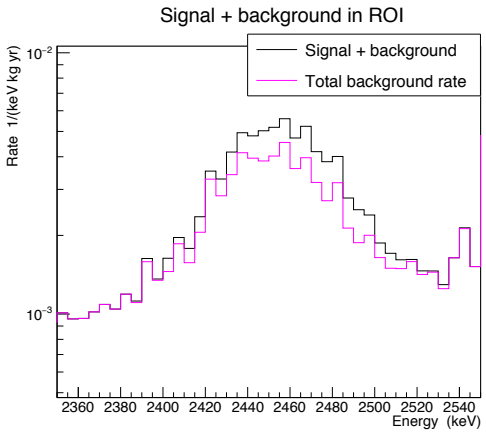

Figure 6.20: Comparison between the total contribution of ER background rate in 1.6 t fiducial volume (pink line) and the sum of both signal and background (black line) in the ROI.

Conclusions

The new phase of the XENON Dark Matter Project, XENONnT, hosted in the underground *Laboratori Nazionali del Gran Sasso*, consists on a double-phase XeTPC containing 5.9 t of active Xe target, instrumented with 494 PMTs and hosted inside a Cryostat. This latter is also contained into a tank filled with Gd-doped water at 0.2% mass concentration, which acts as an additional shield against cosmic rays flux. The presence of gadolinium improves the neutron capture efficiency and the ability to discriminate the events of nuclear recoil background that mimic the signature of the WIMPs interactions, allowing to reach lower NR background level in the TPC. The muon Veto and the new neutron Veto structures, placed near the inner walls of the water tank and around the Cryostat and equipped with 84 and 120 PMTs respectively, allow a further reduction of the environmental background rate in the TPC. The XENONnT experiment will be sensitive to SI WIMP-nucleon cross section down 10^{-48} cm^2.
Even if XENONnT is an experiment to directly search Dark Matter particles, this thesis work shows how it can be used also to study other interesting and still unknown particles: neutrinos. In fact, thanks to the big dimensions reached by this detector, it can be able to detect also all flavors neutrinos coming from Supernova explosions through their coherent elastic scatters on Xe nuclei in the TPC. But this is not the only channel through which XENONnT can detect SN neutrinos. In fact, thanks to the water tank surrounding the TPC, the inverse beta decay interactions of electron antineutrinos on water protons can be detected. Using the XENONnT GEANT4 code to perform simulations of positrons and neutrons of given spectra, generated after the neutrino interaction in water, we studied the detection efficiencies of muon and neutron Vetoes about these events. Supposing the signal detected by 10 PMTs in coincidence, both the Veto systems measured a positrons detection efficiency of the 99% while the neutron ones, thanks to the presence of gadolinium, are about 85% for the muon Veto and 94% for the neutron Veto: we demonstrated that a high detection efficiency can be obtained by XENONnT for both the products of IBD interactions of SN neutrinos.
XENONnT can be also used to study other aspects of neutrino physics. Today, we know that the Standard Model can not provide a correct description of

this particle: starting from the phenomenon of the oscillations of neutrino flavor, which implies that neutrino has a non zero mass, and continuing with the uncertain nature and unknown value of this one, we need another model to describe this particle with all its properties. The most promising way to determine the nature of neutrinos as Dirac or Majorana fermions, and so the mechanism that gives them mass, is the search for the Standard Model forbidden neutrinoless double beta decay. The observation of this nuclear transition would prove the Majorana nature of neutrinos and the fact that lepton number is not a global symmetry of the Standard Model, pointing out the existence of new physics beyond the known one. In XENONnT there is the possibility to search for the neutrinoless double beta decay of the ^{136}Xe isotope: its expected signature is a monoenergetic peak at 2458 keV. Due to the rarity of this process we have to pay attention to some features of the detector, such as the background suppression and its energy resolution. Taking into account all the radiogenic nuclides which have the most relevant contribution for the electronic recoil background in the region of interest for the $0\nu\beta\beta$ search, defined between $[2.35, 2.55]$ MeV, and applying the cut selection of single scatter interactions in the 4 t fiducial volume of XENONnT, we obtain a background rate of about 2×10^{-2} events $[kg \cdot keV \cdot yr]^{-1}$. The sensitivity of XENONnT for neutrinoless double beta decay in the 4 t fiducial volume is shown in Figure (6.11): after one year of livetime, XENONnT will reach a sensitivity of about 9.67×10^{24} yr. We can see further that the 4 t fiducial mass is not the one that maximizes the sensitivity parameter: varying the value of fiducial mass used, we can estimate that the value of this one that maximizes the sensitivity parameter, is about 1.6 t contained in the super-ellipsoid volume. Assuming this best fiducial mass value and performing the same study on sensitivity, we obtain the result reported in Figure (6.16): after one year of livetime, XENONnT will reach a sensitivity of about 1.87×10^{25}. After five years, we will achieve a sensitivity of 4.18×10^{25} yr, comparable with the current limit of EXO reported in Table (6.1). In the search for rare events as neutrinoless double beta decay, a detector as DARWIN, containing a ^{136}Xe isotope target of more than 3.5 t without isotopic enrichment, can be used to perform a search for this decay in an ultra-low background environment, with a sensitivity that will be comparable to other future ton-scale experiments, allowing to explore a region of parameters not yet observed.

Even if the main purpose of dual-phase detectors as XENONnT and DARWIN is the discovery of Dark Matter particles, they can be used also to carry on studies on different aspects of physics, like the neutrino one and the observation of rare events. Thanks to the big target masses used and low background levels achieved, these experiments can get important results, useful to clarify aspects still unknown in physics.

Appendix A

Notations and conventions

Here, the main notations and conventions used in this work are shown.

Metric tensor

We used the *West Coast* or *mostly minus* convention for the metric tensor:

$$g_{\mu\nu} = \begin{cases} 0 & \text{for} \quad \mu \neq \nu\,, \\ 1 & \text{for} \quad \mu = \nu = 0\,, \\ -1 & \text{for} \quad \mu = \nu = 1,2,3\,. \end{cases} \tag{A.1}$$

Pauli's matrices

The Pauli spin matrices τ_k, with $k = 1,2,3$, are hermitean 2×2 matrices defined as:

$$\tau_1 = \begin{pmatrix} 0 & 1 \\ 1 & 0 \end{pmatrix} \qquad \tau_2 = \begin{pmatrix} 0 & -i \\ i & 0 \end{pmatrix} \qquad \tau_3 = \begin{pmatrix} 1 & 0 \\ 0 & -1 \end{pmatrix}. \tag{A.2}$$

Dirac's matrices

We define the Dirac's γ^μ matrices as the 4×4 matrices:

$$\gamma^0 = \begin{pmatrix} 0 & \mathbb{I} \\ \mathbb{I} & 0 \end{pmatrix} \qquad \gamma^k = \begin{pmatrix} 0 & \tau_k \\ -\tau_k & 0 \end{pmatrix} \qquad k = 1,2,3\,, \tag{A.3}$$

where τ_k are the Pauli's matrices (A.2) and $\mathbb{I}$ is the 2×2 identity. The γ^μ matrices respond to the following anti-commutation relations, called *Clifford's algebra*:

$$\{\gamma^\mu, \gamma^\nu\} = 2g^{\mu\nu}\mathbb{I}\,; \tag{A.4}$$

and have the hermitean property:

$$\gamma^{\mu\dagger} = \gamma^0\gamma^\mu\gamma^0 \,. \tag{A.5}$$

The chirality matrix γ_5 is the hermitean 4×4 matrix defined as:

$$\gamma_5 = \gamma^5 = -i\gamma^0\gamma^1\gamma^2\gamma^3 = \begin{pmatrix} \mathbb{I} & 0 \\ 0 & -\mathbb{I} \end{pmatrix}, \tag{A.6}$$

which satisfies the property:

$$\{\gamma^\mu, \gamma^5\} = 0 \,. \tag{A.7}$$

Spinor field

The lagrangian of a Dirac spinor field ψ with mass m is:

$$\mathcal{L}_D = \overline{\psi}(i\gamma^\mu\partial_\mu - m)\psi \,. \tag{A.8}$$

where the Dirac conjugate spinor $\overline{\psi}$ is defined as:

$$\overline{\psi} = \psi^\dagger\gamma^0 \,. \tag{A.9}$$

A Dirac spinor can be written as a complex 4-components vector, made of the 2-components spinors ψ_L^w, ψ_R^w, called Weyl's spinors:

$$\psi = \begin{pmatrix} \psi_R^w \\ \psi_L^w \end{pmatrix} = \begin{pmatrix} \psi_{R1}^w \\ \psi_{R2}^w \\ \psi_{L1}^w \\ \psi_{L2}^w \end{pmatrix}, \tag{A.10}$$

The left and right Dirac's components can be identified using the two chirality projectors P_L and P_R defined as

$$P_L = \frac{1-\gamma_5}{2} = \begin{pmatrix} 0 & 0 \\ 0 & \mathbb{I} \end{pmatrix}; \tag{A.11a}$$

$$P_R = \frac{1+\gamma_5}{2} = \begin{pmatrix} \mathbb{I} & 0 \\ 0 & 0 \end{pmatrix}, \tag{A.11b}$$

which satisfy the following properties:

$$P_j^2 = P_j = P_j^\dagger \,; \qquad j = L, R \tag{A.12a}$$

$$P_L P_R = P_R P_L = 0 \,; \tag{A.12b}$$

$$P_L + P_R = 1 \,. \tag{A.12c}$$

The action of the projectors on a Dirac spinor makes it possible to extract its respective chiral component:

$$\psi_L = P_L\psi = \begin{pmatrix} 0 & 0 \\ 0 & \mathbb{I} \end{pmatrix}\begin{pmatrix} \psi_R^w \\ \psi_L^w \end{pmatrix} = \begin{pmatrix} 0 \\ \psi_L^w \end{pmatrix}, \tag{A.13a}$$

$$\psi_R = P_R\psi = \begin{pmatrix} \mathbb{I} & 0 \\ 0 & 0 \end{pmatrix}\begin{pmatrix} \psi_R^w \\ \psi_L^w \end{pmatrix} = \begin{pmatrix} \psi_R^w \\ 0 \end{pmatrix}; \tag{A.13b}$$

$$\overline{\psi}_L = \overline{\psi}P_R = \overline{\psi}\left(\frac{1+\gamma_5}{2}\right); \tag{A.13c}$$

$$\overline{\psi}_R = \overline{\psi}P_L = \overline{\psi}\left(\frac{1-\gamma_5}{2}\right). \tag{A.13d}$$

Covariant derivative

The gauge covariant derivative is defined as:

$$\mathcal{D}_\mu = \partial_\mu - igT^a A_\mu^a, \tag{A.14}$$

where g is the charge related to the gauge group considered. Their generators are T^a, while A_μ^a is the set of gauge fields. In the case of QED, we have a simpler definition, given that the gauge group is abelian:

$$\mathcal{D}_\mu = \partial_\mu - i\,Qe\,A_\mu. \tag{A.15}$$

The charge g becomes Qe, where e is the strength of the electromagnetic force, while Q is the electric charge of a particle (in e units). The electron is defined as having $Q_e = -1$.

Appendix A. Notations and conventions

Appendix B

Majorana theory

Chiral spinors ψ_L and ψ_R are the smallest irreducible representations of the Lorentz group, from which all representations can be constructed. Starting from the Dirac lagrangian

$$\mathcal{L}_D = \overline{\psi}\left(\frac{i}{2}\gamma^\mu \overleftrightarrow{\partial_\mu} - m\right)\psi\,, \tag{B.1}$$

applying the Euler-Lagrange field equation,

$$\partial_\mu \frac{\delta \mathcal{L}_D}{\delta(\partial\overline{\psi})} = \frac{\delta \mathcal{L}_D}{\delta\overline{\psi}}\,, \tag{B.2}$$

we obtain the Dirac equation for the fermion field $\psi = \psi_L + \psi_R$:

$$(i\gamma^\mu\partial_\mu - m)\psi = 0\,. \tag{B.3}$$

It can be shown that, writing the lagrangian (B.1) in terms of ψ_L and ψ_R, the Dirac Equation (B.3) is equivalent to the coupled equations for the chiral fields ψ_L and ψ_R:

$$i\gamma^\mu\partial_\mu\psi_L = m\psi_R\,; \tag{B.4a}$$

$$i\gamma^\mu\partial_\mu\psi_R = m\psi_L\,. \tag{B.4b}$$

If a fermion is massless, the Equations (B.4) are decoupled:

$$i\gamma^\mu\partial_\mu\psi_L = 0\,; \tag{B.5a}$$

$$i\gamma^\mu\partial_\mu\psi_R = 0\,. \tag{B.5b}$$

Hence, a massless fermion can be describes by a single chiral field, left-handed or right-handed, which has only two independent components:

$$\psi_L = \begin{pmatrix} 0 \\ \chi_L \end{pmatrix} \qquad \psi_R = \begin{pmatrix} \chi_R \\ 0 \end{pmatrix}. \tag{B.6}$$

These spinors are called Weyl spinors and Equations (B.5) are called the Weyl equations.
The possibility of describing a physical particle with a Weyl spinor was rejected by Pauli in 1933, because it leads to the violation of parity. Parity transformations, in fact, transform left-handed Weyl spinor into a right-handed one and vice versa. The parity conservation requires the simultaneous existence of both chiral components. However, the discovery of parity violation in weak processes invalidated Pauli's reasoning, renewing the possibility to describe massless particles with Weyl spinor fields. Since there was no indication of the existence of a neutrino mass and it was likely that neutrino takes part in weak interactions through its left-handed chiral component, Landau, Lee and Yang and Salam proposed to describe the neutrino with a left-handed Weyl spinor ν_L. This theory is the so called *two component theory of massless neutrinos*. If a two component spinor is sufficient for the description of a massless fermion, it is natural to ask if a four component spinor is necessary to describe massive particles. The answer is no, as discover Ettore Majorana in 1937. His idea was to assume that the two chiral components ψ_L and ψ_R are not independent, in such a way as to be able to describe a massive particle using just a single left-handed field ψ_L [69]. This means that the two coupled Equations (B.4) must be two ways of writing the same equation for the one independent field ψ_L.
In order to obtain (B.4a) from (B.4b), we take the Hermitian conjugate of (B.4b), multiplying it on the right with γ^0:

$$\begin{aligned} (i\gamma^\mu \partial_\mu \psi_R)^\dagger \gamma^0 &= m\psi_L^\dagger \gamma^0 \\ -i\,\overline{\psi}_R \partial_\mu \gamma^\mu &= m\overline{\psi}_L\,. \end{aligned} \tag{B.7}$$

In order to obtain the same structure of Equation (B.4a), we take the transpose of Equation (B.7) and introduce the charge conjugation matrix $\mathcal{C}$ which satisfy the following properties:

$$\mathcal{C}^\dagger = \mathcal{C}^{-1}\,; \tag{B.8a}$$

$$\mathcal{C}^T = -\mathcal{C}\,; \tag{B.8b}$$

$$\mathcal{C}\gamma_\mu^T \mathcal{C}^{-1} = -\gamma_\mu\,; \tag{B.8c}$$

$$\mathcal{C}\gamma^{5T} \mathcal{C}^{-1} = \gamma^5\,. \tag{B.8d}$$

Multyply on the left with it:

$$\begin{aligned} -i\mathcal{C}\left(\overline{\psi}_R \partial_\mu \gamma^\mu\right)^T &= m\mathcal{C}\overline{\psi}_L^T \\ -i\mathcal{C}\gamma^{\mu T} \partial_\mu \overline{\psi}_R^T &= m\mathcal{C}\overline{\psi}_L^T\,, \end{aligned} \tag{B.9}$$

and using the property (B.8c) of the charge conjugation matrix, we obtain

$$i\gamma^\mu \partial_\mu \mathcal{C}\overline{\psi}_R^T = m\mathcal{C}\overline{\psi}_L^T\,. \tag{B.10}$$

From the comparison between Equation (B.10) and (B.4a), comes out that

$$\psi_L = \xi \mathcal{C} \overline{\psi}_R^T ; \tag{B.11a}$$

$$\psi_R = \xi \mathcal{C} \overline{\psi}_L^T . \tag{B.11b}$$

where ξ is an arbitrary phase factor which can be eliminated by rephasing the fields. These are the Majorana relations between ψ_L and ψ_R which make sense because $\mathcal{C}\overline{\psi}_L^T$ is right-handed and $\mathcal{C}\overline{\psi}_R^T$ is left-handed. So we can rewrite the Dirac Equation (B.3) only in terms of the left-handed field: we obtain the Majorana equation

$$i\gamma^\mu \partial_\mu \psi_L = m \mathcal{C} \overline{\psi}_L^T . \tag{B.12}$$

Rewriting the field ψ using the definition (B.11b)

$$\psi = \psi_L + \psi_R = \psi_L + \xi \mathcal{C} \overline{\psi}_L^T , \tag{B.13}$$

it is evident that, apart from the phase factor ξ, the term $\mathcal{C}\overline{\psi}_L^T$ is identical to the charge conjugated field ψ_L^c:

$$\mathcal{C} \overline{\psi}_L^T = \psi_L^c . \tag{B.14}$$

Taking the charge conjugated of Equation (B.13) we have:

$$\psi^c = (\psi_L + \psi_L^c)^c = \psi_L^c + \psi_L = \psi . \tag{B.15}$$

The Majorana condition in Equation (B.15) implies the equality of field and its charge conjugated: in other words, the equality between particle and its antiparticle. Hence, only neutral fermions can be described by a Majorana field.

Ringraziamenti

Tra alti e bassi, maree di difficoltà ed incertezze, ma anche mille risate, gioie e successi, questo capitolo della mia vita è giunto al termine. Voglio ringraziare le persone importanti, con le quali ho condiviso molto e che mi sono state accanto, regalandomi momenti indimenticabili ed opportunità preziose.
Inizio con il ringraziare la Professoressa Gabriella Sartorelli, che mi ha accolta con entusiasmo in un mondo a me estraneo, permettendomi di entrare in contatto con una realtà diversa, che non ero abituata a vedere.
Un grazie di cuore a Marco e Pietro, con i quali ho condiviso le mie giornate durante il periodo del lavoro di tesi: grazie per aver curato ogni singolo dettaglio del mio lavoro. Grazie per avermi insegnato che fare ricerca significa portare pazienza: significa costruire risposte, superando tutte le difficoltà del mestiere. Grazie per aver sopportato i miei momenti di crisi, per aver prestato sempre la massima attenzione ai miei dubbi e per aver dato sempre una risposta alle mie domande, per quanto banali talvolta potevano risultare.
Grazie ai miei amici, vicini e lontani: grazie per le serate in compagnia, per tutte le risate e le esperienze condivise. Grazie per aver rispettato i miei spazi ed i miei tempi, per esserci comunque stati nei momenti peggiori e per aver condiviso con me le gioie di quelli migliori.
Un grazie speciale a Daniele, che Bologna mi ha dato la fortuna di incontrare. Grazie per aver vissuto con me il meglio ed il peggio di questi anni. Grazie per la pazienza che hai riservato nei miei confronti e per il supporto e la fiducia che mi hai sempre dato. Grazie per aver diviso con me il peso di tutte le delusioni, e per aver moltiplicato la gioia di tutti i successi. Grazie per tutto.
Un grazie speciale anche a mio fratello, perché so che è quì per me: ora e per sempre. Grazie perché, nonostante le discussioni, rimani un punto fisso, senza il quale sarei persa.
Infine voglio ringraziare i miei genitori, senza i quali nulla di ciò che ho vissuto e realizzato sarebbe stato possibile. Grazie per avermi dato la possibilità di studiare lontana da casa, e per esservi fidati di me dal primo istante. Grazie per avermi sostenuta ed incoraggiata durante i primi periodi, quelli più difficili, e grazie per aver continuato a farlo ogni giorno. Grazie per aver dato forma a questo mio sogno.

Bibliography

[1] F. Englert and R. Brout. "Broken Symmetry and the Mass of Gauge Vector Mesons". *Phys. Rev. Lett.* 13 (9 Aug. 1964), pp. 321–323. DOI: 10.1103/PhysRevLett.13.321. URL: https://link.aps.org/doi/10.1103/PhysRevLett.13.321.

[2] P.W. Higgs. "Broken symmetries, massless particles and gauge fields". *Physics Letters* 12.2 (1964), pp. 132–133. ISSN: 0031-9163. DOI: https://doi.org/10.1016/0031-9163(64)91136-9. URL: http://www.sciencedirect.com/science/article/pii/0031916364911369.

[3] Peter W. Higgs. "Spontaneous Symmetry Breakdown without Massless Bosons". *Phys. Rev.* 145 (4 May 1966), pp. 1156–1163. DOI: 10.1103/PhysRev.145.1156. URL: https://link.aps.org/doi/10.1103/PhysRev.145.1156.

[4] Peter W. Higgs. "Broken Symmetries and the Masses of Gauge Bosons". *Phys. Rev. Lett.* 13 (16 Oct. 1964), pp. 508–509. DOI: 10.1103/PhysRevLett.13.508. URL: https://link.aps.org/doi/10.1103/PhysRevLett.13.508.

[5] Abdus Salam. "Weak and Electromagnetic Interactions". *Conf. Proc.* C680519 (1968), pp. 367–377. DOI: 10.1142/9789812795915_0034.

[6] Sheldon L. Glashow. "Partial-symmetries of weak interactions". *Nuclear Physics* 22.4 (1961), pp. 579–588. ISSN: 0029-5582. DOI: https://doi.org/10.1016/0029-5582(61)90469-2. URL: http://www.sciencedirect.com/science/article/pii/0029558261904692.

[7] Steven Weinberg. "A Model of Leptons". *Phys. Rev. Lett.* 19 (21 Nov. 1967), pp. 1264–1266. DOI: 10.1103/PhysRevLett.19.1264. URL: https://link.aps.org/doi/10.1103/PhysRevLett.19.1264.

[8] Serguei Chatrchyan et al. "Observation of a New Boson at a Mass of 125 GeV with the CMS Experiment at the LHC". *Phys. Lett.* B716 (2012), pp. 30–61. DOI: 10.1016/j.physletb.2012.08.021. arXiv: 1207.7235 [hep-ex].

[9] Georges Aad et al. "Observation of a new particle in the search for the Standard Model Higgs boson with the ATLAS detector at the LHC". *Phys. Lett.* B716 (2012), pp. 1–29. DOI: 10.1016/j.physletb.2012.08.020. arXiv: 1207.7214 [hep-ex].

[10] T. D. Lee and Chen-Ning Yang. "Question of Parity Conservation in Weak Interactions". *Phys. Rev.* 104 (1956), pp. 254–258. DOI: 10.1103/PhysRev.104.254.

[11] C. S. Wu et al. "Experimental Test of Parity Conservation in Beta Decay". *Phys. Rev.* 105 (4 Feb. 1957), pp. 1413–1415. DOI: 10.1103/PhysRev.105.1413. URL: https://link.aps.org/doi/10.1103/PhysRev.105.1413.

[12] R. P. Feynman and M. Gell-Mann. "Theory of the Fermi Interaction". *Phys. Rev.* 109 (1 Jan. 1958), pp. 193–198. DOI: 10.1103/PhysRev.109.193. URL: https://link.aps.org/doi/10.1103/PhysRev.109.193.

[13] F.J. Hasert et al. "Search for elastic muon-neutrino electron scattering". *Physics Letters B* 46.1 (1973), pp. 121–124. ISSN: 0370-2693. DOI: https://doi.org/10.1016/0370-2693(73)90494-2. URL: http://www.sciencedirect.com/science/article/pii/0370269373904942.

[14] F.J. Hasert et al. "Observation of neutrino-like interactions without muon or electron in the gargamelle neutrino experiment". *Physics Letters B* 46.1 (1973), pp. 138–140. ISSN: 0370-2693. DOI: https://doi.org/10.1016/0370-2693(73)90499-1. URL: http://www.sciencedirect.com/science/article/pii/0370269373904991.

[15] M. Tanabashi et al. "Review of Particle Physics". *Phys. Rev. D* 98 (3 Aug. 2018), p. 030001. DOI: 10.1103/PhysRevD.98.030001. URL: https://link.aps.org/doi/10.1103/PhysRevD.98.030001.

[16] Carlo Giunti and W. Kim Chung. *Fundamentals of Neutrino Physics and Astrophysics*. Oxford University Press, 2007.

[17] S. T. Petcov. "The Nature of Massive Neutrinos". *Adv. High Energy Phys.* 2013 (2013), p. 852987. DOI: 10.1155/2013/852987. arXiv: 1303.5819 [hep-ph].

[18] E. Aprile et al. "The XENON1T Dark Matter Experiment". *Eur. Phys. J.* C77.12 (2017), p. 881. DOI: 10.1140/epjc/s10052-017-5326-3. arXiv: 1708.07051 [astro-ph.IM].

[19] E. Aprile et al. "Design and performance of the XENON10 dark matter experiment". English (US). *Astroparticle Physics* 34.9 (Apr. 2011). ISSN: 0927-6505. DOI: 10.1016/j.astropartphys.2011.01.006.

[20] Xenon100 Collaboration et al. "The XENON100 dark matter experiment". *Astroparticle Physics* 35.9 (Apr. 2012), pp. 573–590. DOI: 10.1016/j.astropartphys.2012.01.003. arXiv: 1107.2155 [astro-ph.IM].

[21] D. S. Akerib et al. "The Large Underground Xenon (LUX) Experiment". *Nucl. Instrum. Meth.* A704 (2013), pp. 111–126. DOI: 10.1016/j.nima.2012.11.135. arXiv: 1211.3788 [physics.ins-det].

[22] XiGuang Cao et al. "PandaX: A Liquid Xenon Dark Matter Experiment at CJPL". *Sci. China Phys. Mech. Astron.* 57 (2014), pp. 1476–1494. DOI: 10.1007/s11433-014-5521-2. arXiv: 1405.2882 [physics.ins-det].

[23] E. Aprile et al. "Conceptual design and simulation of a water Cherenkov muon veto for the XENON1T experiment". *JINST* 9 (2014), P11006. DOI: 10.1088/1748-0221/9/11/P11006. arXiv: 1406.2374 [astro-ph.IM].

[24] J. Angle et al. "First Results from the XENON10 Dark Matter Experiment at the Gran Sasso National Laboratory". *Phys. Rev. Lett.* 100 (2008), p. 021303. DOI: 10.1103/PhysRevLett.100.021303. arXiv: 0706.0039 [astro-ph].

[25] E. Aprile et al. "Dark Matter Results from 225 Live Days of XENON100 Data". *Phys. Rev. Lett.* 109 (2012), p. 181301. DOI: 10.1103/PhysRevLett.109.181301. arXiv: 1207.5988 [astro-ph.CO].

[26] E. Aprile et al. "Limits on spin-dependent WIMP-nucleon cross sections from 225 live days of XENON100 data". *Phys. Rev. Lett.* 111.2 (2013), p. 021301. DOI: 10.1103/PhysRevLett.111.021301. arXiv: 1301.6620 [astro-ph.CO].

[27] E. Aprile et al. "Dark Matter Search Results from a One Ton-Year Exposure of XENON1T". *Phys. Rev. Lett.* 121.11 (2018), p. 111302. DOI: 10.1103/PhysRevLett.121.111302. arXiv: 1805.12562 [astro-ph.CO].

[28] E. Aprile et al. "Physics reach of the XENON1T dark matter experiment". *JCAP* 1604.04 (2016), p. 027. DOI: 10.1088/1475-7516/2016/04/027. arXiv: 1512.07501 [physics.ins-det].

[29] E. Aprile et al. "W value in liquid krypton". *Phys. Rev. A* 48 (2 Aug. 1993), pp. 1313–1318. DOI: 10.1103/PhysRevA.48.1313. URL: https://link.aps.org/doi/10.1103/PhysRevA.48.1313.

[30] E. Aprile and T. Doke. "Liquid Xenon Detectors for Particle Physics and Astrophysics". *Rev. Mod. Phys.* 82 (2010), pp. 2053–2097. DOI: 10.1103/RevModPhys.82.2053. arXiv: 0910.4956 [physics.ins-det].

[31] S Kubota, M Hishida, and J Raun. "Evidence for a triplet state of the self-trapped exciton states in liquid argon, krypton and xenon". *Journal of Physics C: Solid State Physics* 11.12 (June 1978), pp. 2645–2651. DOI: 10.1088/0022-3719/11/12/024. URL: https://doi.org/10.1088%2F0022-3719%2F11%2F12%2F024.

[32] Shinzou Kubota et al. "Dynamical behavior of free electrons in the recombination process in liquid argon, krypton, and xenon". *Phys. Rev. B* 20 (8 Oct. 1979), pp. 3486–3496. DOI: 10.1103/PhysRevB.20.3486. URL: https://link.aps.org/doi/10.1103/PhysRevB.20.3486.

[33] F. Glenn Knoll. *Radiation Detection and Measurement*. John Wiley and Sons, 2000.

[34] Alain Lansiart et al. *Development research on a highly luminous condensed xenon scintillator*. Elsevier, 1976.

[35] Elena Aprile et al. *Noble Gas Detectors*. John Wiley and Sons, 1969.

[36] E. Aprile et al. "Observation of Anti-correlation between Scintillation and Ionization for MeV Gamma-Rays in Liquid Xenon". *Phys. Rev.* B76 (2007), p. 014115. DOI: 10.1103/PhysRevB.76.014115. arXiv: 0704.1118 [astro-ph].

[37] E. Aprile et al. "Signal Yields of keV Electronic Recoils and Their Discrimination from Nuclear Recoils in Liquid Xenon". *Phys. Rev.* D97.9 (2018), p. 092007. DOI: 10.1103/PhysRevD.97.092007. arXiv: 1709.10149 [astro-ph.IM].

[38] E. Aprile et al. "First Dark Matter Search Results from the XENON1T Experiment". *Phys. Rev. Lett.* 119.18 (2017), p. 181301. DOI: 10.1103/PhysRevLett.119.181301. arXiv: 1705.06655 [astro-ph.CO].

[39] E. Aprile et al. "Design and performance of the XENON10 dark matter experiment". *Astroparticle Physics* 34.9 (2011), pp. 679–698. ISSN: 0927-6505. DOI: https://doi.org/10.1016/j.astropartphys.2011.01.006. URL: http://www.sciencedirect.com/science/article/pii/S0927650511000089.

[40] J. Angle et al. "Limits on spin-dependent WIMP-nucleon cross-sections from the XENON10 experiment". *Phys. Rev. Lett.* 101 (2008), p. 091301. DOI: 10.1103/PhysRevLett.101.091301. arXiv: 0805.2939 [astro-ph].

[41] E. Aprile et al. "XENON100 Dark Matter Results from a Combination of 477 Live Days". *Phys. Rev.* D94.12 (2016), p. 122001. DOI: 10.1103/PhysRevD.94.122001. arXiv: 1609.06154 [astro-ph.CO].

[42] P. Barrow et al. "Qualification Tests of the R11410-21 Photomultiplier Tubes for the XENON1T Detector". *JINST* 12.01 (2017), P01024. DOI: 10.1088/1748-0221/12/01/P01024. arXiv: 1609.01654 [astro-ph.IM].

[43] L. Baudis et al. "Performance of the Hamamatsu R11410 Photomultiplier Tube in cryogenic Xenon Environments". *JINST* 8 (2013), P04026. DOI: 10.1088/1748-0221/8/04/P04026. arXiv: 1303.0226 [astro-ph.IM].

[44] K. Lung et al. "Characterization of the Hamamatsu R11410-10 3-Inch Photomultiplier Tube for Liquid Xenon Dark Matter Direct Detection Experiments". *Nucl. Instrum. Meth.* A696 (2012), pp. 32–39. DOI: 10.1016/j.nima.2012.08.052. arXiv: 1202.2628 [physics.ins-det].

[45] M. Aglietta et al. "Muon "depth-intensity" relation measured by the LVD underground experiment and cosmic-ray muon spectrum at sea level". *Phys. Rev. D* 58 (9 Oct. 1998), p. 092005. DOI: 10.1103/PhysRevD.58.092005. URL: https://link.aps.org/doi/10.1103/PhysRevD.58.092005.

[46] E. Aprile et al. "Dark Matter Search Results from a One Ton-Year Exposure of XENON1T". *Phys. Rev. Lett.* 121 (11 Sept. 2018), p. 111302. DOI: 10.1103/PhysRevLett.121.111302. URL: https://link.aps.org/doi/10.1103/PhysRevLett.121.111302.

[47] E. Aprile et al. "Constraining the Spin-Dependent WIMP-Nucleon Cross Sections with XENON1T". *Phys. Rev. Lett.* 122 (14 Apr. 2019),

p. 141301. DOI: 10.1103/PhysRevLett.122.141301. URL: https://link.aps.org/doi/10.1103/PhysRevLett.122.141301.

[48] E. Aprile et al. "First Results on the Scalar WIMP-Pion Coupling, Using the XENON1T Experiment". *Phys. Rev. Lett.* 122 (7 Feb. 2019), p. 071301. DOI: 10.1103/PhysRevLett.122.071301. URL: https://link.aps.org/doi/10.1103/PhysRevLett.122.071301.

[49] J. Billard, L. Strigari, and E. Figueroa-Feliciano. "Implication of neutrino backgrounds on the reach of next generation dark matter direct detection experiments". *Phys. Rev.* D89.2 (2014), p. 023524. DOI: 10.1103/PhysRevD.89.023524. arXiv: 1307.5458 [hep-ph].

[50] E. Bagnaschi et al. "Likelihood Analysis of Supersymmetric SU(5) GUTs". *Eur. Phys. J.* C77.2 (2017), p. 104. DOI: 10.1140/epjc/s10052-017-4639-6. arXiv: 1610.10084 [hep-ph].

[51] E. Aprile et al. "Observation of two-neutrino double electron capture in 124Xe with XENON1T". *Nature* 568.7753 (2019), pp. 532–535. ISSN: 1476-4687. DOI: 10.1038/s41586-019-1124-4. URL: https://doi.org/10.1038/s41586-019-1124-4.

[52] Rafael F. Lang et al. "Supernova neutrino physics with xenon dark matter detectors: A timely perspective". *Phys. Rev.* D94.10 (2016), p. 103009. DOI: 10.1103/PhysRevD.94.103009. arXiv: 1606.09243 [astro-ph.HE].

[53] Alessandro Mirizzi et al. "Supernova Neutrinos: Production, Oscillations and Detection". *Riv. Nuovo Cim.* 39.1-2 (2016), pp. 1–112. DOI: 10.1393/ncr/i2016-10120-8. arXiv: 1508.00785 [astro-ph.HE].

[54] The SN neutrino data are available from https://wwwmpa.mpa-garching.mpg.de/ccsnarchive/index.html.

[55] H. -Th. Janka. "Neutrino Emission from Supernovae" (2017). DOI: 10.1007/978-3-319-21846-5_4. arXiv: 1702.08713 [astro-ph.HE].

[56] Francesco Capozzi et al. "Global constraints on absolute neutrino masses and their ordering". *Phys. Rev.* D95.9 (2017), p. 096014. DOI: 10.1103/PhysRevD.95.096014. arXiv: 1703.04471 [hep-ph].

[57] Smirnov, A. Yu. "The MSW effect and matter effects in neutrino oscillations". *Phys. Scripta* T121 (2005), pp. 57–64. DOI: 10.1088/0031-8949/2005/T121/008. arXiv: hep-ph/0412391 [hep-ph].

[58] Agafonova, N. Yu. and others. "Study of the effect of neutrino oscillations on the supernova neutrino signal in the LVD detector". *Astropart. Phys.* 27 (2007), pp. 254–270. DOI: 10.1016/j.astropartphys.2006.11.004. arXiv: hep-ph/0609305 [hep-ph].

[59] M. Goeppert-Mayer. "Double Beta-Disintegration". *Phys. Rev.* 48 (6 Sept. 1935), pp. 512–516. DOI: 10.1103/PhysRev.48.512. URL: https://link.aps.org/doi/10.1103/PhysRev.48.512.

[60] W. H. Furry. "On Transition Probabilities in Double Beta-Disintegration". *Phys. Rev.* 56 (12 Dec. 1939), pp. 1184–1193. DOI: 10.1103/PhysRev.56.1184. URL: https://link.aps.org/doi/10.1103/PhysRev.56.1184.

[61] L. Cardani. "Neutrinoless Double Beta Decay Overview". *SciPost Phys. Proc.* 1 (2019), p. 024. DOI: 10.21468/SciPostPhysProc.1.024. arXiv: 1810.12828 [nucl-ex].

[62] Francesco Vissani. "Signal of neutrinoless double beta decay, neutrino spectrum and oscillation scenarios". *JHEP* 06 (1999). [,700(1999)], p. 022. DOI: 10.1088/1126-6708/1999/06/022. arXiv: hep-ph/9906525 [hep-ph].

[63] P. A. R. Ade et al. "Planck 2013 results. XVI. Cosmological parameters". *Astron. Astrophys.* 571 (2014), A16. DOI: 10.1051/0004-6361/201321591. arXiv: 1303.5076 [astro-ph.CO].

[64] J. B. Albert et al. "Search for Majorana neutrinos with the first two years of EXO-200 data". *Nature* 510 (2014), pp. 229–234. DOI: 10.1038/nature13432. arXiv: 1402.6956 [nucl-ex].

[65] A. Gando et al. "Search for Majorana Neutrinos Near the Inverted Mass Hierarchy Region with KamLAND-Zen". *Phys. Rev. Lett.* 117 (8 Aug. 2016), p. 082503. DOI: 10.1103/PhysRevLett.117.082503. URL: https://link.aps.org/doi/10.1103/PhysRevLett.117.082503.

[66] Matthew Redshaw et al. "Mass and Double-Beta-Decay Q Value of ^{136}Xe". *Phys. Rev. Lett.* 98 (5 Feb. 2007), p. 053003. DOI: 10.1103/PhysRevLett.98.053003. URL: https://link.aps.org/doi/10.1103/PhysRevLett.98.053003.

[67] F. Alessandria et al. "Sensitivity of CUORE to Neutrinoless Double-Beta Decay" (2011). arXiv: 1109.0494 [nucl-ex].

[68] J. J. Gómez-Cadenas and Justo Martín-Albo. "Phenomenology of neutrinoless double beta decay". *PoS* GSSI14 (2015), p. 004. DOI: 10.22323/1.229.0004. arXiv: 1502.00581 [hep-ex].

[69] Evgeny Akhmedov. "Majorana neutrinos and other Majorana particles:Theory and experiment". In: 2014. arXiv: 1412.3320 [hep-ph].